ADVANCED FUNCTIONAL MATERIALS
www.afm-journal.de

In Situ Amorphization of Electrocatalysts

Huishan Meng, Zhijie Chen, Jinliang Zhu, Bo You, Tianyi Ma, Wei Wei, Sergio Vernuccio, Juan Xu,* and Bing-Jie Ni**

Electrocatalysis represents an efficient and eco-friendly approach to energy conversion, enabling the sustainable synthesis of valuable chemicals and fuels. The deliberate engineering of electrocatalysts is crucial to improving the efficacy and scalability of electrocatalysis. Notably, the occurrence of in situ amorphization within electrocatalysts has been observed during various electrochemical processes, influencing the energy conversion efficiency and catalytic mechanism understanding. Of note, the dynamic transformation of catalysts into amorphous structures is complex, often leading to various amorphous configurations. Therefore, revealing this amorphization process and understanding the function of amorphous species are pivotal for elucidating the structure-activity relationship of electrocatalysts, which will direct the creation of highly efficient catalysts. This review examines the mechanisms behind amorphous structure formation, summarizes characterization methods for detecting amorphous species, and discusses strategies for controlling (pre)catalyst properties and electrochemical conditions that influence amorphization. It also emphasizes the importance of spontaneously formed amorphous species in electrochemical oxidation and reduction reactions. Finally, it addresses challenges in the in situ amorphization of electrocatalysts. aiming to guide the synthesis of electrocatalysts for efficient, selective, and stable electrochemical reactions, and to inspire future advancements in the field.

1. Introduction

Electrocatalysis presents a compelling approach for producing clean energy carriers like hydrogen and high-value chemicals, all while minimizing environmental impact.[1] Electrocatalysts can lower the activation energy of reactions and improve the selective adsorption of intermediates during electrochemical activation.[2] This capacity promotes the electrochemical process for energy transition,[3] environmental protection,[4] and sustainable development.[5] Such examples include water splitting,[6] urea oxidation reaction (UOR),[7] biomass oxidation reaction (BOR),[8] carbon dioxide reduction reaction (CO_2RR),[9] etc. Significant efforts have been directed toward exploring highly efficient catalysts.[10] However, the inevitable reconstruction of electrocatalysts under electrochemical conditions can lead to changes in the catalyst's performance and shape the catalytic pathways.[11] Thus, it is essential to explore the in situ reconstruction process of electrocatalysts.

H. Meng, J. Xu
School of Ecological and Environmental Sciences
East China Normal University
Shanghai 200241, P. R. China
E-mail: jxu@des.ecnu.edu.cn

H. Meng, W. Wei
Centre for Technology in Water and Wastewater (CTWW)
School of Civil and Environmental Engineering
University of Technology Sydney
Sydney, NSW 2007, Australia

The ORCID identification number(s) for the author(s) of this article can be found under https://doi.org/10.1002/adfm.202405270

[Correction added on August 1, 2024, after first online publication: The author's name has been updated in this version.]

DOI: 10.1002/adfm.202405270

Z. Chen, B.-J. Ni
School of Civil and Environmental Engineering
The University of New South Wales
Sydney, NSW 2052, Australia
E-mail: zhijie.chen1@unsw.edu.au; bingjie.ni1@unsw.edu.au

J. Zhu
School of Resources
Environment and Materials
MOE Key Laboratory of New Processing Technology for Nonferrous Metals and Materials
Collaborative Innovation Center of Sustainable Energy Materials
Guangxi University
Nanning 530004, P. R. China

B. You
Key Laboratory of Material Chemistry for Energy Conversion and Storage (Ministry of Education)
Hubei Key Laboratory of Material Chemistry and Service Failure
School of Chemistry and Chemical Engineering
Huazhong University of Science and Technology
Wuhan 430074, P. R. China

With the characterization of post-catalysis electrocatalysts, the chemical properties, structural characteristics, porosity, and crystalline arrangement of electrocatalysts could undergo dynamic changes under the application of potentials and harsh electrochemical conditions.[12] In situ amorphization is one of the most frequently observed reconstruction phenomena.[13] Amorphous structures are characterized by a large electrochemical surface area, rich defect surface, and high structural flexibility.[14] Nevertheless, establishing the structure-activity relationship during electrocatalysis is challenging due to its complexity. The amorphous phase encompasses a wide range of catalyst compositions without being limited by valence, allowing for continuous adjustment of their electronic structure to optimize catalytic activity. Moreover, the amorphous structure not only influences the interaction with intermediates but also facilitates fast ion diffusion processes, significantly enhancing electrocatalytic performance.[15] Furthermore, the self-establishment of amorphous-crystalline heterostructures optimizes the transformation pathway of intermediates, contributing to a notable enhancement in catalytic reaction kinetics.[16]

Recently, many studies have employed an in situ electrochemical process to activate precatalysts.[17] During this process, the amorphization of electrocatalysts from surface to bulk exposes more active sites and promotes electrocatalytic performance.[18] Additionally, the in situ formation of amorphous species during electrochemical activation demonstrates a higher level of disorder than amorphous species grown thermally or electrochemically, thus efficient electrocatalysis.[19] Nevertheless, it is important to acknowledge that the occurrence of amorphous phases could also reduce electrochemical activity,[20] especially for single perovskite.[21] Moreover, moderate amorphization may benefit the oxygen evolution reaction (OER) activity and stability, while an excessively thin or thick amorphous layer is detrimental to catalytic reactions.[22] The excessive amount of amorphous species could decrease the selectivity of oxidation of 5-hydroxymethylfurfural (HMF).[23] The reconstruction process of electrocatalysts has been extensively reviewed,[24] especially for OER. However, in situ amorphization process of catalysts in different electrocatalytic reactions has not been comprehensively analyzed. Therefore, it is crucial to summarize emerging advancements in the in situ amorphization of electrocatalysts to provide insights into the rational design of high-performance catalysts and the underlying mechanism of catalytic reactions.

Herein, we outline the in situ amorphization process of electrocatalysts during electrochemical processes, as well as the role of self-evolved amorphous species in electrocatalysis. The in situ amorphization process is primarily associated with the redox reactions of electrocatalysts during electrochemical activation. It primarily involves "dissolution-precipitation", direct redox transformation, or atomic rearrangement of catalysts, leading to the formation of amorphous species. Ex situ and in situ characterization technologies are utilized to discern the generation of amorphous species and their dynamic evolution process. The degree of amorphization, the composition of amorphous species, and the activity of these species could be controlled through the modulation of catalyst properties, including their composition, structure, and morphology. Additionally, adjustments to electrochemical operational parameters and electrolyte conditions could regulate the amorphization process. The role of the in situ formed amorphous species in regulating electrochemical processes is also discussed, which is followed by the perspectives in this field. **Figure 1** mainly summarizes the methods for regulating catalysts' in situ amorphization and the function of amorphous species in electrocatalytic reactions.

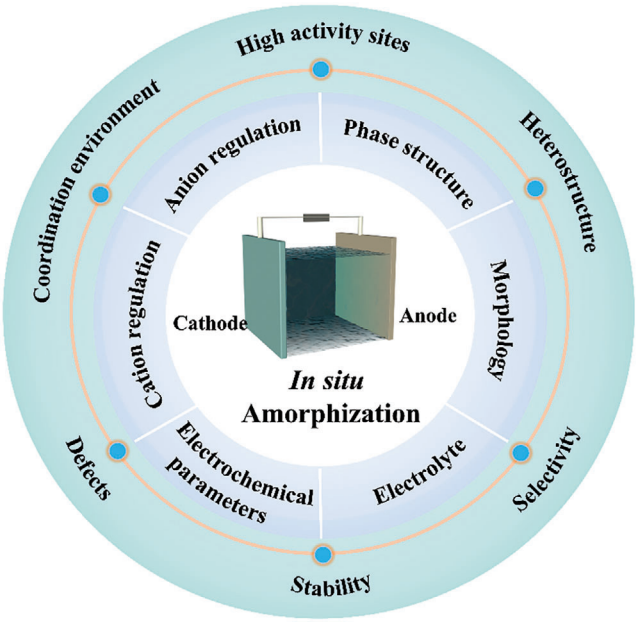

Figure 1. Schematic of the in situ amorphization of electrocatalysts.

2. Mechanisms of In Situ Amorphization of Electrocatalysts

The correlation between the catalytic performance of materials and their structures is crucial for optimizing catalyst functionality in electrocatalysis.[25] However, the occurrence of in situ amorphization of catalysts under applied potential and harsh electrolyte conditions significantly impacts their electrochemical performance, posing a substantial challenge in building the structure-activity relationship.[11a] The amorphous structure offers several advantages during electrocatalysis,[26] thus comprehending the underlying mechanisms of amorphization in the electrolysis process is essential for designing efficient electrocatalysts.

2.1. Dissolution-Precipitation Process

Under potential stimulation, certain electrocatalyst components would leach out and subsequently react with the electrolyte,

T. Ma
School of Science
Royal Melbourne Institute of Technology
Melbourne, VIC 3000, Australia
S. Vernuccio
Department of Chemical & Biological Engineering
The University of Sheffield
Sheffield S1 3JD, UK

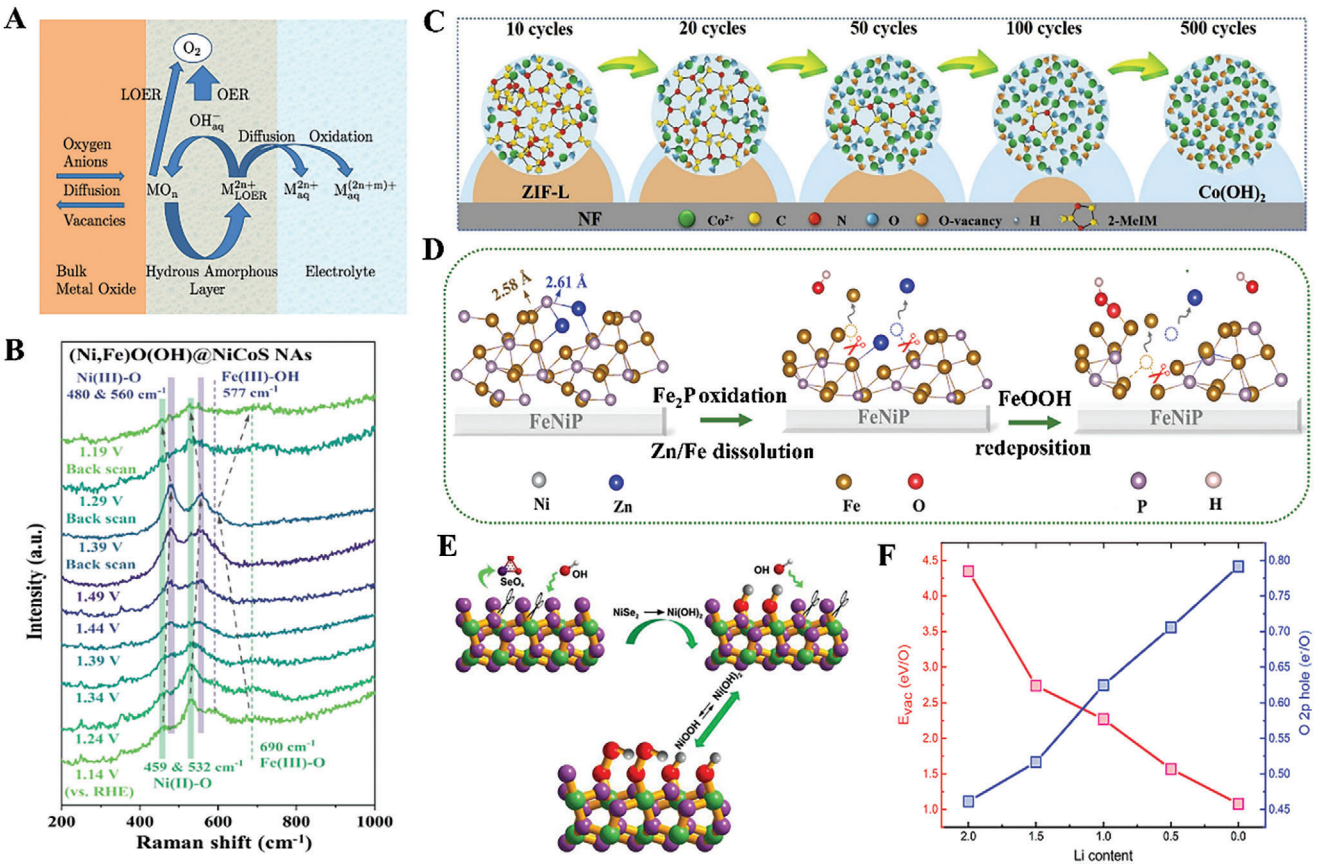

Figure 2. A) Schematic illustration of the dissolution-precipitation mechanism induced by LOER during the OER in an alkaline medium.[29] Copyright 2015, Springer Nature. B) *Operando* electrochemistry-Raman spectra of (Ni,Fe)O(OH)@NiCoS in alkaline electrolyte.[34] Copyright 2021, Elsevier. C) Schematic representation of the amorphous $Co(OH)_2$ evolution with the organic frame oxidation from CoM-ZIF-L during CV activation.[36] Copyright 2021, Elsevier. D) Reconstruction diagram of Zn-doped FeNiP@Fe_2P during electrochemical activation based on theoretical calculations.[46] Copyright 2024, Wiley. E) In situ reconstruction schematic diagram of $NiSe_2$ during electrocatalysis in an alkaline solution. Ni, Se, O, and H are depicted as green, purple, red, and gray balls, respectively.[48] Copyright 2019, Elsevier. F) Correlation between lithium content and formation energy of oxygen vacancies and unoccupied oxygen 2p states in $Li_xCo_2O_4$.[51] Copyright 2019, American Chemical Society.

leading to the precipitation of an amorphous phase on the catalyst surface during the electrocatalytic process. Yang et al. investigated the in situ formation amorphous phase on $LiCoPO_4$ with phosphorus leaching after potential cycling at neutral pH, which bears compositional resemblance to those acquired through the electrodeposition of cobalt oxide materials in electrolyte solutions buffered with phosphate (Co-P_i).[27] The presence of Co^{2+} ions with high spin and substitutionally labile properties in $LiCoPO_4$ suggests that they may dissociate into the solution at equilibrium. The authors speculated that the dissolved Co^{2+} ions could readily re-deposit on the surface during potential cycling in electrolytes containing leached phosphorus. Hence, $LiCoPO_4$ possessing an amorphous structure exhibits electrochemical properties comparable to those of Co-P. Similarly, Xu et al. found that the amorphous phase generated after the potential cycling of $SrCo_{0.8}Fe_{0.2}O_{3-\delta}$ (SCF02) in KOH solution is similar to that formed during the cycling of $SrCoO_{3-\delta}$ (SC) in the electrolyte containing Fe^{3+}.[28] It can be speculated that the perovskite oxide undergoes a dissolution/precipitation cycle to form an amorphous phase, which allows for the participation of Fe from the electrolyte.

During the in situ amorphization process of SC and SCF02, the content of Sr and lattice oxygen was dramatically reduced. The ""dissolution-precipitation"" process is well documented during the typical lattice oxygen evolution reaction (LOER). Schmidt et al. found that metal oxides would be unstable at potentials exceeding the oxygen evolution equilibrium potential and could leach into the electrolyte as a result of the oxidation of lattice oxygen anions.[29] Subsequently, metal cations with unchanged valency can be re-deposited onto the catalyst surface in the alkaline electrolyte when an appropriate potential is applied. This reconstruction process forms a layer with reduced structural order, termed the hydrous amorphous layer (**Figure 2A**). The thickness of the hydrous amorphous layer extends into the bulk catalyst due to the extraction of oxygen anions from the lattice within the bulk catalyst, facilitated by the leaching of positively charged metal cations. Most metal oxides, such as perovskite oxides,[30] $La_2Li_{0.5}Ni_{0.5}O_4$,[31] and $CoCr_2O_4$,[32] undergo a process of amorphization through an initial leaching of unstable elements, followed by a dissolution-precipitation process involving transition metals that leads to the formation of amorphous species.

2.2. Redox Reactions

2.2.1. Direct Redox Processes of Precatalysts

Unlike the development of the amorphous structure through the dissolution-precipitation of transition metal species during in situ electrochemical activation, catalysts undergo an electrochemical redox reaction to promote amorphization.[33] Under the potential-dependent electrochemical reconstruction processes, the direct redox process of electrocatalysts induces the structure transformation into an amorphous structure. Shao et al. proposed that the Ni-Fe hydroxide/oxide ((Ni,Fe)O(OH)) structure could be converted into amorphous γ-NiFeOOH with high electrochemical activity.[34] According to *operando* electrochemistry-Raman techniques, the peak corresponding to Ni(III) in amorphous γ-NiOOH was observed and became stronger with the increase in potential from 1.14 to 1.49 V versus reversible hydrogen electrode (RHE) (Figure 2B). The γ-NiOOH with an interlayer space and high-valence Ni sites is prone to exhibit amorphous characteristics because of randomly oriented bonds and an unsaturated coordination environment.

Metal-organic frameworks (MOFs) utilized as electrocatalysts can experience amorphization due to the redox activity of ligands during the electrochemical activation process.[35] A highly active amorphous metal hydroxide was synthesized on CoM-zeolitic imidazolate framework-large (CoM-ZIF-L), wherein OH^- ions present in the electrolyte replaced ligands in CoM-ZIF-L.[36] During the electrochemical activation process of cyclic voltammetry (CV), CoM-ZIF-L experienced a reversible redox reaction involving the Co site transitioning between Co(II)/Co(III) and Co(III)/Co(IV), leading to the presence of amorphous $Co(OH)_2$. In contrast, the CoM-ZIF-L was transformed into highly crystalline fragments of $Co(OH)_2$ during the chemical etching process in the KOH solution. The reversible redox reaction of the cobalt site disrupts the coordination between cobalt ions and 2-methylimidazole, facilitating the introduction of OH^- to replace 2-methylimidazole and form the amorphous phase, as depicted in Figure 2C. During the HER process in neutral conditions, the application of MOF-derived catalysts also resulted in the generation of amorphous CoS_x due to the disruption of the organic coordination environment.[37] By analyzing the evolution of the 2-methylimidazole-based nitrogen coordination environment, it was observed that the organic ligand thiourea degrades into S^{2-} ions induced by the production of OH^- during HER. Therefore, the S^{2-} replaces the organic ligand to react with Co^{2+} ions, causing the development of amorphous CoS_x. The in situ formed amorphous structure in MOF-based catalysts appears to be associated with substituting the organic ligand, which is deeply dependent on both the catalyst's structure and the electrochemical conditions.

In addition to metal oxides, metal carbides,[38] nitrides,[39] and sulfides,[40] also experience redox reactions to form amorphous oxides during both OER and hydrogen evolution reaction (HER) in alkaline electrolytes. Non-oxide metal catalysts display lower thermodynamic stability compared to metal oxides, making them prone to oxidation during the electrochemical process.[41] Ren et al. investigated the reconstruction of the NiMoN@NiFeN catalyst in the OER process.[42] The amorphous NiFe oxides and NiFe oxy(hydroxides) were generated with the oxidation of Ni^{2+} and Fe^{2+} to Ni^{3+} and Fe^{3+} respectively. Yang et al. reported that the $(Co_xFe_{1-x})_3Mo_3C$ component in the CoFe/$(Co_xFe_{1-x})_3Mo_3C$ catalyst could experience oxidation to form active amorphous Co(Fe) oxyhydroxides.[43] Meanwhile, the valence of Fe and Co was shifted to a higher value. In situ formation of amorphous oxide/ oxy(hydroxides) species can also be observed for the bimetallic carbide Mo_6Ni_6C[44] and Ni/W_5N_4,[45] corresponding to the metal redox in the pre-catalysts. The amorphization of non-oxide may also be correlated with both the shift in metal valence and the dissolution-precipitation mechanism. Huang et al. reported that the dissolution-redeposition reconstruction of the Zn-doped FeNiP@Fe_2P nanoarray catalyst involved the continuous dissolution of Zn and Fe_2P, accompanied by oxidation of Fe^{2+} to Fe^{3+} (Figure 2D).[46] Ultimately, amorphous FeOOH formed as iron ions combined with OH^- in the electrolyte. Furthermore, the formation of amorphous Ru oxide in the bimetallic Ir-Ru catalyst was associated with the dissolution and redeposition of Ru during the in situ reconstruction process.[47]

According to some viewpoints, electrocatalysts may undergo reconstruction into a crystalline layer due to the leaching of unstable elements, potentially resulting in subsequent amorphization with further redox conditions. Lau et al. demonstrated the generation of an amorphous/crystalline heterojunction ($Ni(OH)_2$/NiOOH) from the $NiSe_2$ precatalyst in an alkaline solution during both HER and OER.[48] The $NiSe_2$ phase completely disappeared after electrochemical activation. The features of $Ni(OH)_2$ were detected using the selected area electron diffraction pattern, and X-ray photoelectron spectroscopy analysis results indicated a reversible transition between crystalline $Ni(OH)_2$ and amorphous NiOOH. They proposed that pyrite-type $NiSe_2$ transformed into lamellar-type $Ni(OH)_2$ after Se_2^{2-} leaching as SeO_x initially, and then $Ni(OH)_2$ evolved into amorphous NiOOH with lattice expansion during polarization (Figure 2E). The leaching of other unstable compositions also induces the metastable hydroxide form, which is subsequently oxidized to yield an amorphous oxyhydroxide phase, such as V-NiS[49] and $Co_3(PO_4)_2{\cdot}8H_2O$.[50]

2.2.2. Oxygen Vacancies Contribute to Amorphization

The redox process of electrocatalysts can promote the generation of vacancies, thereby facilitating the in situ amorphization process. Zhu et al. investigated a reversible surface amorphization on Mn_2O_3 during OER.[52] They employed in situ transmission electron microscope imaging to track the dynamic development of the surface layer. The evolution of an amorphous structure was accompanied by the observation of redox Mn valence changes and oxygen defects. They suggested that the formation of the reversible surface layer might be related to the dynamic process involving the creation and filling of oxygen deficiencies on the surface of Mn_2O_3. Leaching of unstable electrocatalysts and the oxidation of lattice oxygen could induce the generation of vacancies, initiating interactions of electrocatalysts with ions in the electrolyte to induce amorphization. Zhang and coworkers illustrated that oxygen vacancies resulting from lithium leaching and the oxidation of tetravalent cobalt were subsequently filled by hydroxyl ions, leading to the amorphization of $Li_2Co_2O_4$.[51] A correlation between delithiation and the generation of the amorphous

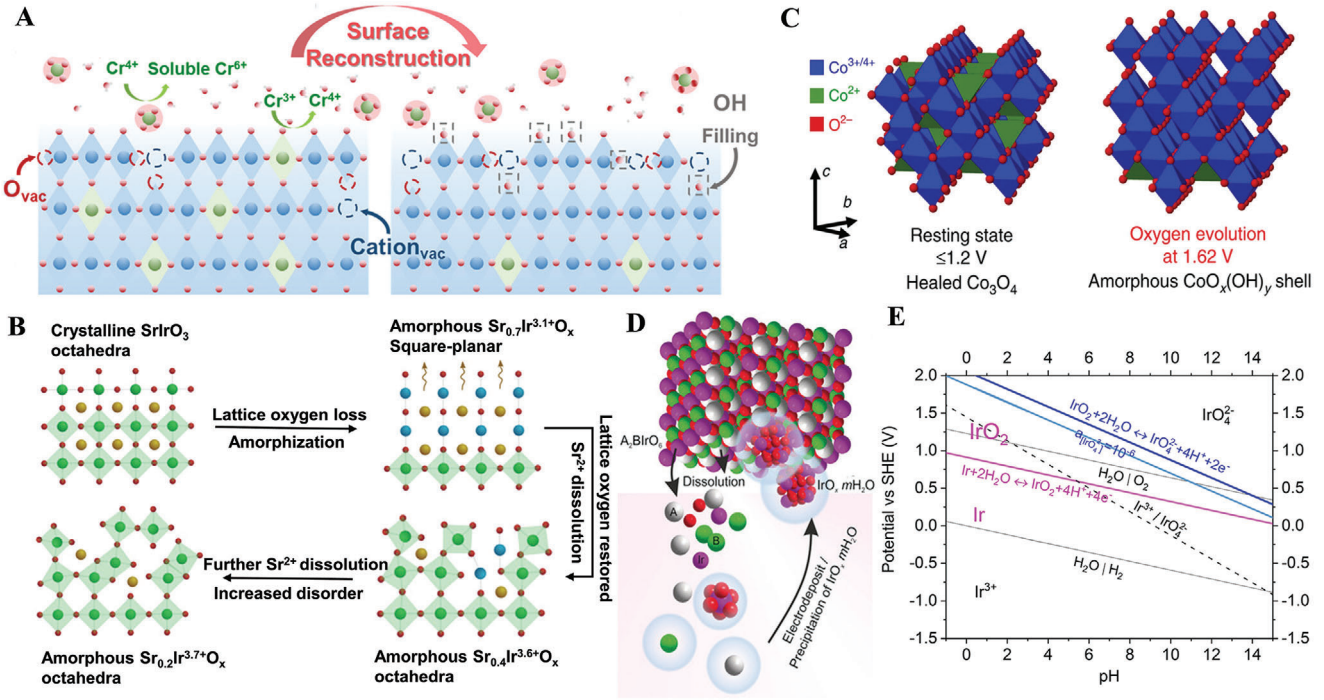

Figure 3. A) Schematic diagram of the formation of vacancies and subsequent reconstruction processes on NiCrO.[53] Copyright 2024, American Chemical Society. B) The structural evolution of $SrIrO_3$ along the proposed reconstruction pathway from crystalline to amorphous phase.[19] Copyright 2021, American Association for the Advancement of Science. C) The alteration in the near-surface structure of crystalline Co_3O_4 before and after amorphization.[57] Copyright 2021, Springer Nature. D) The dissolution-electrodeposition of iridium species during the electrocatalysis process.[58] Copyright 2019, Wiley. E) The Pourbaix diagram of iridium depicts its dependency on both pH and potential at room temperature (25 °C).[59] Copyright 2022, American Chemical Society.

active layer was established. Delithiation significantly reduces the energy required for the formation of oxygen vacancies (Figure 2F) and promotes the emergence of Co^{4+} species. Co^{4+} ions also can activate oxidized oxygen, facilitating the electro-driven occupation of these vacancies by OH^-, ultimately resulting in the formation of an amorphous (oxy)hydroxide surface layer.

The defects arising directly from the leaching of unstable elements may also induce the generation of amorphous species. Cr leaching from NiCrO during electrocatalysis resulted in the creation of numerous vacancies, which promote the formation of amorphous NiOOH through OH filling (**Figure 3A**).[53] Furthermore, the leaching of lattice elements from Ir-based electrocatalysts under acidic electrochemical conditions prompts defect formation, which may initiate the process of amorphization. Shao et al. reported that monoclinic $SrIrO_3$ experienced amorphization compared with IrO_2, primarily triggered by the leaching of almost all lattice Sr^{2+} ions during the HER process in an acidic medium.[54] Progressive surface amorphization might primarily be attributed to defects resulting from the leaching of alkaline-earth elements, rather than the leaching of Ir. Xu et al. also proposed the collapse of the initial pseudo-cubic structure and the emergence of the amorphous IrO_xH_y phase occurred when Sr and Co were rapidly leached out from $SrCo_{0.9}Ir_{0.1}O_{3-\delta}$ during electrochemical activation.[55]

The presence of oxygen vacancies on the catalyst surface could amplify the dissolution of alkaline-earth elements during the electrocatalytic process, significantly increasing the degree of in situ amorphization in the active layer. Suntivich et al. investigated the amorphization of $SrIrO_3$ when lattice oxygen redox was activated during the OER process.[19] They proposed that the accumulation of oxygen vacancies, activated by lattice oxygen, could induce structural instability in $SrIrO_3$, resulting in the formation of amorphous $Sr_{0.7}Ir^{3.1+}O_x$ with a square-planar structure (Figure 3B). Furthermore, more leaching of Sr occurred after the initial phase of reconstruction, leading to the development of a highly disordered structure. The coupled formation of oxygen vacancies and Sr leaching facilitated the generation of an active amorphous layer in $SrIrO_3$.

2.3. Migration of Atoms

During the electrocatalysis process, the dynamic migration of atoms in catalysts initiates the amorphization. Ersen et al. observed the amorphization of Co_3O_4 during OER in alkaline and neutral electrolytes.[56] In a neutral medium, the absence of detectable phosphorus suggests that the amorphous cobalt (oxy-hydr)oxide phase was not formed via electrodeposition. In an alkaline environment, more pronounced amorphization occurred alongside enhanced OER performance, presumably correlated with the extent of charge transfer. Strasser et al. discovered that the crystalline Co_3O_4 underwent oxidation to form $CoO_x(OH)_y$ without changing phase at the onset of electrocatalytic oxygen evolution. As the electrode potential and oxygen evolution rate

increase, the Co oxidation state gets higher, and the Co coordination undergoes a partial change from tetrahedral to octahedral. The random site occupancy of $Co^{3+/4+}$ ions within a marginally rearranged O^{2-} lattice results in an amorphization process of the near-surface $CoO_x(OH)_y$ layer (Figure 3C).[57]

Based on the discussions above, electrochemical conditions, including pH and applied potential, govern the reconstruction of electrocatalysts as depicted by the Pourbaix diagram. Grimaud et al. suggested a widespread dissolution-electrodeposition/precipitation mechanism for the formation of the $IrO_x{\cdot}mH_2O$ in Ir^{v}-based perovskite materials (Figure 3D).[58] Formation of the $IrO_x{\cdot}mH_2O$ phase was influenced by the pH value and applied potential, exhibiting limited correlation with the pre-catalyst. Iridium from Ir-based catalysts can dissolve in acidic electrolytes and then precipitates in its oxidized form at the OER potential, as shown in the Pourbaix diagram for iridium (Figure 3E).[59] Nevertheless, the underlying mechanisms driving amorphization processes remain elusive. It is worth mentioning that electrocatalysts may experience in situ reconstruction, leading to the production of both crystalline and low-crystalline phases.[60] An in-depth investigation into the origins of amorphization demands further endeavors through the application of advanced in situ techniques and analytical methods.

Under applied potentials, electrocatalysts will undergo self-reconstruction and lead to phase evolution. The formation of amorphous species during different electrochemical processes is a complex phenomenon that involves intricate structural transformations within the catalyst, influenced by factors such as the specific electrochemical environment, the nature of the redox reactions taking place, and the interactions between the catalyst and the electrolyte. In this context, it is essential to individually analyze the in situ amorphization process of various catalysts on a case-by-case basis. In addition, the physicochemical properties of catalysts and electrochemical operations are interdependent and mutually influence each other in the amorphous process. Therefore, the chemical properties of precatalysts and electrochemical conditions can be applied to regulate the amorphization process, which will be discussed later.

3. Characterization of Self-Evolved Amorphous Species

Identifying the properties of the self-evolved amorphous species, including the structure feature and chemical compositions, is crucial for understanding the electrochemical active sites and establishing structure-activity relationships. To gain a full understanding of the active species during electrocatalysis, several characterization techniques were employed to identify the structure information, such as X-ray diffraction (XRD), transmission electron microscopy (TEM), Raman spectroscopy and X-ray absorption spectroscopy (XAS).[61] Hence, in this section, we summarize both ex situ and in situ characterization techniques aimed at gaining insights into the amorphous species and the dynamic reconstruction process.

3.1. X-Ray Diffraction

In situ amorphization typically involves the phase transformation of precatalysts from crystalline to amorphous phases, which can be detected using XRD. Crystalline materials show distinct diffraction peaks in XRD due to their ordered structure, while amorphous materials show broad, featureless scattering due to their disordered structure. For example, Mullins et al. discovered that NiS transformed into amorphous nickel oxide during electrochemical activation.[62] This conversion was characterized by the loss of crystalline peaks in the XRD patterns and the absence of new diffraction peaks. Comparable observations can be made in the complete amorphization of other precatalysts, such as Co_3C,[38] erythrite,[63] and CoP.[64] Following partial amorphization of the precursor catalysts, the alterations in XRD patterns are generally minor. NiFe-OH-F suffered partial amorphization to form an amorphous layer after electrochemical activation,[65] whereas the diffraction peaks of the precatalyst were still observable in the XRD pattern. The same phenomenon has been observed in Ni and Ni_3N nanoparticles.[66] Grazing-incident X-ray diffraction (GIXRD) enables detailed characterization of surface and interface properties. Scott et al. employed GIXRD to uncover the alterations in crystallinity on the surface of polycrystalline Cu electrodes after undergoing electrochemical reduction.[67]

In situ XRD provides real-time insights into the structural transformations occurring during electrochemical amorphization. Zhang and his co-authors investigated the structural evolution of an in situ electrochemical amorphization electrode using the in situ XRD technique.[68] They observed that the peaks of the pristine ZnV_2O_4 phase were significantly weakened with the emergence of the amorphous structure. Strasser et al. elucidate the characterization of Co_3O_4 films under various electrochemical potentials using in situ GIXRD experiments.[57] Although the Co_3O_4 structure remained unchanged under applied electrochemical potential (**Figure 4A**), analysis of the broadening of selected Co_3O_4 reflections revealed alterations in the mean structural coherence length of crystalline domains. Notably, the Co_3O_4 demonstrated its maximum structural coherence length at the onset potential of OER, followed by structural transformations leading to decreased structural coherence length as electrode potential increased (Figure 4B). This transformation was attributed to the appearance of an amorphous CoO_x shell on crystalline Co_3O_4. Notably, the amorphous species can revert to crystalline Co_3O_4 once the applied potential is outside the oxygen evolution range, demonstrating a reversible transformation. This study utilizes GIXRD to reveal the reversible surface phase transformations during the in situ amorphization process. Ex/in situ XRD technology is useful for investigating amorphization with noticeable phase changes. However, XRD is inadequate for analyzing reconstructed electrocatalysts with the presence of a thin amorphous phase. The formation of an amorphous shell on LiCoBPO did not alter the GIXRD patterns after OER.[69] Direct evidence should be used to further characterize the formation of the amorphous structure during electrochemical reconstruction.

3.2. Transmission Electron Microscopy

Microscopic analysis techniques provide direct insights into the formation of amorphous structures. The structure evolution from surface to bulk could be detected by TEM. Selected area electron diffraction (SAED) pattern from the corresponding TEM elucidates the phase transformation of the catalyst. The occurrence

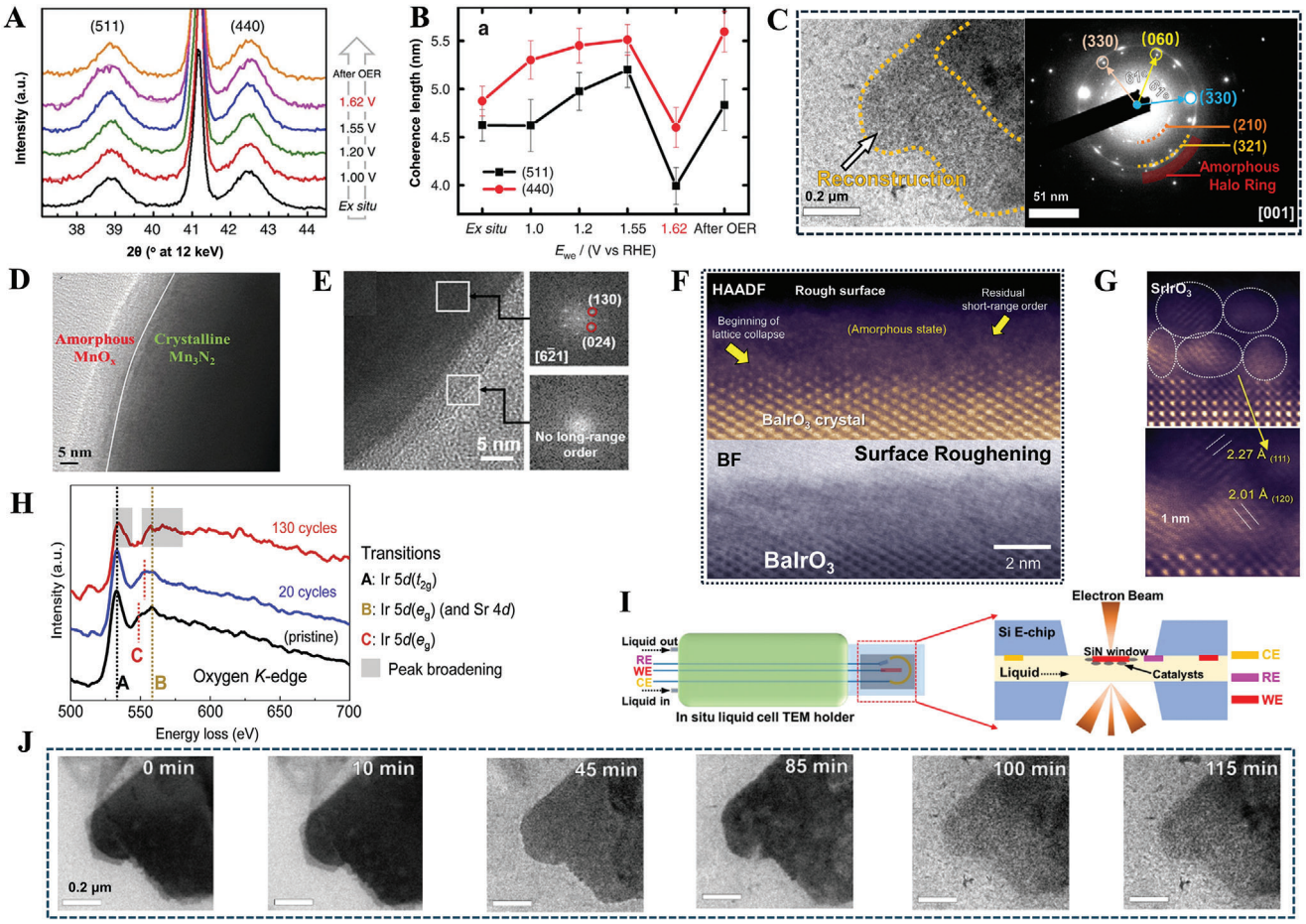

Figure 4. A) In situ GIXRD patterns, B) along with their corresponding structural coherence length of Co_3O_4.[57] Copyright 2015, Nature Portfolio. C) TEM images of the in situ reconstructed Ru-$NiPS_3$ (left) and related SAED patterns (right).[70] Copyright 2023, Nature Portfolio. D) HR-TEM image of Mn_3N_2 catalyst after in situ amorphization.[39] Copyright 2018, Wiley. E) HR-TEM image of reconstructed $SrIrO_3$, along with its corresponding FFT patterns.[54] Copyright 2020, American Chemical Society. F) The surface structure and atomic-level distribution of $BaIrO_3$ detected by HAADF and BF-STEM. G) HAADF images of the in situ reconstructed $SrIrO_3$. H) EELS analysis of O K-edges on the amorphous surface region.[73] Copyright 2019, Cell Press. I) Schematic representation of in situ electrochemical liquid cell TEM holder and its accompanying apparatus. J) In situ TEM imagines of Ru-$NiPS_3$ over time.[70] Copyright 2023, Nature Portfolio.

of the amorphous halos ring in the SAED pattern served as an indication of the amorphization occurring on the surface of the catalyst (Figure 4C).[70] High-resolution TEM (HR-TEM) provides direct evidence of the amorphization by detecting atomic arrangement. Driess et al. utilized TEM and HR-TEM to get insights into the near-surface structure of Mn_3N_2.[39] TEM images only showed the structural changes of the crystalline particles after the electrochemical process. In HR-TEM images, a distinct disordered shell of MnO_x was prominently observed on the surface of crystalline Mn_3N_2 (Figure 4D), evidencing that the Mn_3N_2 surface undergoes amorphization after strong alkaline electrochemical oxidation. The integration of HR-TEM with fast Fourier transform (FFT) analysis serves as a valuable method to understand the transformation from crystalline to amorphous states in the catalyst. In comparison with the crystalline $SrIrO_3$, FFT images of the amorphous surface revealed the absence of long-range ordering (Figure 4E).[54] TEM with energy-dispersive spectroscopy (EDS) is a commonly employed method for identifying the composition of in situ formed amorphous phases, thereby assisting in the speculation of the reconstruction process and compound composition.[71] According to HR-TEM-EDS analysis, the emergence of an amorphous layer on $Sr_xCa_{1-x}FeO_{3-\delta}$ is associated with the significant leaching of A-site ions on the surface.[72]

Employing scanning transmission electron microscopy (STEM) in both high-angle annular dark-field (HAADF) and bright-field (BF) modes allows for an in-depth examination of amorphous structure, revealing atomic-level details and local atomic arrangements. Chung et al. conducted HAADF-STEM and BF-STEM to directly observe the atomic-column resolution of $SrIrO_3$ and $BaIrO_3$ during the OER under an acidic electrolyte.[73] HAADF and BF-STEM images in Figure 4F revealed the lattice collapse of $BaIrO_3$, resulting in a rough and amorphous surface. Conversely, $SrIrO_3$ after 60 cycles showed an amorphous surface layer with the presence of nanometer-scale polycrystals (Figure 4G). Along with STEM, electron energy-loss spectroscopy (EELS) indicated the near-amorphous nature of the $SrIrO_3$ following 130 anodic cycles. The significant broadening observed in peaks A and B in the oxygen K-edge spectrum after

130-cycle samples implied the development of an amorphous structure (Figure 4H). This phenomenon is attributed to the disruption of oxygen octahedral symmetry within the [IrO_6] units and variations in Ir-O bond length in the amorphous state. STEM-EELS measurements also can verify the elemental composition and chemical valence of amorphous species. Zhu et al. utilized STEM-EELS spectra to illustrate the amorphous surface material on Mn_2O_3 nanocatalyst.[52] Spatially resolved EELS fine structures of Mn_2O_3 after OER revealed a red shift in Mn-$L_{2,3}$ edges and an increase in the L_2/L_3 intensity ratio on the surface, indicating a reduced Mn valence. Coupled with the analysis of O-K edge fine structures, the amorphous surface resembled the Mn_3O_4 phase, containing mixed Mn^{2+} and Mn^{3+} ions.

In situ technology has been utilized to monitor the structural evolution of catalysts during electrochemical activation. Zhao's group conducted an in situ electrochemical TEM technique to investigate the reconstruction of Ru-$NiPS_3$ during the alkaline HER process.[70] The design of the in situ electrochemical liquid cell TEM holder and the liquid cell structure is depicted in Figure 4I. The in situ electrochemical TEM captured the stepwise evolution of a reconstructed surface at the Ru-$NiPS_3$ (Figure 4J), with the corresponding SAED patterns gradually exhibiting an amorphous halo ring. In situ electrochemical TEM sequential images, together with corresponding in situ sequential SAED patterns, reveal the amorphization process during electrocatalysis. In situ TEM is capable of revealing the dynamic changes in structure and composition.[56,74] Xi and co-researchers similarly applied in situ electron microscopy to uncover the structural and compositional transformation of $(NiCo)S_{1.33}$.[75] An amorphous shell developed on the catalyst surface following the application of 0.9 V for 21 s, and its thickness grew from 27.75 to 57.00 nm as time progressed. Moreover, in situ atomic HAADF was utilized to investigate the surface amorphization at different applied potentials. Amorphous regions were notably extended at elevated applied potentials ranging from 0.9 to 1.3 V. The corresponding in situ elemental mapping of S and O, along with in situ EELS of the O K-edge, expounded the evolution of composition and chemical states during amorphization.

3.3. Raman Spectroscopy and Fourier-Transform Infrared Spectroscopy (FT-IR)

Raman spectroscopy is a valuable tool for analyzing chemical compounds based on their molecular vibrations, offering detailed information about the molecular structure of materials. Recently, Raman spectroscopy has been widely used to identify the in situ-formed amorphous species during electrocatalysis.

Analyzing the positions and intensities of peaks in Raman scattering spectra allows for the identification of amorphous chemical properties. Liu et al. employed Raman spectroscopy to define the species present on the amorphous surface of FeS_2 microspheres.[76] As shown in **Figure** 5A, the peaks observed at 337 and 370 cm^{-1} were assigned to the characteristic signatures of pyrite FeS_2. Following OER, the reduced intensity of these peaks suggested the self-transformation of FeS_2, while the appearance of characteristic peaks corresponding to FeOOH indicated the formation of new species. Similarly, two peaks ≈478 and 556 cm^{-1} were observed in the Raman spectra of reconstructed Co, Cl-NiS, associated with the chemical bonding of Ni-O in the NiOOH phase.[77] The formed NiOOH on the amorphous structure contributed to the ethylene glycol electrooxidation reaction. Moreover, the additional broad peak at ≈1050 cm^{-1} on the reconstructed B,Co-NiS indicated the presence of $NiOO^-$, further confirming the formation of NiOOH.[78]

In situ Raman measurements were performed to illustrate the real-time evolution of amorphous species during the electrochemical process, assisting in uncovering the active sites in electrocatalysis. Xiong et al. utilized in situ Raman spectroscopy to investigate the generation of amorphous species on the NiNPS.[79] As displayed in Figure 5B, the peaks related to Ni-OH and Ni-O were detected at the applied potential of 0.2 V. The detection of NiOOH peaks at potentials between 0.3 and 0.5 V implied an additional phase transformation as the applied potential increases. Significant Raman shifts of NiOOH were maintained during the OER process. Upon reducing the potential, NiOOH underwent a reversible transformation into Ni hydroxide and NiO. The amorphous layer contained both Ni hydroxide and NiO in the post NiNPS. Therefore, in situ Raman reveals that the NiOOH serves as the active species during oxygen evolution. In situ Raman spectra can also be employed to explore the dynamic evolution of reconstructed species over time. Stable Raman shifts of NiOOH were detected on the surface of Au@NiS_x after 30 minutes of reconstruction (Figure 5C).[80] In situ Raman spectroscopy is a frequent method to investigate the mechanisms underlying in situ amorphization. Zheng et al. reported that in situ Raman spectra taken during the OER and 5-hydroxymethylfurfural oxidation (HMFOR) showed characteristic peaks of amorphous NiOOH in both reactions.[81] During OER, these peaks were detected starting at 1.1 V versus RHE, whereas in the HMFOR process, NiOOH peaks only appeared at higher potentials (>1.45 V). Therefore, the author speculated that active NiOOH oxidizes HMF reactants at lower potentials compared with OER, followed by its reduction back to Ni^{2+}, confirming the evolution of NiOOH as active sites in HMFOR. In situ Raman spectroscopy measurements could be performed to elucidate the amorphization behavior of various electrocatalysts.[82] Compared to $Ni_2P_4O_{12}$, amorphous species in Ir/$Ni_2P_4O_{12}$ appeared after fewer activation cycles, and the peaks of amorphous NiOOH were stronger after 50 activation cycles. Ir/$Ni_2P_4O_{12}$ exhibited enhanced electrochemical activity.

Apart from Raman spectroscopy, FT-IR is employed as a tool for analyzing the evolution of chemical functional groups of catalysts during in situ amorphization.[83] The distinction in molecular absorption spectra between the pre-catalyst and reconstructed catalyst enabled the identification of catalyst reconstruction and the amorphous species form. Yang and colleagues utilized FT-IR spectroscopy to explore the functional group states of Fe-Ni-Co-MOF during the activation process.[84] The absorption peak at 2976 cm^{-1}, associated with 2-methylimidazole in the pristine Fe-Ni-Co-MOF, was significantly weakened and ultimately disappeared, indicating a disruption in the structure of the MOF. 1,4-terephthalic acid transitions from acting as a bridging ligand to adopting monodentate and bidentate coordination forms. This change was evidenced by the positions of the carboxylate group's asymmetric and symmetric stretching vibration peaks at 102 and 252 cm^{-1}, respectively. The observed spacing of these peaks suggests that the bidentate mode is associated with the

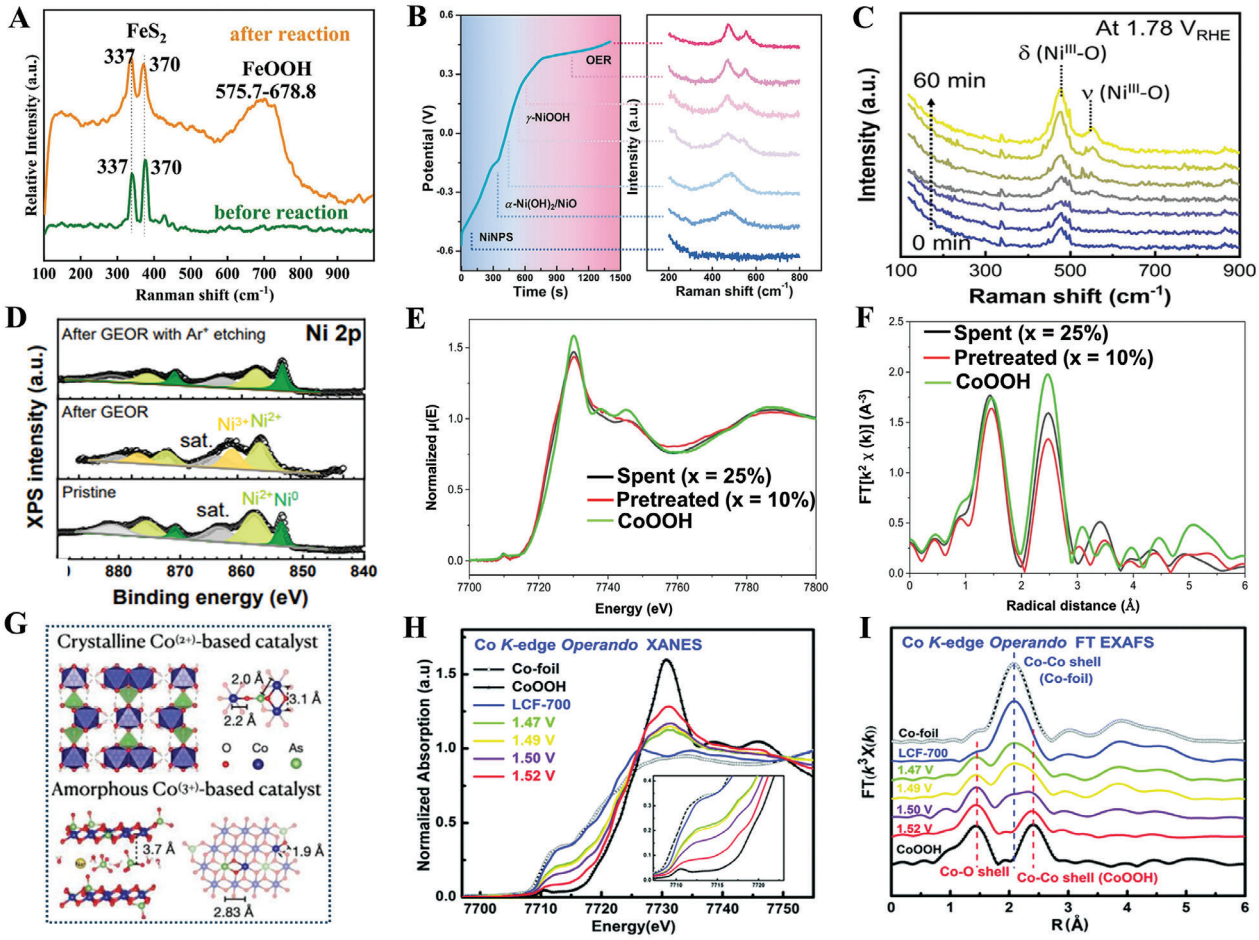

Figure 5. A) Raman spectra of pristine FeS_2 and amorphized FeS_2.[76] Copyright 2023, Elsevier. B) Chronopotentiometric analysis of NiPPS with an applied current at 0.5 mA (left), corresponding to the in situ Raman spectra at distinct potential (right).[79] Copyright 2019, Wiley. C) *Operando* Raman spectra of Au@NiS_x recorded during the GOR process. D) High-resolution XPS spectra of Ni 2p.[80] Copyright 2023, Wiley. E) XANES spectra and F) EXAFS spectra constructed in magnitude R space of the catalyst after pretreatment and usage.[30a] Copyright 2021, American Chemical Society. G) Structural schematic diagram of crystalline erythrite and amorphous cobalt oxide layer.[63] Copyright 2021, Wiley. H) *Operando* XANES and I) FT-EXAFS spectra of LCF at Co K-edge with applied potential in alkaline solution.[87] Copyright 2018, Royal Society of Chemistry.

crystalline-amorphous boundaries, whereas the monodentate mode occurs within the amorphous phase. Furthermore, the breakdown of coordination bonds between organic ligands and metal ions, facilitated by OH^- groups, resulted in the attenuation of absorption peaks at 754 and 547 cm^{-1}, reflecting the degradation of Co_2Fe-O/Co_2Ni-O clusters during electrochemical activation of Fe-Ni-Co-MOF. Importantly, the appearance of new absorption peaks at 582 cm^{-1} for M-O was attributed to the formation of metal oxides/hydroxide species in the amorphous regions. FTIR analysis can also identify the characteristics of in situ-formed amorphous species present in LiCoBPO and pakhomovskyite.[69,85]

3.4. X-Ray Photoelectron Spectroscopy and Absorption Spectroscopy

The amorphization of catalysts is generally associated with the formation of new phases during electrocatalysis, leading to variations in the chemical environment and electronic structure of the components. X-ray photoelectron spectroscopy and absorption spectroscopy are important techniques to unveil the evolution of catalyst's surface chemical properties and provide insights into the amorphous species.

X-ray photoelectron spectroscopy (XPS) analysis has been applied to gain insight into the chemical states of the in situ generated amorphous layer. Hus et al. detected the generation of an amorphous species on the Au@NiS_x during the glycerol oxidation reaction (GOR).[80] XPS analysis revealed a peak corresponding to Ni^{3+} on the amorphous surface (Figure 5D). This observation suggests a transition in the valence states of Ni species from Ni^{2+} to Ni^{3+} during the amorphization process. In the corresponding high-resolution O 1s and S 2p spectra, a pronounced strengthening of the nickel-oxygen (Ni-O) and sulfur-oxygen (S = O) bonds was observed, providing additional evidence for the oxidation of the Au@NiS_x. After the Ar^+ bombardment, the absence of Ni^{3+} in XPS spectra indicated that the amorphous layer has a depth of only a few nanometers.

X-ray absorption near edge structure (XANES) and extended X-ray absorption fine structure (EXAFS) techniques are highly effective in exploring the electronic and geometric structure of amorphized electrocatalysts, respectively. Nikolla et al. employed XANES and EXAFS to detect changes in the chemical environment of Co ions in various reconstructed catalysts.[30a] The pre-edge feature and energy position in XANES spectra reflected the average oxidation state of Co. The identification of the amorphous Co-OOH phase on the reconstructed catalyst was based on the overlapping signature XANES features of Co-OOH with emerging features (Figure 5E). Additionally, linear combination fitting analysis of the XANES spectra was performed to determine the proportion of amorphous Co-OOH present. EXAFS spectra were applied to indicate the changes in the local coordination environment of the catalyst. As depicted in Figure 5F, the peaks in the FT-EXAFS at Co K-edge were related to the distance of the Co atom, which is assigned to the coordination environment of Co. The amorphization of electrocatalysts induced a disruption for the long-range order of Co-Co distance (Figure 5G), which could be reflected in the FT-EXAFS fitting results.[63] The Debye-Waller factor obtained from the EXAFS fitting quantifies disorder within the crystal lattice, where deviations from the perfect alignment of atoms in the fcc structure increase the Debye-Waller factor.[51,86] According to the fitting results, the coordination numbers of Co cations could also be calculated.[69] The disorder in atomic arrangement and defect formation associated with amorphization in electrocatalysts can be characterized using EXAFS spectra.

In situ/*operando* XAS technologies unveil the evolution of the atomic scale structure during the electrochemical amorphization process. For instance, a 2 nm-thick amorphous layer emerged on the catalyst $LaCo_{0.8}Fe_{0.2}O_{3-\delta}$ (LCF) after the OER process.[87] *Operando* XAS at the Co/Fe K-edge was conducted to capture the development of the surface electronic structure in a self-developed electrochemical cell. Analysis of the *operando* XANES spectral indicated a gradual shift in the absorption edge, suggesting a change in the Co oxidation state as the applied potential increased (Figure 5H). At a potential of 1.52 V, the position of the absorption edge closely resembled that of the CoOOH reference, suggesting that the cobalt ions were predominantly in a trivalent state. The analysis of k^3-weighted FT-EXAFS spectroscopy at the Co K-edge revealed a gradual disappearance of the metallic Co-Co/Fe coordinated peak at ≈2.2 Å with increasing applied potential (Figure 5I). Additionally, distinct peaks matched with Co-O and Co-Co bonds in edge-sharing trivalent cobalt oxides/hydroxides were observed at high potential, suggesting the generation of CoOOH during the electrochemical oxidation process. Similar changes in iron can be observed through these *operando* XAS technologies at the Fe K edge. The author identified the amorphous layer as containing (Co/Fe)O(OH) species.

Analyzing the in situ XANES and EXAFS spectra of different electrocatalysts can uncover the factors affecting amorphization behaviors. An increase in the valence state of Co in both $CoFe_{0.25}Al_{1.75}O_4$ and $CoAl_2O_4$ was observed in the in situ Co K-edge XANES studies, which was reflected by the shift in the K-edges.[88] A significant valency increment in $CoFe_{0.25}Al_{1.75}O_4$ was observed at lower potentials, whereas $CoAl_2O_4$ exhibited similar behavior only at higher potentials. In situ Co K-edge FT EXAFS spectra indicated that applying a potential of 1.5 V led to a higher ratio of octahedral coordination in $CoFe_{0.25}Al_{1.75}O_4$ compared to $CoAl_2O_4$, suggesting a more complete transformation into amorphous oxyhydroxide. This suggests that Fe substitution facilitates the formation of amorphous species, thereby improving the catalyst's performance. In situ/*operando* XAS was highly effective for characterizing the amorphization processes of other catalysts, such as NiFe Prussian blue analogue,[35b] bimetallic carbide Mo_6Ni_6C,[44] and $Ba_{0.5}Sr_{0.5}Co_{0.8}Fe_{0.2}O_{3-\delta}$.[89]

Characterizing the in situ amorphization of electrocatalysts offers a crucial perspective in the field of catalysis research. By leveraging a diverse array of advanced characterization techniques, including XRD, TEM, XPS, XAS, and Raman spectroscopy, researchers have gained a profound insight into the dynamic structural changes occurring within catalysts during electrochemical processes. Such approaches not only shed light on the formation and behavior of amorphous species but also unravel the intricate mechanisms underlying catalyst evolution under varying electrocatalytic conditions. Through a detailed exploration of these characterization techniques, the perspective on in situ amorphization transcends mere observation, offering a deeper understanding of catalyst performance, stability, and the tailored design of efficient electrocatalytic systems for sustainable energy applications.

4. Regulation of In Situ Amorphization Process

In situ amorphization during electrochemical processes leads to the formation of new phases that significantly impact the catalytic performance. Typically, the active sites are primarily located within the in situ amorphous structure.[90] The gradual progression of amorphization from the surface toward the bulk populates the number of active sites, while excessive amorphization may induce deterioration of catalytic activity.[21] Amorphous species possess high intrinsic activity because of their disordered and unsaturated coordination structures. However, their introduction can lead to poor conductivity and insufficient stability in harsh electrochemical conditions.[91] A too-thin layer of in situ formed amorphous species may have limited activity, whereas a too-thick layer might cause the conductive structure to collapse.[92] Yang's group studied the interfacial charge-transfer behavior of amorphized $Lu_2Ir_2O_7$ through electrochemical impedance spectroscopy (EIS). They found that the amorphous (oxy)hydroxide IrOOH is conducive to electronic transfer during the OER. Nonetheless, excessive amorphization led to an increase in charge-transfer resistance.[93] The high electrocatalytic activity of amorphized catalysts in both OER and HER is attributed to the balance between having adequate active sites and maintaining good conductivity.[22,94]

Thus, manipulating amorphization presents a crucial step toward achieving efficient and stable electrocatalysts. This section elucidates specific principles for optimizing amorphization, focusing on two critical aspects, namely precatalyst regulation and external test conditions.

4.1. Precatalyst Modulation

Since the reconstruction of electrocatalysts is closely linked with their physicochemical properties,[95] many strategies, including

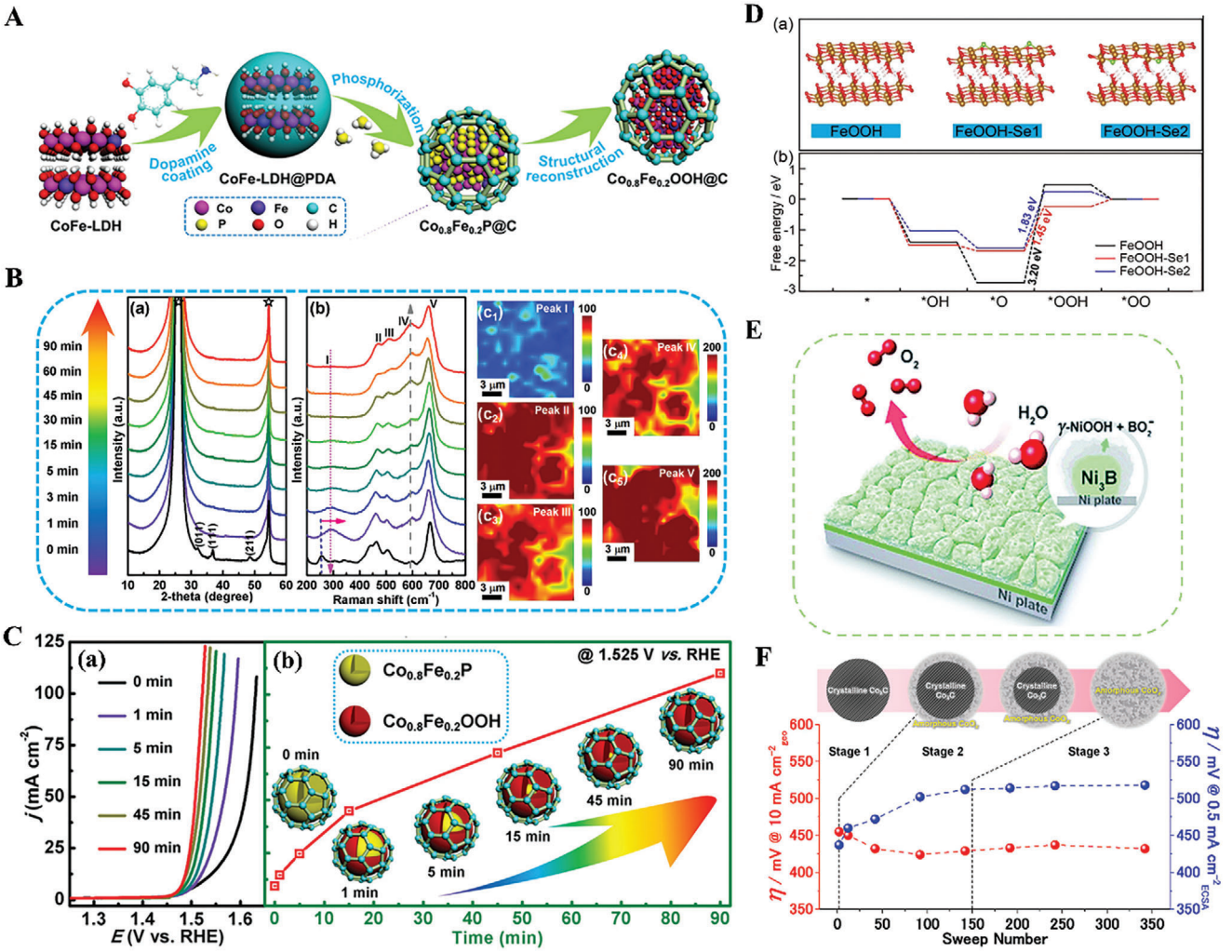

Figure 6. A) A schematic representation of the synthesis process for $Co_{0.8}Fe_{0.2}P$@C and its subsequent amorphization process. B) Ex situ XRD patterns a) and Raman spectra b) for the $Co_{0.8}Fe_{0.2}P$@C in different reaction times. Raman mapping images corresponding to the peaks in Figure b after 90 min of electrochemical activation c). C) Polarization curves a) and corresponding current density at 1.525 V versus RHE b) were recorded for the $Co_{0.8}Fe_{0.2}P$@C following electrochemical oxidation at various time points (1, 5, 15, 45, and 90 min). Inset: schematic depiction illustrating the structural amorphization process of $Co_{0.8}Fe_{0.2}P$@C along with electrochemical oxidation.[18a] Copyright 2020, Wiley. D) Structural models for FeOOH and FeOOH doped with selenium, the colors orange, red, and green denote the Fe atoms, O atoms, and Se atoms, respectively a). The free energy profiles for FeOOH with and without Se atoms during the OER at 1.23 V (b).[102] Copyright 2019, American Chemical Society. E) A schematic diagram illustrating the in situ generation of an amorphous layer on the Ni_3B catalyst.[104] Copyright 2019, Royal Society of Chemistry. F) Electrochemical sweep on Co_3C led to in situ amorphization, resulting in the change of OER overpotentials (η). Red curve represents data based on geometric electrode surface area, while blue curve corresponds to data based on electrochemically active surface area (ECSA).[38] Copyright 2018, American Chemical Society.

modulation of precatalysts' chemical composition, crystallinity, and surface structure, have been developed to shape the in situ amorphization process during the electrocatalytic process.

4.1.1. Anions Regulation

Many metal non-oxide materials, such as metal chalcogenides, metal pnictides, and borides, exhibit noticeable in situ reconstruction under electrocatalysis, resulting in the generation of an amorphous structure, unlike their oxide counterparts.[96] Metal non-oxide catalysts, characterized by weaker M-X (X = S, Se, Te, P, N, B) bonds compared to M-O bonds, are more susceptible to electrochemistry-induced reconstruction than their oxide counterparts.[97]

The substitution of metal oxide with metal non-oxide would help to initiate the reconstruction of catalysts. For example, the complete phosphorization of metal materials was applied to the fabrication of amorphous (oxy)hydroxides during electrocatalysis. Qiu et al. reported that $Co_{0.8}Fe_{0.2}P$@C synthesized by low-temperature phosphorization of CoFe-layered double hydroxides coated with a polydopamine shell (CoFe-LDH@PDA) underwent phosphate leaching and induced structural reconfiguration during OER (**Figure 6A**).[18a] Analysis of the XRD pattern and Raman spectra of $Co_{0.8}Fe_{0.2}P$@C revealed the weakening and disappearance of Co-P peaks (Figure 6B). No new peaks of the crystal phase

emerge in the XRD pattern as the prolonged oxidation treatment time, and peaks of Fe-O and Fe-OH gradually became stronger in the Raman spectra. This process ultimately results in lattice distortion and in situ amorphization of the catalyst. Eventually, full amorphization of $Co_{0.8}Fe_{0.2}P$@C was achieved through the complete leaching of phosphorus species (Figure 6C). In contrast, for crystalline CoFe oxyhydroxide, only surface reconstruction occurred. The amorphous $Co_{0.8}Fe_{0.2}OOH$@C demonstrates efficient oxygen evolution. It should be noted that many phosphides only induced an amorphous layer during the in situ electrochemical activation, such as hyperbranched NiCoP,[98] hierarchical flower-like NiCoP,[99] and NiFeP.[100]

Other metal non-oxide, such as sulfides, selenides, and borides, have been utilized as electrocatalysts due to their intrinsic chemical nature.[101] These properties also enable them to undergo conversion to amorphous (oxy)hydroxides during the electrocatalysis. The formation of $Ni(OH)_2$/NiOOH heterojunction, achieved via selenium leaching of $NiSe_2$ during both HER and OER in an alkaline condition, enhanced the water splitting performance.[48] Furthermore, Wang and colleagues synthesized amorphous Se-doped FeOOH through in situ electrochemical reconstruction of the FeSe precatalyst, leading to a lower energy barrier for the rate-determining step during the OER process compared with FeOOH (Figure 6D).[102] Borides can also regulate the formation of an amorphous phase while retaining metaborate, thereby enhancing the catalytic performance of the amorphous species.[103] Unlike pristine nickel, Ni_3B facilitates amorphization during OER.[104] The surface of Ni_3B was predominantly occupied by an amorphous layer with a thickness of 30–50 nm, whereas nickel plates exhibited a rough surface with a 2 nm-thick amorphous layer after OER. Moreover, the amorphous (oxy)hydroxide layer containing metaborate species optimizes the catalytic activity of the catalyst (Figure 6E). Cheng et al. also reported that the in situ-formed amorphous (oxy)hydroxide with oxyanions has a higher electrocatalytic activity compared to the counterpart with additive oxyanions on (oxy)hydroxide.[105] Thus, the rational design of anions for non-oxide metals could regulate the constituents and activity of the amorphous phase.

For metal non-oxides, in situ amorphization leads to the formation of (oxy)hydroxides is a common phenomenon. However, some studies also suggest in situ formation of amorphous oxides in these materials. In harsh electrolytes for electrocatalytic oxidation, metal non-oxides are typically partially or fully oxidized to the corresponding amorphous metal oxides. For example, Co_3C was fully converted into amorphous CoO_x as a result of the electrochemical sweep (Figure 6F).[38] Amorphous metal oxides also can be formed in the CoS,[106] NiS,[62] and Mn_3N_2 systems,[39] during the electrochemical process.

Alternatively, incomplete sulfur (S) leaching of sulfides can lead to the generation of amorphous oxysulfide during in situ electrochemical processes. Liu et al. engineered a spinel $NiCo_2S_4$ catalyst by substituting sulfur (S) anion for $NiCo_2O_4$, which possesses a metastable spinel structure. This structure facilitates its amorphization under electrocatalysis (**Figure 7A**).[107] However, $NiCo_2O_4$ with a robust spinel structure shows minimal change after OER. Given that S is bonded to both Co and Ni sites in the $NiCo_2S_4$ spinel structure, alterations in the Co and Ni atom's coordination environment were detected in the extended EXAFS spectra and analyzed through wavelet transform (WT). Co-O bonds emerged during amorphization as sulfur dissolved from Co-S, while S bound to the Ni site remained, demonstrating the formation of amorphous oxysulfide after the reaction (Figure 7B,C). The oxysulfide structure, comprising both oxygen and sulfur anions, demonstrates superior inherent electrocatalytic activity for OER compared to structures with a single anion. Similar surface oxysulfide was also observed during the in situ amorphization of Ni_3S_2.[108] On the amorphous surface, the distribution of Ni, S, and O suggested that sulfur anions diffused from the bulk to the surface during prolonged electrochemical activation (Figure 7D). The rapid oxidation of sulfides occurring on the surface created a concentration boundary layer, which induced ion diffusion along the gradient (Figure 7E). Consequently, the amorphous oxysulfide shell emerged because of Fick's second law. Figure 7F illustrates the structure evolution process with the sulfur anionic regulation. This process results in the establishment of stable oxysulfide shells, which create efficient active sites for oxygen evolution.

The unstable of metal non-oxides can promote in situ amorphization during electrocatalytic reaction, leading to the formation of various amorphous structures. Furthermore, the introduction of heteroatoms, such as phosphorus, sulfur, selenium, which typically possess lower electronegativity than oxygen, serves to optimize the precatalyst's electronic structure, thereby impacting the amorphous reconstruction. Fan and coauthors reported that S doping on the $Ni_xFe_y(OH)_2$ (S-NiFeLDH) could decrease the energy barrier for precatalyst reconstruction and enhance its transformation to amorphous NiOOH.[109] The amorphization in S-NiFeLDH is more pronounced than in NiFe-LDH. In the case of precatalysts with stable crystalline structures, the leaching of dopants benefits surface amorphization during the electrochemical activation. Liu et al. discovered that phosphorus-doped $NiFe_2O_4$ could promote the amorphization process to form amorphous oxyhydroxides.[110] Depth-profiling X-ray photoelectron spectroscopy technique (DP-XPS) was employed to explore the breakdown of metal-phosphorus (M-P) bonds following electrochemical activation, revealing a noticeable variation in P content from the surface layer of the catalyst to the bulk (Figure 7G). The dynamic alteration of phosphorous content could lead to the formation of an amorphous layer. Even in neutral electrolyte conditions, the surface of $LiCoPO_4$ can transform into an amorphous structure, accompanied by phosphorus leaching during CV testing. In contrast, $LiCo_2O_4$ was restructured into a spinel-like structure at pH 7.[27] The dopant fluorine anion, being highly electronegative, induces the formation of amorphous species with excellent electrocatalytic activity.[111] Fluorine-doped NiFe electrocatalysts prompted the formation of a thicker amorphous shell and the creation of defects within it, exhibiting elevated intrinsic electrochemical activity (Figure 7H,I).[112] The formation of amorphous species could also be triggered by the leaching of other anions dopants, such as chlorine,[113] selenium,[114] and tellurium.[115]

Furthermore, the incorporation of oxygen-containing anions into electrocatalysts could regulate its electronic structure, facilitating the formation of (oxy)hydroxides and enhancing electrocatalytic activity, such as borate ions (BO_3^{3-}) and $[Cr(C_2O_4)_3]^{3-}$.[116] Under the potential induction in strongly alkaline conditions, the complete loss of phosphate in $Co_3(OH)_2(HPO_4)_2$ could give rise to an amorphous $CoO_x(OH)$ structure in both OER and HER.[50]

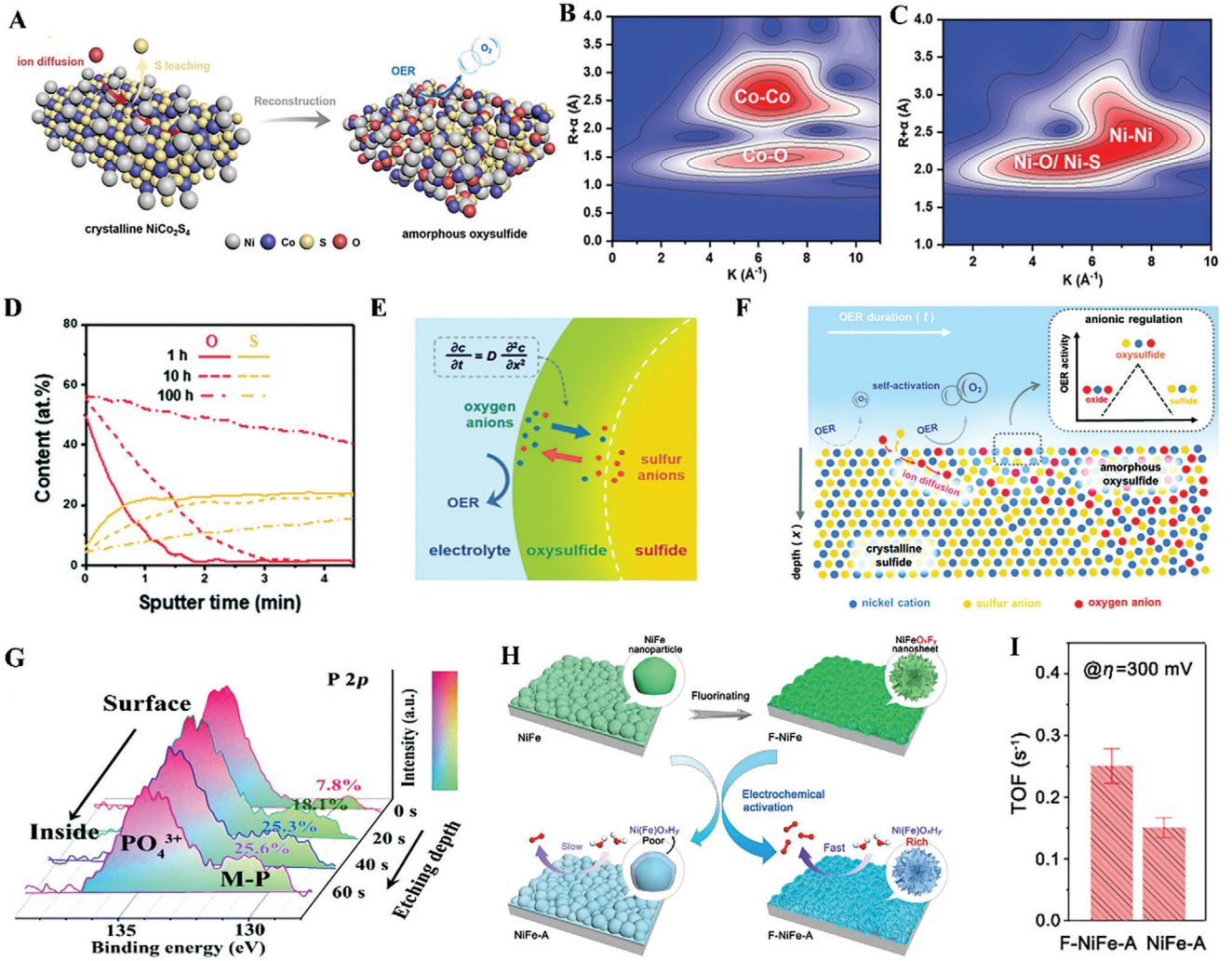

Figure 7. A) Schematic representation of the reconstruction mechanism occurring on $NiCo_2S_4$. Morlet wavelet transform of the k^3-weighted B) Co K-edge EXAFS and C) Ni K-edge EXAFS spectra for post $NiCo_2S_4$, respectively.[107] Copyright 2023, Wiley. D) Depth-profiling of auger electron spectroscopy analysis reveals elemental content within Ni_2S_3 following different durations of OER activation. E) Formation of oxysulfide layer via ion diffusion under electrochemical activation. F) Full scenario to illustrate the generation of oxysulfide amorphous layer under the OER conditions.[108] Copyright 2022, Royal Society of Chemistry. G) XPS core level spectra of P 2p corresponding to various Ar^+ etching periods.[110] Copyright 2020, Royal Society of Chemistry. H) Comparison of surface reconstruction and I) turnover frequency (TOF) value for NiFe-electrocatalyst with and without F doping after electrochemical activation.[112] Copyright 2021, American Chemical Society.

The introduction of heteroatoms renders the catalyst more prone to amorphization during electrochemical activation, primarily due to the in situ self-leaching of these heteroatoms. On the other hand, the incorporation of heteroatoms may lead to the leaching of other ions or co-leaching with other elements, manipulating the amorphization processes. The doping of chlorine regulates the amorphization process of $LiCoO_2$ (**Figure 8A**), reducing the applied potential to initiate in situ Co oxidation and delithiation during the OER, rather than inducing amorphization through Cl leaching.[117] As shown in Figure 8B, an amorphous Co (oxy)hydroxide layer was observed on the cycled $LiCoO_{1.9}Cl_{0.1}$, progressively thickening on the cycled $LiCoO_{1.8}Cl_{0.2}$. The amorphous layer exhibited similar atomic ratios of cobalt and chlorine as the pristine catalyst (Figure 8C), indicating minimal loss of Cl and Co during amorphization. In contrast, facile and rapid lithium extraction from $LiCoO_{1.8}Cl_{0.2}$ was noted through the inductively coupled plasma mass spectrometry (ICP-MS) analyses (Figure 8D). Furthermore, cobalt oxidation of $LiCoO_{1.8}Cl_{0.2}$ could be fully completed at 1.5 V versus RHE, preventing further oxidation to Co^{4+} (Figure 8E,F). The amorphous structure can terminate the surface amorphization by preventing further Li extraction and Co oxidation, thereby manipulating the dynamic surface reconstruction. The surface of cycled $LiCoO_2$ underwent reconstruction into spinel-type $Li_{1\pm x}Co_2O_4$ ($0 < x < 1$). Figure 8G,H show the Density functional theory (DFT) calculation results, Cl doping shifted the reconstruction reaction path largely downhill, rendering delithiation energetically favorable. On the contrary, more energy was required for cobalt oxidation and lithium extraction during the electrochemical activation of $LiCoO_2$.

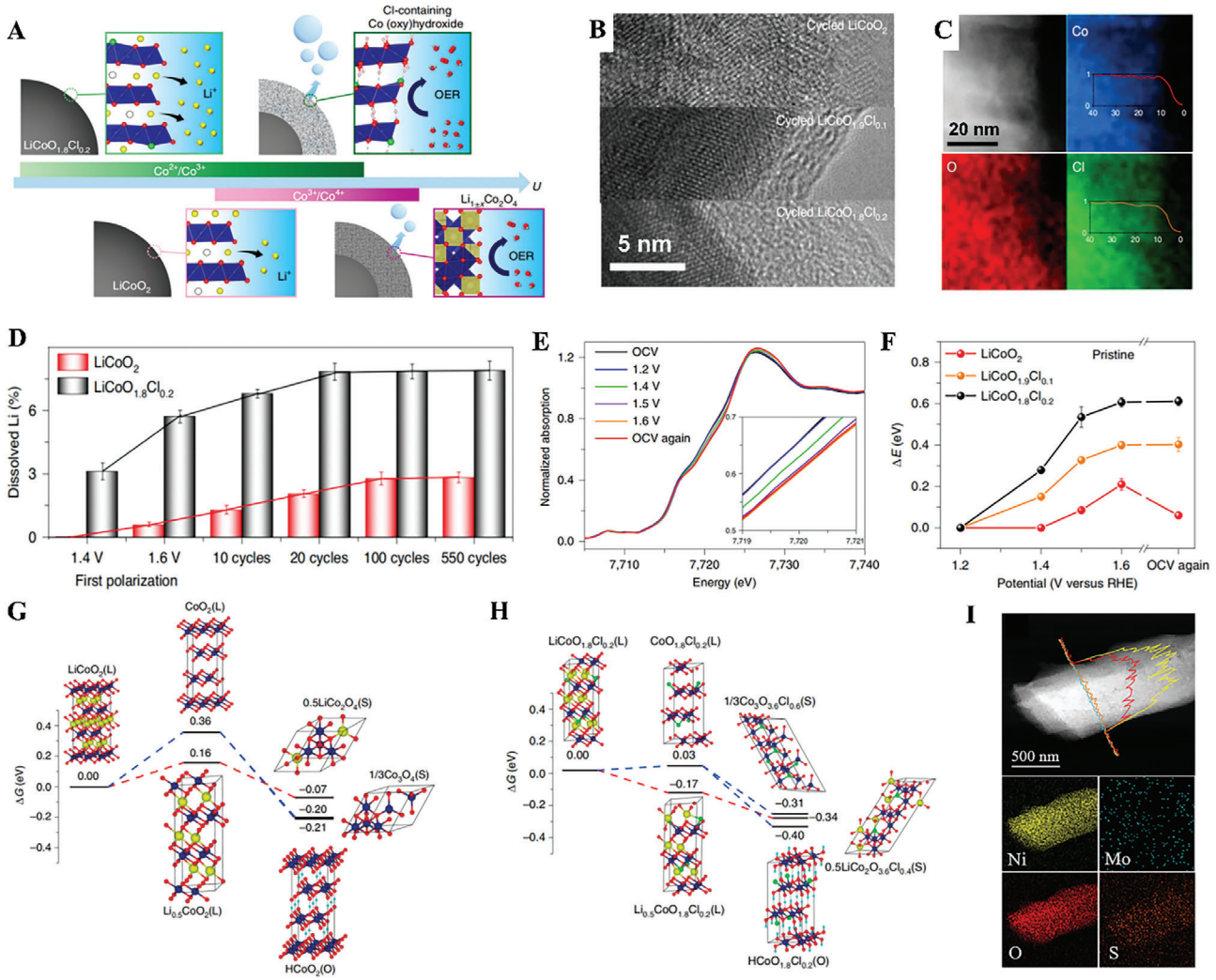

Figure 8. A) Schematic illustration of the variance in surface reconstruction between $LiCoO_2$ and $LiCoO_{1.8}Cl_{0.2}$ during electrochemical activation. B) TEM images of the Post-$LiCoO_{2-x}Cl_x$ (x = 0, 0.1 or 0.2) after electrochemical cycles. C) HAADF-STEM image and EDS mapping for the surface amorphous region of $LiCoO_{1.8}Cl_{0.2}$. Inset: EDS line cut. D) The amount of Li in the solution after electrochemical cycles. E) XANES spectra at the Co K-edge of $LiCoO_{1.8}Cl_{0.2}$ with the applied potential. F) Variations value in Co K-edge shifts at different potentials for $LiCoO_{1.8}Cl_{0.2}$. Energy profile calculated for the reconstruction reaction of G) $LiCoO_2$, and H) $LiCoO_{1.8}Cl_{0.2}$ at 1.6 V versus RHE.[117] Copyright 2021, Nature Portfolio. I) HR-TEM images accompanied by line-scan energy dispersive spectrometer pattern and mappings of Ni, Mo, O, and S elements of reconstructed NiMoOS.[118] Copyright 2022, Wiley.

Furthermore, the co-leaching of heteroatoms can also accelerate the formation of amorphous species. The introduction of S dopant in NiMoOS accelerated the dissolution of MoO_4^{2-} during OER activation, thus an amorphous structure was quickly formed through crystal collapse.[118] The reactive M-S coordination destabilized the outer layer during electrochemical activation, leading to the co-leaching of Mo and S species for fast reconstruction (Figure 8I). A similar co-leaching phenomenon can be observed in P-doped NiS,[119] CoP_3-NiS nanowire arrays,[120] and B,Co-NiS.[78] Moreover, the doping of S in CoP results in the formation of oxides/hydroxides containing sulfur.[121] The author explained that the S in CoP exhibits higher oxidation resistance compared to P during the OER process. Variations in heteroatom doping among electrocatalysts can lead to the formation of diverse amorphous structures, which influence the electrochemical conversion of organic molecules or facilitate water splitting.

In the process of anion regulation, the increased instability of the catalyst leads to the in situ amorphization with the dissolution of anions. However, there has not yet been systematically investigated how different anions and doping methods induce varying degrees of amorphization and affect the activities of the amorphous species. Furthermore, it can also be inferred that the composition of different cations ultimately influences the in situ amorphization process.

4.1.2. Cation Regulation

Strategies involving metal cation substitution or doping can significantly improve the electrocatalytic activity of otherwise inactive electrocatalysts.[88] This approach could influence the stability of precatalysts and facilitate the involvement of lattice

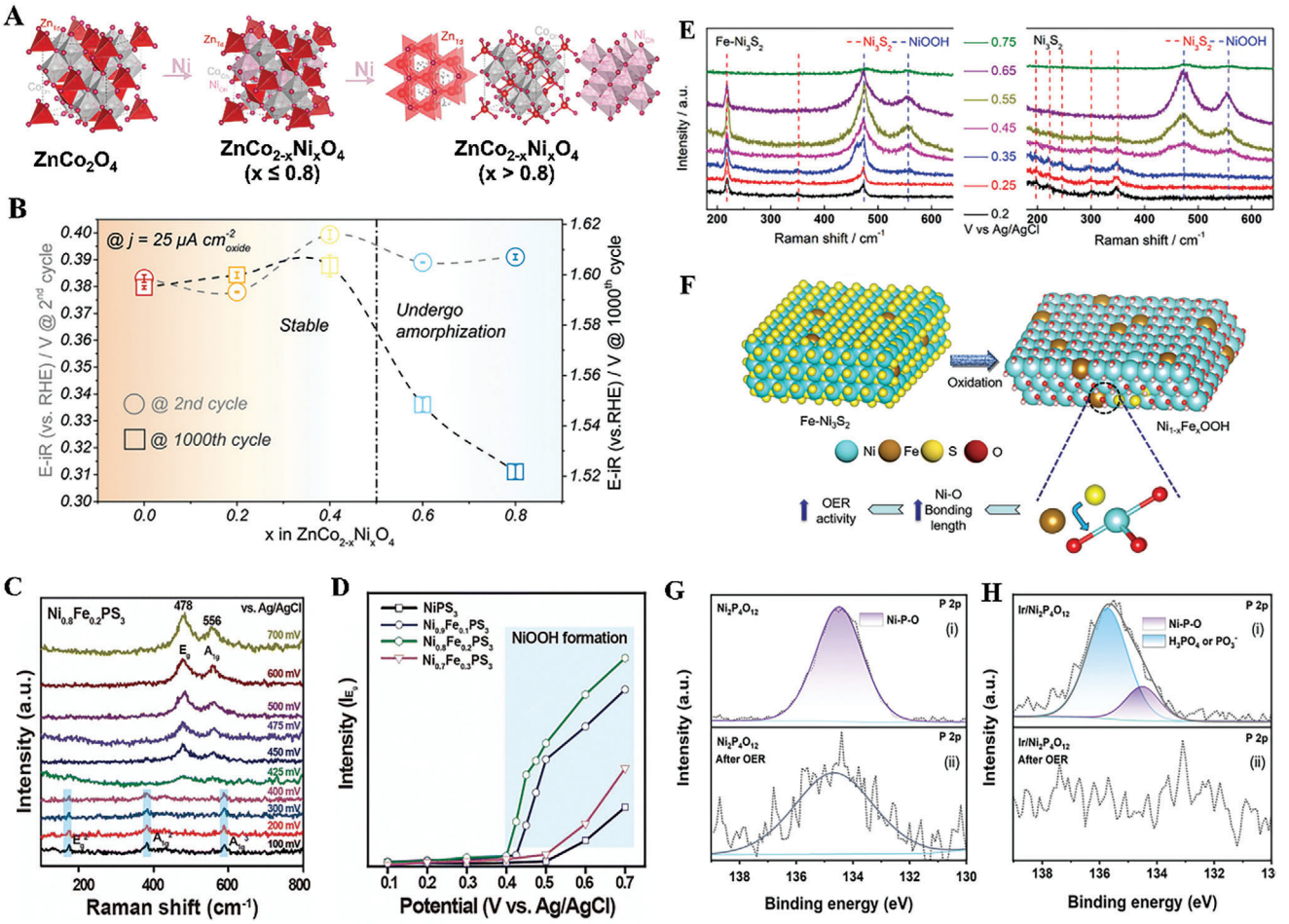

Figure 9. A) Crystal structure changes of the Ni-substituted $ZnCo_2O_4$. B) *iR*-corrected potential (*vs* RHE) at the fixed current density for $ZnCo_{2-x}Ni_xO_4$ (x = 0.0, 0.2, 0.4, 0.6, 0.8) after different electrochemical cycles.[122] Copyright 2019, Wiley. C) In situ Raman spectroscopy of $Ni_{0.8}Fe_{0.2}PS_3$ at various applied potentials. D) Intensity of NiOOH peaks in the in situ Raman spectra for $Ni_xFe_{1-x}PS_3$ under different potentials.[127] Copyright 2023, Royal Society of Chemistry. E) Characterization of Fe-Ni_3S_2 and Ni_3S_2 via in situ Raman spectroscopy. F) Schematic diagram illustrating the phase transformation of Fe-Ni_3S_2 during electrochemical activation.[130] Copyright 2022, Wiley. Comparison of high-resolution XPS spectra of the P 2p for G) $Ni_2P_4O_{12}$ and H) Ir/$Ni_2P_4O_{12}$ before and after electrocatalytic reaction.[82] Copyright 2023, Wiley.

oxygen, thereby regulating the amorphization process during the electrocatalytic process. Xu's group discovered that substituting Ni into $ZnCo_2O_4$ spine structure ($ZnCo_{2-x}Ni_xO_4$) led to instability and the absence of a spinel structure (**Figure 9A**).[122] The amorphization of $ZnCo_{2-x}Ni_xO_4$ after 1000 electrochemical cycles, driven by its instability, triggered a change in the overpotential at 25 μA cm^{-2} (Figure 9B). The ratios between metal cations as well as the ratios between metal cations and anions could influence the degree of amorphization. For example, an amorphous surface can be formed on the $Ba_{0.5}Sr_{0.5}Co_{0.8}Fe_{0.2}O_{3-\delta}$ (BSCF),[123] whereas the $Ba_4Sr_4(Co_{0.8}Fe_{0.2})_4O_{15}$ maintains its crystal structure during the OER process.[124] Similarly, the amorphous phenomena are more pronounced in Ni_2P_5 compared to Ni_2P,[125] and in W_2CoB_2 compared to WCoB.[126]

The optimal stoichiometry of the cation dopant accelerates the formation of active species on the amorphous layer. Fe-doped Ni thiophosphate ($Ni_xFe_{1-x}PS_3$) underwent in situ surface amorphization, resulting in the formation of amorphous oxide layers at low applied potential.[127] In situ Raman spectroscopy measurements indicated that the applied potential for developing amorphous NiOOH was lower on $Ni_{0.8}Fe_{0.2}PS_3$ compared to other $Ni_xFe_{1-x}PS_3$ (Figure 9C). Therefore, more amorphous NiOOH species were generated for $Ni_{0.8}Fe_{0.2}PS_3$ (Figure 9D). Additionally, the regulation of Fe in NiPS is advantageous for inducing the formation of an amorphous layer on $Ni_{0.85}Fe_{0.15}PS$, facilitating the presence of metal sites at the near-surface area with a relatively high valence state.[128] Varying compositions of metal cations can regulate the electronic structure of perovskites, thereby influencing the reconstructed structures. Yang and coworkers reported that $Sr_4Mn_2CoO_9$ exhibited a larger surface amorphization region compared to $Sr_6Co_5O_{15}$, in contrast to the crystalline stability observed in $LaCoO_3$.[129] However, the underlying reason for amorphization triggered by metal substitution requires additional investigation.

Regulating the metal ratio in precatalysts can alter the electronic structure, influencing the amorphization process and the activity of amorphous species during in situ electrochemical activation. In addition, metal doping or substitution can modify

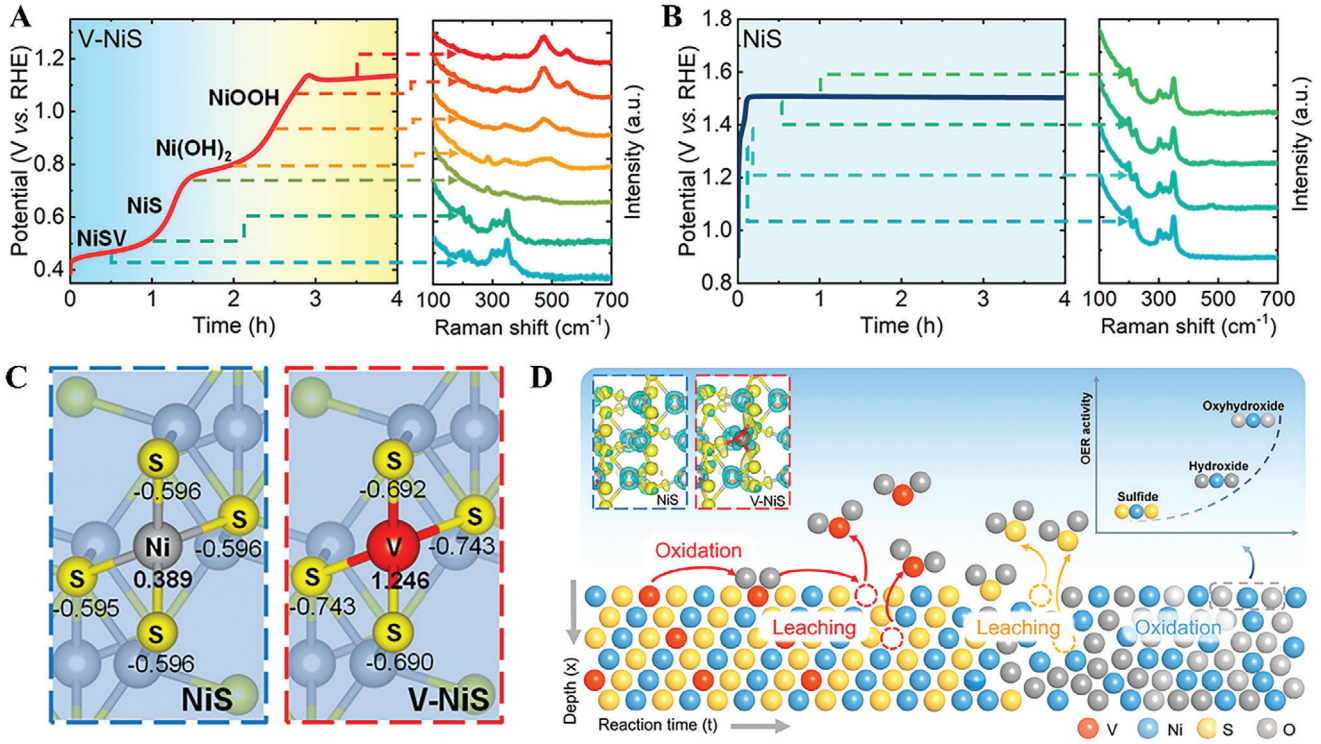

Figure 10. *Operando* Raman spectra of A) V-NiS and B) NiS during the electrochemical activation process. C) Density functional theory calculations of Bader charges for NiS and V-NiS. D) Schematic of the evolution of amorphous structure induced by vanadium leaching of V-NiS.[49] Copyright 2023, American Chemical Society.

the dissolution of the unstable phase, thereby affecting the generation of the amorphous phase. Ren and co-authors demonstrated that Fe-doped Ni_3S_2 accelerated the generation of amorphous NiOOH species, along with residual sulfur.[130] As revealed by in situ Raman spectra, the dissolution of S was inhibited by the incorporation of Fe (Figure 9E). The presence of substantial residual S in Fe-Ni_3S_2 led to an extended Ni-O bond in NiOOH, enhancing electrocatalytic activity for both oxygen evolution reaction and urea oxidation reaction (Figure 9F). The prevention of sulfur leaching can also be observed when Fe is doped into NiO/NiS_2.[131]

At times, the introduction of metal elements expedites the release of unstable components, promoting the amorphization process. Zhou et al. proposed decorating individual metal atoms (Ir) on $Ni_2P_4O_{12}$ to facilitate the leaching of PO_4^{3-}, achieving a much thicker amorphous structure on $Ir/Ni_2P_4O_{12}$ than on $Ni_2P_4O_{12}$.[82] In situ Raman spectroscopy demonstrated that $Ir/Ni_2P_4O_{12}$ required fewer activation CV cycles to generate amorphous NiOOH species. Additionally, it exhibited significantly stronger NiOOH signals after 50 CV cycles, implying enhanced electrochemical amorphization in $Ir/Ni_2P_4O_{12}$. XPS analysis indicated an increase in PO_4^{3-} leaching with the incorporation of single Ir atoms into $Ni_2P_4O_{12}$ (Figure 9G,H), reinforcing the reconstruction to form amorphous active species. Theoretical calculations revealed a significant reduction in the energy barriers to release PO_4^{3-} from the surface of $Ni_2P_4O_{12}$ in the presence of an Ir atom. Similarly, other metal cation dopants can also enhance the leaching of unstable elements, leading to their transformation into amorphous species, such as chromium-doped nickel sulfide.[132]

The introduction of unstable cations into precatalysts can induce highly efficient amorphization through their leaching during the electrochemical process. Pan et al. modified NiS by introducing vanadium cations, facilitating the formation of amorphous NiOOH through in situ V leaching at a lower potential.[49] *Operando* Raman spectra in **Figure 10A** identify the generation process of NiOOH, originating from the breakdown of the V-S bond with the oxidation of V. The cleavage of V-S bonds led to S leaching and the oxidation of Ni before reaching a potential of 1.2 V. In contrast, the active transformation of NiS to NiOOH took place at high applied potentials (Figure 10B). DFT calculations were employed to investigate the leaching mechanism of V at low potential. The Bader charge analysis revealed that the substituted V (1.246 e) has a much higher charge than the original Ni (0.389 e) (Figure 10C), leading to an orderly increase in the degree of ionization that enhances the leaching of the catalyst. Figure 10D illustrates the amorphization process of V-NiS. The doping of unstable V induced changes in electron distribution, making the cleavage of V-S bonds more susceptible. Amorphous species formed by V leaching facilitated the electrocatalytic process. The leaching of unstable cations to accelerate the generation of amorphous structures has been observed in other studies. The V leaching in V-doped Ni_2P created a disordered Ni structure.[133] Sacrificial W in CoFeW sulfide could induce metal cation vacancies, which benefited in situ reconstruction.[134] Qiu et al. reported that the substitution of Fe into metallic nickel can facilitate

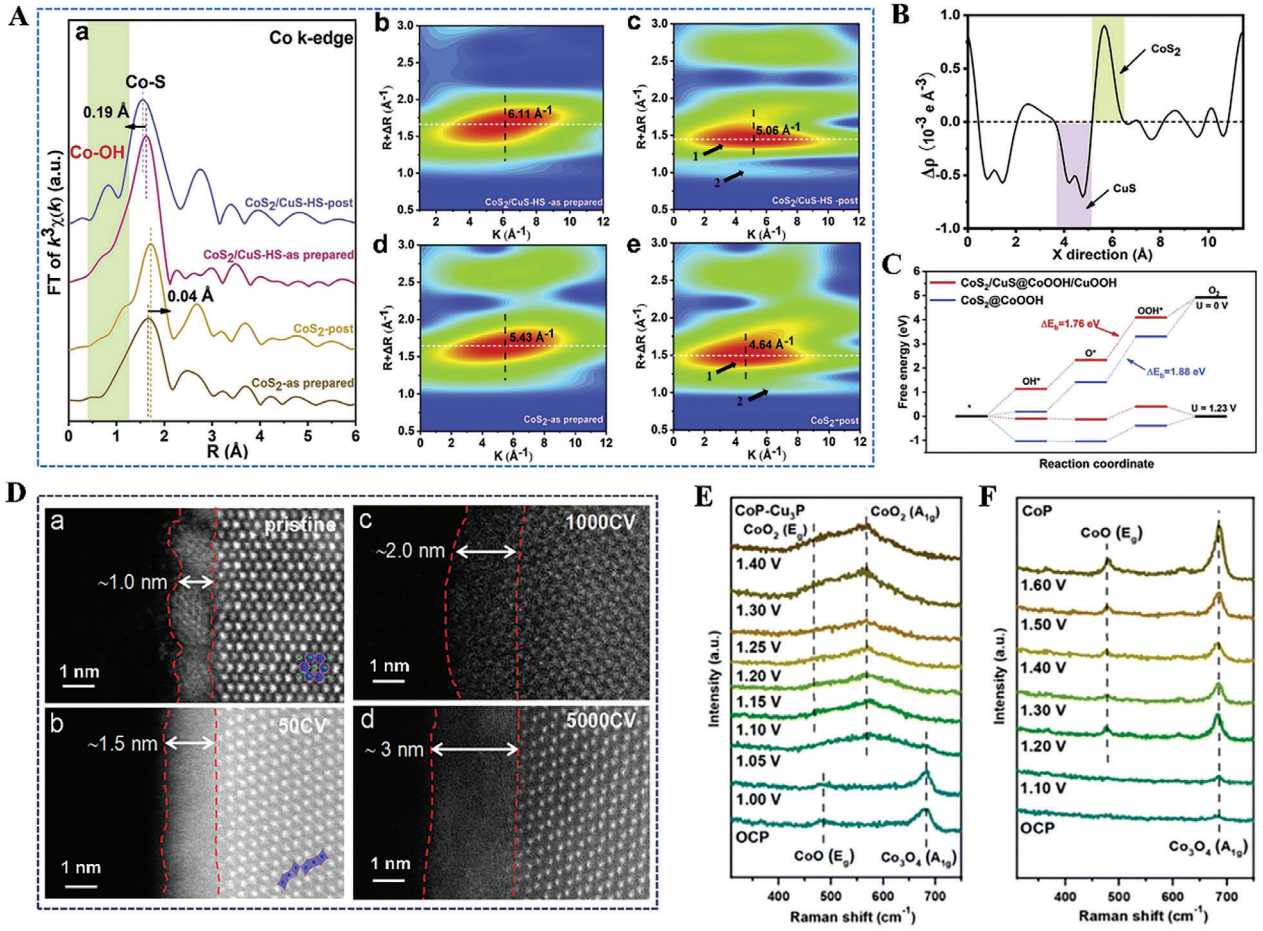

Figure 11. A) FT-EXAFS spectra of Co K-edge a) and WT-EXAFS contour plots (b-e) of the pristine catalyst and the reconstructed catalyst. B) Calculation of planar average electron density difference for CoS_2/CuS. C) Free energy diagrams were theoretically calculated for CoS_2@CoOOH and CoS_2/CuS@CoOOH/CuOOH at different applied potentials during the oxygen evolution process.[138] Copyright 2022, Cell Press. D) HAADF-STEM images with lattice-resolved details illustrate the structure evolution for IrO_x/9R-$BaIrO_3$ during acidic OER(a-d). The inserted structures on the HAADF-STEM images represent the simulated configurations of 9R-$BaIrO_3$, featuring the exposed (001) facet and two face-shared IrO_6 octahedral trimers following the leaching of Ba. The green balls represent Ba, the blue balls represent Ir, and the red balls represent O.[142] Copyright 2021, American Chemical Society. In situ Raman spectroscopy was performed on the E) CoP-Cu_3P electrode and F) CoP electrode.[143] Copyright 2023, Royal Society of Chemistry.

surface transformation into highly active FeNi-oxyhydroxides, which was associated with the oxidation and partial leach out of Fe atoms.[135] Moreover, Zn leaching in $ZnCo_2O_4$ enhanced the amorphization of the near-surface part.[136]

Doping cations induce instability in electrocatalysts, leading to their amorphization at lower potentials and the formation of highly active amorphous phases. The types and proportions of cations in precatalysts exert influence on their electronic structure, resulting in disparities in the development of amorphous structure. Therefore, it is crucial to establish the relationship between the electronic structure of precatalysts and amorphous reconstruction in future research.

4.1.3. Phase Structure Tuning

Designing a heterostructure by combining different phases to achieve mutual advantages is considered an effective method for boosting the amorphization process and improving structural properties.[137] This section will discuss the influence of heterostructures on the amorphization process during electrocatalysis.

The amalgamation of distinct phase for precatalysts supports the in situ amorphization, thereby facilitating the formation of highly active and stable amorphous species. Song et al. introduced a heterostructure CoS_2/CuS with a built-in electric field, which rapidly amorphized into an (oxy)hydroxide during electrocatalysis.[138] The peak of Co-OH was more pronounced and intense in CoS_2/CuS-post than in CoS_2-post (**Figure 11A**). The calculated formation energy of amorphous (oxy)hydroxide on CoS_2/CuS was notably lower than that on CoS_2, indicating the favorable growth of oxyhydroxide species along the heterointerface. Based on the calculated results of the planar average electron density difference along the X-direction (Figure 11B), electrons were transferred between CuS and CoS_2 on the interface, causing holes to accumulate in CuS. This phenomenon suggested the

formation of a built-in electric field within the catalyst through charge polarization, thereby enhancing the rate of electron transfer during the electrochemical reaction. A more intrinsically disordered atomic structure in the CoS_2/CuS-post compared to the CoS_2-post enhanced energy conversion during electrocatalysis (Figure 11C). Heterostructures that promote the generation of amorphous phases have also been observed in other research studies, such as $NiFe_2O_{4-x}/NiMoO_4$[139] and heterostructure catalyst (W-CoO) wherein CoO nanowire arrays were hybridized with tungsten nanoparticles.[140]

A heterostructure with electronic coupling effects facilitates the formation of amorphous oxyhydroxide species, boosting electrocatalytic performance. Conversely, heterostructure $SrCo_{0.8}Fe_{0.5-x}O_{3-\delta}/Fe_xO_y$ restricted Sr^{2+} leaching from $SrCo_{0.8}Fe_{0.5-x}O_{3-\delta}$, resulting in the formation of a thin amorphous CoFe (oxy)hydroxide layer, while retaining its perovskite structure.[141] The single-phase $SrCo_{0.8}Fe_{0.5-x}O_{3-\delta}$ encountered a more rapid and extensive surface Sr^{2+} dissolution during OER, resulting in a thicker amorphous layer. The extensive collapse of the perovskite structure would reduce the stability of the catalyst. The author speculated that Fe_3O_4 interacts robustly with the perovskite phase to mitigate surface Sr^{2+} leaching, attenuating the amorphization process. The modulation of in situ-generated amorphous species by heterostructures of the precatalyst highly depends on the properties of these two phases.

Modulating the interfacial electronic structures of the heterostructure could influence the activity of in situ formed amorphous species. Highly active amorphous species can form on the heterostructure electrocatalyst during electrochemical activation. Yan and coworkers reported that a heterostructure catalyst, formed by anchoring IrO_x particles onto the support catalyst 9R-$BaIrO_3$ (IrO_x/9R-$BaIrO_3$), promoted the formation of amorphous high-valence $Ir^{5+}O_x$ species.[142] HAADF-STEM images in Figure 11D reveal the growth of an amorphous layer with increasing cycles of CV. Simultaneously, the 9R-$BaIrO_3$ layer underwent Ba leaching, evolving into under-coordinated disordered IrO_6 octahedrons. Analyses of XPS spectra and XANES spectra indicated that the surface of initial IrO_x/9R-$BaIrO_3$ heterostructure transformed into amorphous $Ir^{4+}O_xH_y/IrO_6$ octahedrons and subsequently into amorphous $Ir^{5+}O_x/IrO_6$ octahedrons. This transformation leads to significantly enhanced acidic OER activity and stability compared to 9R-$BaIrO_3$ and IrO_2. Furthermore, Jiang et al. observed that the CoP-Cu_3P heterostructure facilitated in situ amorphization for the oxidation of Co species to high valent state, which might act as the catalytic center during GOR.[143] As shown in Figure 11E, F, the development of an amorphous surface on CoP-Cu_3P, featuring high-valence Co species (Co^{3+}/Co^{4+}), initiated at 1.05 V. In contrast, only a minimal amount of Co^{3+} emerged on the surface of CoP once the voltage surpassed 1.2 V. Compared to catalysts with pure phases, other catalysts featuring heterostructures, such as Ni_3N/Ni@Ni_3N,[66] and $NiSe_2/MoSe_2$,[144] similarly enhance the activity of the in situ formed amorphous species.

The heterogeneous structure of precatalysts is crucial in generating active amorphous structures, and the spatial composition within the heterogeneous structure further influences the development of amorphous formations. Xi's group investigated the spatial arrangements in heterostructure electrocatalysts,[145] like $CoS_{1.97}$, $CoS_{1.97}$-CeO_2 and CeO_2-$CoS_{1.97}$, affecting the reconstruction process during the water splitting. In the HR-TEM images (**Figure 12**A,B), CeO_2-$CoS_{1.97}$ formed a random amorphous layer of CoOOH on $CoS_{1.97}$ nanoparticles, whereas the $CoS_{1.97}$-CeO_2 sample produced an amorphous layer dispersing $CoS_{1.97}$, CeO_2, and CoOOH nanoparticles. The different electronic distribution near the Fermi level in the 3D contour plot for $CoS_{1.97}$-CeO_2 and CeO_2-$CoS_{1.97}$ might lead to a distinct amorphization process (Figure 12C). As shown in the in situ Raman spectra (Figure 12D–F), the broadened peaks of $CoS_{1.97}$ in heterostructure indicate their decreased domain size and increased lattice disorder. The heterostructure catalyst underwent reconstruction as the applied potential increased, exhibiting different characteristics between the CeO_2-$CoS_{1.97}$ and $CoS_{1.97}$-CeO_2. According to the quasi-*operando* XPS spectra depicted (Figure 12G–I), the oxygen-vacancy-rich CeO_2 substrate on CeO_2-$CoS_{1.97}$ facilitated the formation of amorphous CoOOH by reducing the transition energy barrier. Conversely, the presence of surface CeO_2 on $CoS_{1.97}$-CeO_2 led to the formation of crystalline CoOOH. Therefore, the spatial arrangement of the two phases should be considered during the synthesis of heterogeneous catalyst materials. The spatial distribution between these phases can affect electrocatalysis performance, leading to the formation of unique reconstruction structures.

Aside from heterostructures, the crystallinity of catalysts also affects the structure reconstruction, and amorphous precatalysts are more facile to initiate the in situ amorphization process.[146] The flexible electronic structure and rich defective sites of amorphous catalysts allow for easier redox behavior and rapid ion diffusion, resulting in a deep structural reconstruction during the electrochemical process.[147] For metal non-oxide precatalysts, the amorphous phase structure usually can accelerate the etching of anion ligands (e.g., S, B, P) and promote the formation of stable and active species during electrocatalysis. Chen and coauthors reported that a mechanically milled catalyst ($CuFeS_2$-BM), featuring an amorphous layer on crystallized $CuFeS_2$, induced a complete transformation of initially sulfide species into an amorphous structure through prominent S dissolution under OER conditions.[148] $CuFeS_2$-BM exhibits excellent electrochemical performance due to the in situ deep structure self-reconstruction, while the transformation of the active phase in crystallized manually milled counterpart ($CuFeS_2$-HM) is restricted. The flexible structure and abundant vacancies within the amorphous layer of the precatalyst can reduce the energy required for the phase transformation evolution. To further decrease crystallinity, a short time would suffice to achieve complete structural reconstruction. Additionally, sun et al. applied an amorphous NiFe-borate ((NiFe-B_i) layer onto the NiFe-LDH nanoarray, enhancing the in situ formation of amorphous active species on the NiFe-LDH surface.[149] After OER electrolysis, a thicker amorphous layer was formed for NiFe-LDH@NiFe-B_i compared to NiFe-LDH. Comparable observations were reported for NiO@Ni-Bi[150] and p-Co_3O_4@Co-Bi.[151]

Regulating the composition of precatalysts serves as a fundamental approach to controlling the amorphization process. The regulation of anions and cations could influence the stability and the electronic structure of the catalyst, controlling the degree of amorphousness and the formation of different amorphous

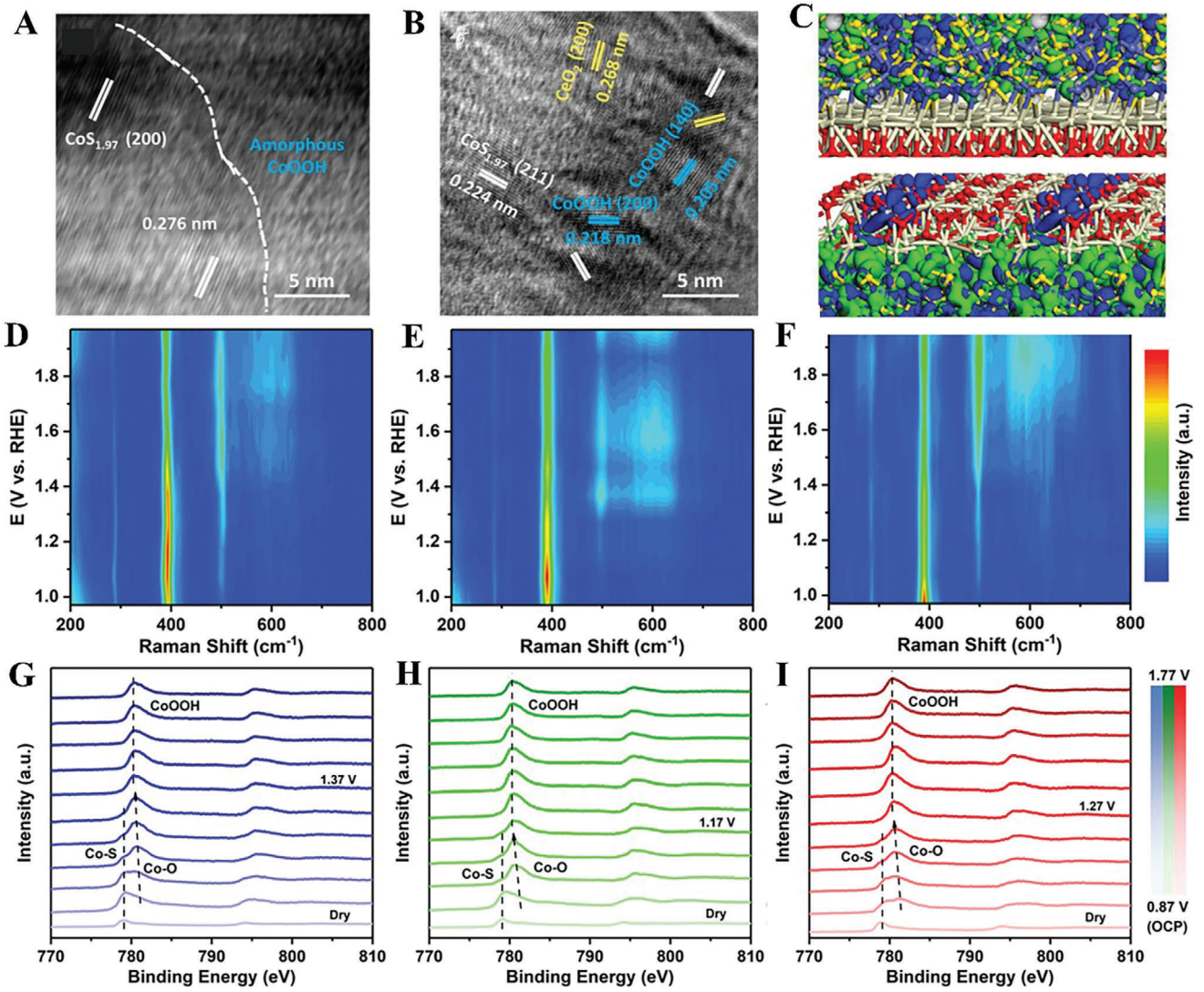

Figure 12. HR-TEM images of A) CeO_2-$CoS_{1.97}$ and B) $CoS_{1.97}$-CeO_2 following 24 h of chronopotentiometry OER tests at the current density of 10 mA cm^{-1}. In situ Raman spectra of D) $CoS_{1.97}$, E) CeO_2-$CoS_{1.97}$, F) $CoS_{1.97}$-CeO_2 at different applied potential (*vs* RHE). Potential (*vs* RHE) -dependent Quasi-*operando* Co 2p XPS spectra for G) $CoS_{1.97}$, H) CeO_2-$CoS_{1.97}$, I) $CoS_{1.97}$-CeO_2.[145] Copyright 2021, Wiley.

active species. Meanwhile, the composition of distinct phases and interfacial electronic structure of heterostructure catalyst influence the development of the amorphous structure. However, most research focuses on in situ amorphization with changes in composition, overlooking the role of the precatalysts' intrinsic chemical properties in amorphization. The relationship between precatalysts' phase structures and amorphization kinetics requires further exploration.

4.1.4. Morphology Regulation

In addition to deliberate design of composition and phase structure, another effective strategy for modifying the evolution of amorphous structures during electrochemical activation involves regulating morphology, including size, porosity, and distribution density.

Nanoparticle size can optimize the electronic structure, accelerating the evolution of active amorphous phases and simultaneously enhancing electrocatalytic activity. Xie et al. documented that La_2NiMnO_6 particles, ranging in size from ≈30 nm to bulk (identified as LNMO-1, LNMO-2, and LNMO-3), manifested distinct electrocatalytic activity and surface reconstruction characteristics.[152] The active amorphous oxide/hydroxide phase on LNMO-1 nanoparticles progressively reached a thickness of 5–8 nm after CV tests, whereas the amorphous layers on LNMO-2 and LNMO-3 surface were thinner than the layer observed on LNMO-1 (**Figure 13**A). Reducing the bulk particle size of La_2NiMnO_6 catalysts to ≈33 nm revealed a decrease in the manganese oxidation state and an increase in the nickel oxidation state, as indicated by XPS and XANES analyses. The formation of an active amorphous phase was facilitated by the emergence of Mn^{3+} and Ni^{3+}. Figure 13B indicated that the spin states of Mn^{3+} exhibited high-spin configurations, while those of Ni^{3+} showed

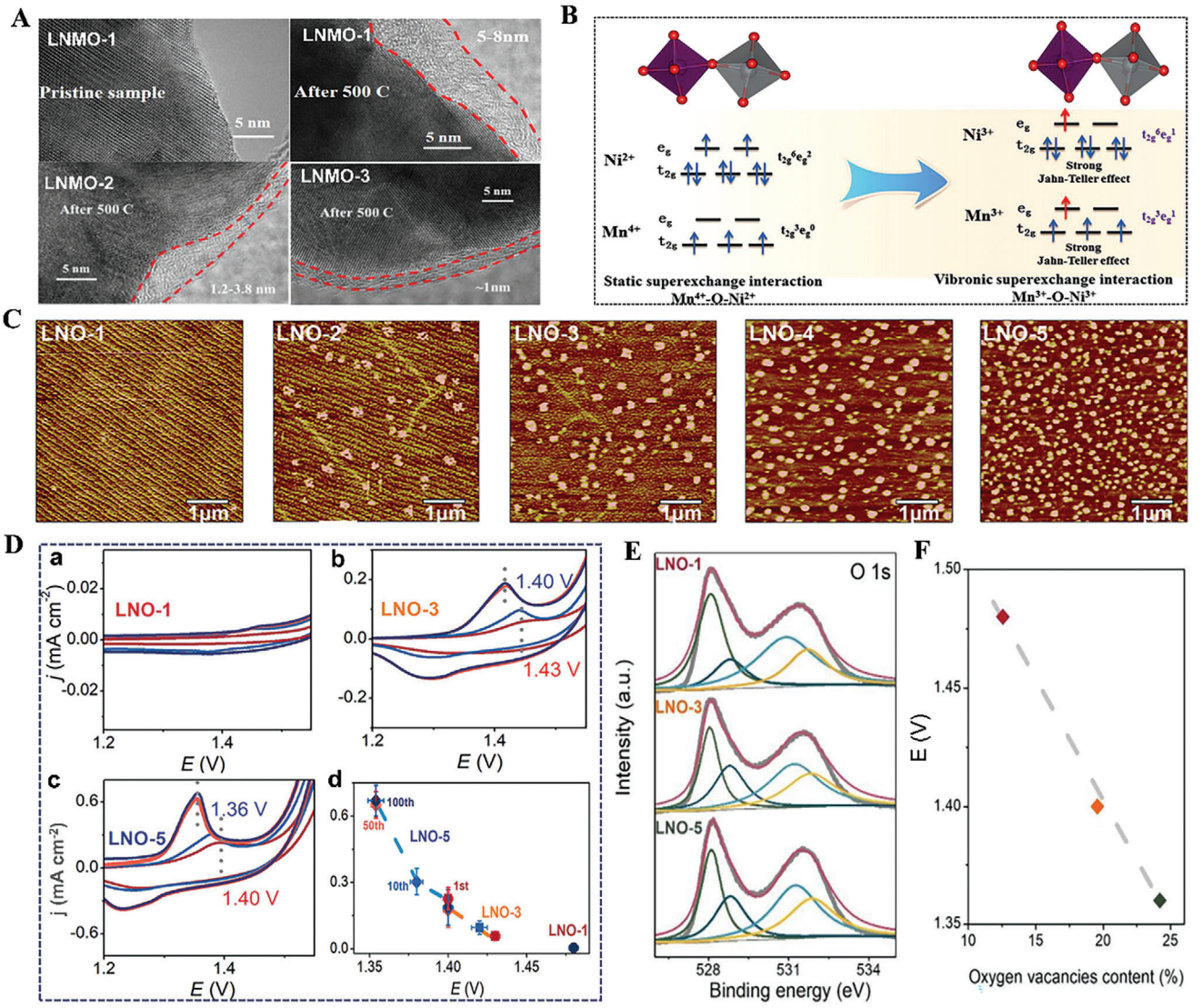

Figure 13. A) HR-TEM images of pristine LNMO-1 and amorphized LNMO-x after 500 cycles. B) Schematic for the deformation of MnO_6 and NiO_6 octahedra.[152] Copyright 2018, American Chemical Society. C) AFM images of LNO nanoparticles dispersed across thin LNO films of varying densities. D) CV scans before the onset of OER at different cycles for LNO-1 a), LNO-3 b), and LNO-5 c); Changes in the reconstructed potential before and after different electrochemical cycles d). E) XPS spectra of O 1s for LNO-x. F) The changes in reconstructed potentials with respect to the oxygen vacancy content of nanoparticle densities.[153] Copyright 2023, Wiley.

low-spin configurations, inducing strong Jahn-Teller distortion of MnO_6 and NiO_6 octahedra. This distortion facilitates the generation of an active amorphous structure.

Furthermore, the distribution density of nanoparticles influences their amorphization process. Lv et al. demonstrated that increasing the density of $LaNiO_3$ (LNO) particles could reduce the potential for the in situ generation of amorphous NiOOH.[153] As shown in Figure 13C, the nanoparticle densities of LNO-x could be observed in atomic force microscopy (AFM) images. Electrochemical measurement (Figure 13D) indicated that both LNO-3 and LNO-5 exhibited signs of the reconstruction reaction. Meanwhile, increasing nanoparticle densities were found to correspond with a decrease in the reconstruction potential. O 1s spectrum of LNO-x indicated that the rise of particle density increases the oxygen vacancies (Figure 13E). Oxygen vacancies exhibited a linear correlation with the reconstruction potential (Figure 13F), resulting in enhanced amorphization at high particle density. The pore structure of the mesoporous catalyst dictates the activity of the in situ generated amorphous phase. Kaya et al. reported that mesoporous NiS_2 with a crystalline phase experienced rapid amorphization to generate a Ni-enriched sulfide film during HER.[154] The mesoporous structure with narrow pores inhibited the facile leaching of sulfurous species. Conversely, the nonporous NiS_2 counterpart shows a complete absence of S_2^{2-} species, resulting in lower HER activity in the generated $Ni(OH)_2$.

Compared to the composition regulation strategy, the impact of morphology on catalytic reconstruction has received less

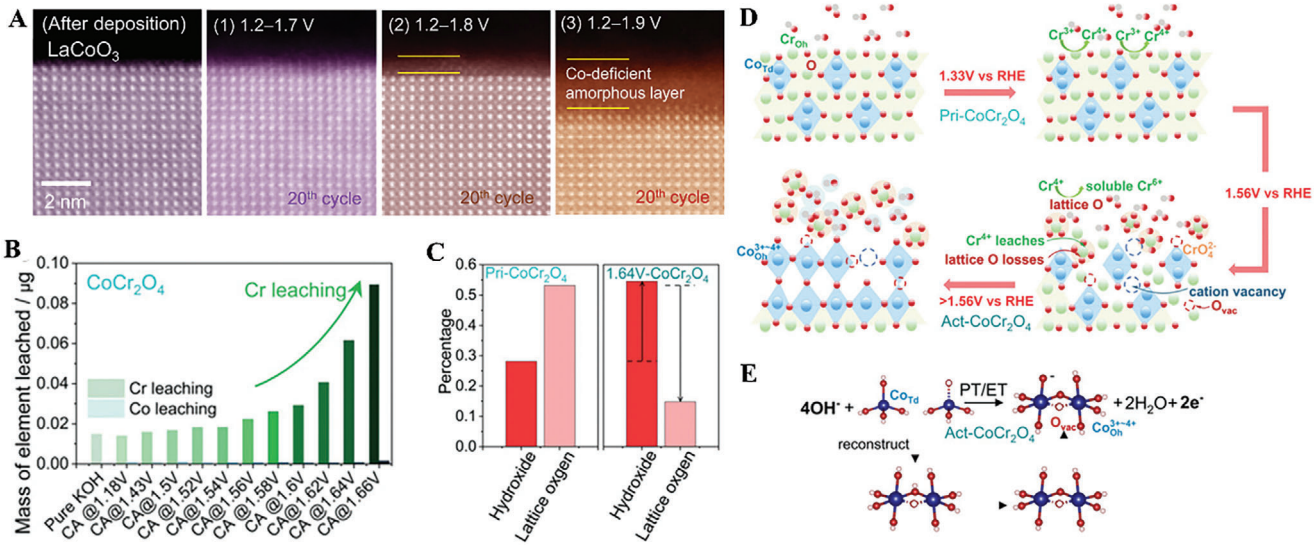

Figure 14. A) STEM images of $LaCoO_3$ under cycling experiments at different potential ranges.[20] Copyright 2021, Nature Portfolio. B) Cr leaching of $CoCr_2O_4$ after consecutive electrochemical activation at a 20 min interval. C) Oxygen contained in different chemical states for $CoCr_2O_4$ before and after reconstruction at 1.64 V. D) Schematic representation of the surface evolution for $CoCr_2O_4$ with the Cr leaching. E) Non-concerted transfer of protons and electrons on the amorphous surface of $CoCr_2O_4$.[32] Copyright 2021, Wiley.

attention. However, the regulation of morphology in nanoparticle or nanoporous catalysts holds promise for promoting the in situ development of an amorphous species and enhancing their activity in electrochemical activation.

4.2. Electrochemical Conditions Alteration

According to Pourbaix diagrams, the equilibrium state of electrocatalysts varies with specific electrode potential and solution pH at a given temperature and electrolyte concentration.[155] Electrochemical conditions, such as applied potential, electrolyte, and temperature, exert significant influence on the structure evolution of electrocatalysts toward thermodynamic equilibrium during the electrocatalytic process. For example, elevated temperatures enhance mass transfer kinetics and electrolyte infiltration, thereby accelerating the reconstruction process and resulting in diverse outcomes. Mai et al. reported the complete reconstruction of $NiMoO_4$ during the electro-oxidation at a high temperature,[156] whereas only surface reconstruction occurred at room temperature. Notably, the transformation into an amorphous structure has not been reported. On the other hand, pH and electrolyte composition profoundly affect both the amorphization process and the properties of amorphous species. Therefore, this section will explore the development of the amorphous structure by modulating electrochemical conditions.

4.2.1. Electrochemical Operational Parameter Manipulation

The surface evolution could be influenced by the electrochemical operational conditions, such as applied potential states and electrochemical activation methods. The degree of amorphization shows a significant dependency on the potential range. When a higher overpotential of up to 1.9 V was applied, an evident Co-deficient amorphous layer became observable on the $LaCoO_3$ thin films (**Figure 14A**).[20] Unfortunately, the amorphous layer formed through dissolution-precipitation at high potential appears to diminish the electrochemical activity of the catalyst. Additionally, Xu et al. explored that the anodic potential regulated the Cr leaching from $CoCr_2O_4$ to promote the in situ generation of the amorphous active Co oxyhydroxide layer during the electrochemical activation process.[32] The initiation and acceleration of Cr leaching coincide with the OER potential. The redox reactions of Cr did not induce reconstruction at low potentials. Application of potentials exceeding 1.56 V versus RHE to $CoCr_2O_4$ facilitated chromium leaching, as Cr^{4+} endured anodic oxidation to soluble Cr^{6+} (Figure 14B). Moreover, lattice oxygen oxidation was observed after the Cr leaching in the form of chromate, leading to a reduction in the proportion of lattice oxygen at high potential (Figure 14C). Therefore, the escalating dissolution of Cr triggers the leaching of lattice oxygen anions, creating both cation vacancies and oxygen vacancies (Figure 14D). This facilitates the formation of an amorphous Co oxyhydroxide layer, which exhibits high intrinsic activity. Figure 14E demonstrates a non-concerted proton-electron transfer of hydroxyl species with oxygen vacancies on the surface.

The lattice oxygen redox typically triggers in situ amorphization of electrocatalysts at high applied potentials. The applied potential on $SrIrO_3$ must reach the OER windows in order to generate an amorphous layer.[19] When the applied potential was below the threshold required for the OER, the $SrIrO_3$ film did not generate an amorphous layer during electrochemical activation. This amorphization is initiated through lattice oxygen oxidation, triggering by coupled diffusion of Sr^{2+} and O^{2-} at the oxide-electrolyte interface under the high applied potential. During in situ reconstruction of $Ni_3N/Ni@Ni_3N$, the presence of amorphous species is also notable and increases with the

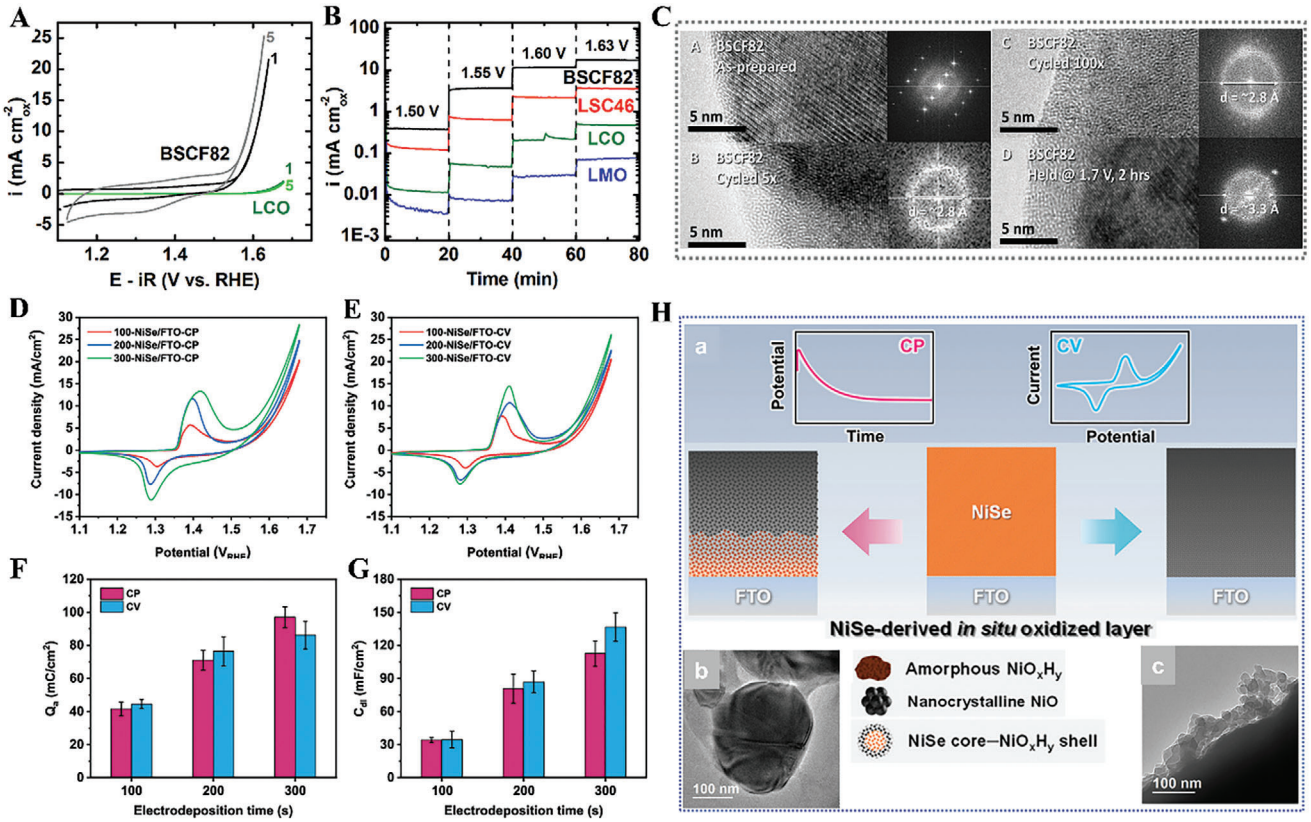

Figure 15. A) CV scan of different catalysts at 10 mV s^{-1}, B) *I–t* curves of different catalysts at various applied potentials. $LaCoO_3$ note as LCO, $La_{0.4}Sr_{0.6}CoO_{3-\delta}$ note as LSC46, $LaMnO_3$ note as LMO. C) HR-TEM image and corresponding FFT for BSCF82 surface undergoing different electrochemical activation processes. Electrochemical conditions: applied potential form 1.1–1.7 V versus RHE; 0.1 M KOH electrolyte, scan rate at 10 mV s^{-1}.[157] Copyright 2012, American Chemical Society. CV analysis of reconstructed x-NiSe/FTO after D) CP activation and E) CV activation. (x represents NiSe electrodeposition times on FTO of 100, 200, or 300 s) The alterations in Q_a and C_{dl} for different catalysts following CP F) and CV G) treatment. H) Schematic illustration of the surface evolution of NiSe after CV and CP activation a). TEM images of 300-NiSe/FTO after CP activation b) and CV activation c).[158] Copyright 2022, American Chemical Society.

expansion of the potential region.[66] The features of amorphous NiOOH seemed to disappear when the potential returned from a high level to a low state. Meanwhile, Xia et al. suggested that more negative potential will slow down the amorphization process of transition-metal phosphides to form a thin shell of amorphous species.[100]

Electrochemical activation at appropriate voltage levels play a critical role in initiating the formation of amorphous structures, while electrochemical activation conditioning also significantly influences their evolution. Yang et al. discovered that the electrochemical activity of perovskite catalyst (BSCF82) increased in both CV and potentiostatic measurements (**Figure 15**A,B),[157] revealing the reconstruction of BSCF82. Particularly, BSCF82 exhibited a marked amorphization rate when subjected to CV experiments, as opposed to the potentiostatic testing at a constant value (Figure 15C). Mullins et al. investigated the impact of CV and chronopotentiometry (CP) on the in situ amorphization level of NiSe deposited on fluorine-doped tin oxide glass (FTO) substrate.[158] The electrochemical characterization of the reconstructed catalyst unveiled discrepancies in the extent of amorphization and the composition of amorphous species (Figure 15D,E). Comparing the anodic redox charge associated with the Ni^{2+} to Ni^{3+} transition (Q_a) and double-layer capacitance (C_{dl}) values suggested that CV was associated with a higher level of in situ oxidation for thicker NiSe samples (300-NiSe-FTO) relative to CP (Figure 15F,G). As illustrated in Figure 15H, CV conditioning resulted in a completely in situ amorphization of 300-NiSe/FTO, thereby generating randomly shattered aggregates of amorphous NiO_xH_y. Conversely, 300-NiSe-FTO underwent partial oxidation when subjected to CP electrochemical conditioning. As a result, core-shell particles, amorphous NiO_xH_y, and nanocrystalline NiO were observed after CP activation.

The electrochemical conditioning method may determine the electrolyte-permeable thicknesses, thereby controlling the oxidation and reduction processes to influence the rearrangement of precatalysts into an amorphous structure. Electrochemical conditioning through CV is likely to facilitate electrolyte permeation to electrocatalysts compared to CP, consequently leading to the complete in situ amorphization. On the other hand, as the reconstruction process of Co_3O_4 proceeded in a phosphate electrolyte, an amorphous cobalt (oxyhydr)oxide-like phase formed during the CP experiment.[56] Conversely, following the CV experiment, a 3 nm-thick amorphous layer became embedded on the catalyst's surface, which is barely discernible through structural

studies. CP under OER conditions suggests a greater charge transfer per unit of experimental time compared to CV. Therefore, different activation methods exert varying effects on catalysts, ultimately affecting the development of amorphous phases. Moreover, Mullins's study displayed that the amorphous cobalt oxide particles derived from Co_3C progressively thicken with an increasing number of sweeps.[38] Eventually, complete conversion of Co_3C to an amorphous state occurs, contributing to heightened ECSA and minimized OER overpotential.

Electrochemical activation methods not only induce varying degrees of amorphization but also influence the nature of the amorphous species formed in situ. Jaramillo et al. explored the in situ surface alterations of the MoN catalyst under ORR conditions using a controlled potential hold procedure.[159] Amorphization and oxygen incorporation of the MoN surface could be observed under moderated polarization. As the potential exceeded 0.7 V, oxygen incorporation continued, substantial Mo dissolution occurred, and the degree of amorphization increased. This indicates that the amorphized surface species changed at high applied potentials. Electrochemical activation through CV and linear sweep voltammetry (LSV) may result in the formation of distinct amorphous species, respectively. Li's group illustrated that a reversible Co oxidation occurred on the amorphous $Co(OH)_2$-ZIF-L surface during CV activation.[36] Upon activation by LSV, the surface of the catalyst experienced irreversible oxidation reactions. The amorphization induced by CV cycles led to the generation of Co^{II}/Co^{III} and Co^{III}/Co^{IV} redox species. Hod's team investigated the electrochemical conversion of cobalt-imidazole-based MOF during the CV scan within the negative potential window (−1.76 to −0.15 V) to produce amorphous species for the HER.[37] Irrespective of the scan rate, all samples exhibited their amorphous nature after electrochemical activation. Nevertheless, XPS and Raman spectroscopy analyses indicated that altering the potential scan rate resulted in the formation of distinct cobalt compounds. This variation is attributed to differences in dwelling time, which consequently affected the contact time with OH^-. Additionally, the scan rate had a significant impact on the levels of sulfur and metallic cobalt. Therefore, effective control of electrochemical conditions is essential for crafting an efficient amorphous structure, which in turn boosts electrochemical reactions.

4.2.2. Electrolyte Adjusting

The activity and stability of the catalyst during electrocatalysis are directly influenced by the pH value of the electrolyte, affecting the structural transformation and new phase formation.[160] Ersen et al. demonstrated that pH influenced the in situ reconstruction of Co_3O_4.[56] The reconstructed species on the in situ generated amorphous layer differed between alkaline and neutral electrolytes (**Figure 16A**). Furthermore, the catalyst exhibited more favorable kinetics for the OER in the alkaline electrolyte. Significant morphological and structural changes might be induced by the rapid electrochemical reaction. The corrosion behavior of the electrocatalyst could be modified by the pH conditions during the electrochemical process, resulting in the desired reconstruction. Hofmann et al. reported that Co_2P degraded in both acidic and alkaline environments.[161] Under alkaline HER conditions, Co_2P experienced in situ reconstruction to form $Co(OH)_2$, whereas its original chemical state remained unchanged in acidic HER conditions. Ir-based crystal oxides can undergo leaching to form amorphous species in acidic conditions, rather than in alkaline conditions.[93] These behaviors are related to the thermodynamic steady state of the metal catalyst according to the Pourbaix diagram. In addition, Grimaud's group unraveled the precise influence of pH on the amorphization of $La_2Li_{0.5}Ni_{0.5}O_{4\pm\delta}$ (LLNO).[31] HAADF-STEM revealed that the amorphous layer on the surface of LLNO thickened as the pH increased from 12.5 to 14. (Figure 16B). The electrochemical quartz crystal microbalance (EQCM) showed that an increase in pH led to a greater mass loss of LLNO. The redox process, coupled with the severe degradation of the LLNO catalyst, may result in the emergence of an amorphous layer in alkaline conditions. The fast redox reaction between OH^-/H^+ ions and the catalyst at high acidity or high alkalinity might trigger significant degradation of catalyst. Other electrocatalysts exhibited similar phenomena, such as Co_2P,[162] $LiCoPO_4$,[27] and Co_9S_8-SWCNT.[163] The regulation of amorphization by the pH of the electrolyte should be considered under appropriate conditions.

Counterions in the electrolytes can contribute a lot to amorphization during in situ electrochemical activation. In the progression of CO_2 reduction reaction (CO_2RR), the presence of I^- anions in the electrolyte, instead of HCO_3^-, could induce in situ amorphization of CuO catalysts. However, increasing the concentration of KI from 0.5 to 1.0 M caused an increase in the crystallinity of the catalyst.[164] Electrolyte anions not only regulate the occurrence of amorphization but also control the amorphous structure. Risch et al. demonstrated that Erythrite (Ery, $Co_3(AsO_4)_2{\cdot}8H_2O$) experienced different levels of amorphization during electrocatalysis in various electrolytes at pH 7.[63] Ery could transform into amorphous layered cobalt oxide after voltage cycling under OER conditions. The development of the reconstructed species was also influenced. The shift of the X-ray edge position in the XANES spectrum indicated the extent of the Co oxidation state related to the electrolyte conditions (Figure 16C). The FT of EXAFS at the Co-K edge revealed that electrolyte anions affected the atom distance within the reconstructed catalyst (Figure 16D). In borate electrolytes, the reconstruction behavior of Ery was more pronounced in comparison to carbonate and phosphate electrolytes. The surprisingly different behavior of the reconstructed Ery in these three electrolytes is expected to control the electrochemical performance. Additionally, ions present in the electrolyte could engage in the amorphization process. Sun reported that an amorphous thin Co-Fe-Bi layer was generated in situ during the reconstruction of $CoFe_2O_4$ in 0.1 M potassium borate (K-Bi) electrolyte, resulting in an outstanding OER activity.[165] As discussed above, the electrolyte conditions affect the amorphization process and the form of the amorphous species. Nevertheless, further research is required to explore the origin of anion effects in the electrolyte and to improve the management of amorphization processes.

In summary, higher applied potentials and harsh electrolytes accelerate the dissolution of most electrocatalysts, leading to amorphization during electrochemical activation. Additionally, the operating conditions affect the redox behavior of catalysts and their interaction with the electrolyte, influencing the formation of amorphous structures and the activity of amorphous species. Furthermore, the anions in the electrolytes play a

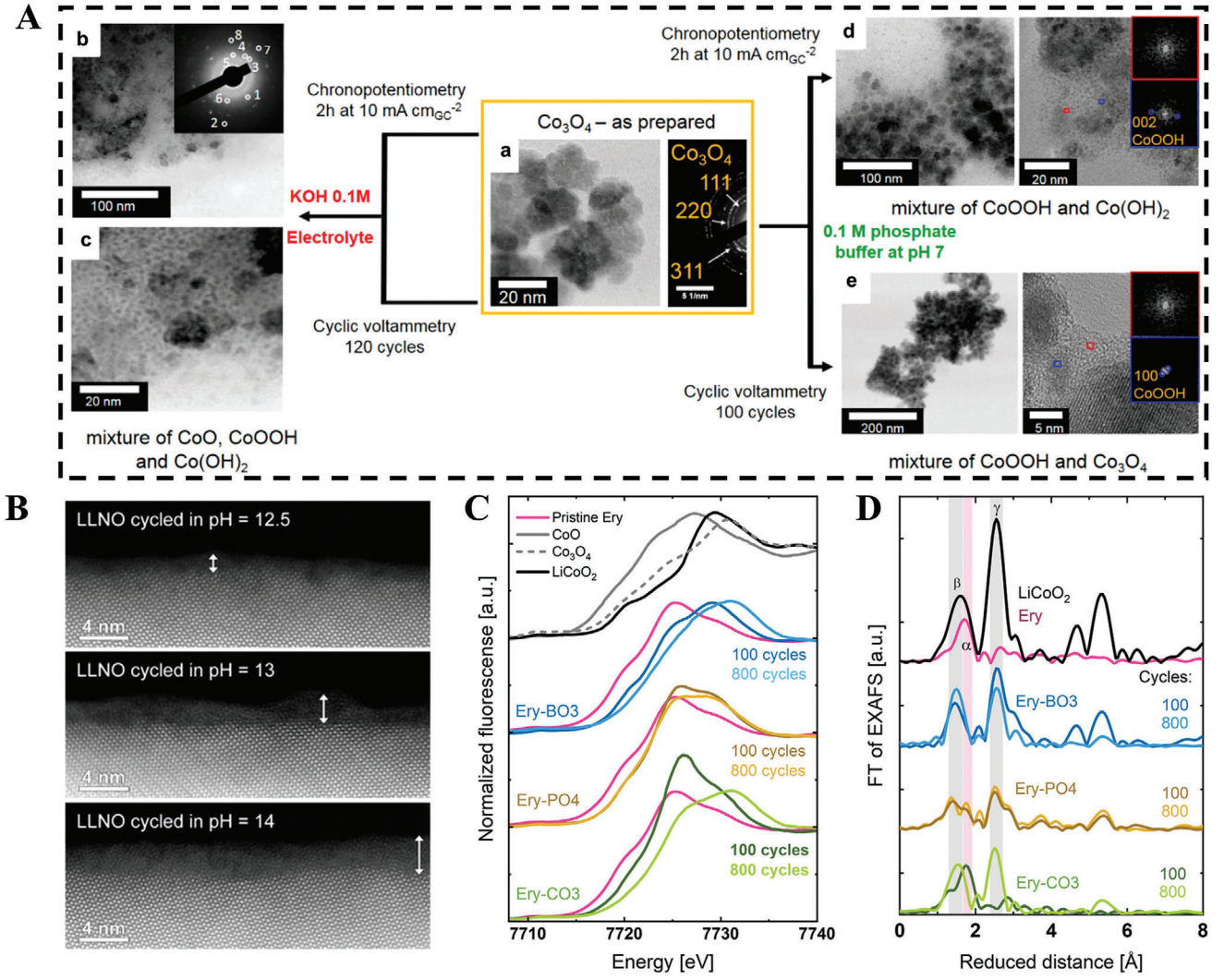

Figure 16. A) Bright-field STEM images and diffraction patterns of Co_3O_4 pre- and post-electrochemical activation. Pristine Co_3O_4 a). Post-Co_3O_4 after CP test in alkaline solution b). Post-Co_3O_4 after CV test in alkaline solution c). Post-Co_3O_4 after CP test in neutral solution d). Post-Co_3O_4 after CV test in neutral solution e). Inset: diffraction pattern displaying a mixture of Co oxide. In the inset of figure b, 1, 2, and 3 represent CoOOH, 4 and 5 represent $Co(OH)_2$, and 6, 7, and 8 represent CoO. Experiment conditions: 0.1 M KOH electrolyte, neutral potassium phosphate aqueous electrolyte, current density of 10 mA cm^{-2} in CP, 0.6-1.8 V versus RHE applied potential in CV.[56] Copyright 2019, American Chemical Society. B) HAADF-STEM images for LLNO following electrochemical cycling in alkaline solutions with varying pH.[31] Copyright 2018, American Chemical Society. C) Co-K edge in XANES spectra for the pristine Ery and post Ery collected after electrochemical activation in neutral borate, phosphate, and carbonate electrolyte. Comparing with the Co-K edge spectra of $LiCo^{(3+)}O_2$, $Co_3{}^{(2.7+)}O_4$, and $Co^{(2+)}O$. D) Fourier transform of the Co-K edge EXAFS on pristine Ery and post Ery with electrochemical activation in neutral electrolyte with different counterions. The light-colored gray areas and light-colored pink areas present the interatomic distances of layered Co-oxides (peaks β and γ) and typical Co-O in Ery.[63] Copyright 2021, Wiley.

decisive role in the evolution of amorphous structure, although the exact mechanism behind this influence remains unclear. There are various methods available to regulate the amorphization process, while it is challenging to predict in situ amorphization behavior of electrocatalysts during electrochemical activation. Establishing a universal descriptor system is necessary to elucidate the relationship between the amorphization process and precatalysts' physicochemical properties. Additionally, delving into the reasons behind the impact of electrochemical conditions on the in situ amorphization of catalysts would foster the advancement of high-performance electrochemical systems.

5. Roles of In Situ Generated Amorphous Phases in Electrocatalysis

In situ amorphization of electrocatalysts has been well-documented in various electrochemical reactions. As such, it is important to analyze the role of the self-evolved amorphous species in the electrocatalytic process. In this section, the main role of the in situ generated amorphous species in electrochemical oxidation and reduction processes is comprehensively discussed. In particular, the amorphous species-regulated active sites and stability are disclosed.

5.1. Electrochemical Oxidation Reactions

Electrochemical oxidation reactions like OER, UOR, BOR, hydrogen oxidation reactions (HOR), ethylene glycol oxidation reaction (EGOR), and methanol oxidation reaction (MOR) are critical processes in electrochemical energy applications. Under oxidation potentials, the applied catalysts may undergo self-reconstruction and form amorphous phases. **Table 1** lists representative amorphization processes of electrocatalysts during various electrochemical oxidation reactions. Most amorphization of transition metal-based catalysts results in the generation of metal (oxy)hydroxide phases. In this section, the role of self-evolved amorphous phases in electrochemical oxidation reactions is discussed.

5.1.1. High-Valence Components in Amorphous Species

Accompanied by amorphization, the electrochemical activity of the catalyst is commonly associated with the presence of high-valence elements in the in situ formed amorphous phase. John et al. demonstrated that the retention of high valence Ni^{3+} ions in amorphous NiOOH species can sustain urea oxidation rate during the prolonged electrocatalysis of UOR.[166] On the contrary, the presence of Ni^{2+} in NiO can lead to a drop in UOR activity. The high valence state of Ni^{3+} associated with amorphous species is also considered as the active species in other electrochemical oxidation reactions, such as OER[167] and GOR.[80] Ni^{3+} is generally considered advantageous for electrochemical activation due to its high electrophilicity toward adsorbed oxygen.[186]

During electrocatalysis, the amorphization of precatalysts could bring about the emergence of species with heightened oxidation states. Zhang et al. reported that the electrochemically activated NiFe PBA showed an activity level roughly six times greater than the noble metal catalyst IrO_2 (10 mA cm^{-2}).[35b] The TEM-SAED and XANES analyses identified the formation of amorphous $Ni(OH)_2$ following the electrochemical activation of NiFe-PBA. *Operando* XAS techniques revealed that Ni^{2+} in amorphous $Ni(OH)_2$ was reversibly oxidized to Ni^{4+} under varying applied potential. In contrast, the change in Ni valence state was smaller in crystalline $Ni(OH)_2$ upon the application of potential. They speculated that the deprotonation process of amorphous $Ni(OH)_2$ triggers the transformation of the valence state as the applied potential increases (**Figure 17A**), and Ni^{4+} ions serve as active centers facilitating the oxygen evolution process. Projected density of states (PDOS) calculated by DFT revealed that deprotonation of amorphous $Ni(OH)_2$ led to the formation of highly reactive Ni^{4+} ions and oxygen 2p holes (Figure 17B). The deep insertion of Ni^{4+} 3d band into the O 2p band caused an upward shift in the O 2p band and an increase in the concentration of O 2p holes. These O ions with 2p holes can act as electrophilic centers during OER, which significantly contributes to the catalytic activity.

High-valence species produced during in situ amorphization of other catalysts (such as $LaCo_{0.8}Fe_{0.2}O_{3-\delta}$,[87] CoMn LDH,[168] $Ni_3Fe_{0.75}V_{0.25}/Ni_3Fe_{0.75}V_{0.25}N$ heterojunction,[187] and CoP-Cu_3P[143]) are also proposed to play a role in catalyzing the reactions of water and organic molecules. Li's research showed an increase in Co^{4+} content with the amorphization of $Li_2Co_2O_4$.[51] They calculated the electronic structure of simulated surface amorphous species, which closely aligned with the requirements of the anionic redox reaction in OER, featuring a highly covalent Co-O bond and significant O 2p states near the Fermi level. This indicated that the Co^{4+}-O atomic motif may function as active sites during the OER. Otherwise, Risch et al. discovered that erythrite (Ery) exhibited disparate in situ amorphization processes in four neutral electrolytes, causing variations in the oxidation states of cobalt.[63] According to Figure 17C, in situ generated amorphous layer on Ery displayed the highest Co oxidation state after reconstruction in the carbonate electrolyte, leading to the highest current density. A similar amorphization can be observed when Mn_3N_2 and Mn_2O_3 act as electrocatalysts in OER.[39] The amorphization of Mn_3N_2 was accompanied by a drastic increase in the oxidation state of Mn compared to Mn_2O_3. The transition from Mn^{2+}/Mn^{3+} to Mn^{3+}/Mn^{4+} occurred on the amorphous surface of Mn_3N_2 (Figure 17D). The presence of Mn^{3+}/Mn^{4+} composition enables the formation of Jahn-Teller distorted Mn-O bonds, thereby enhancing the electrocatalytic activity. The required overpotential for Mn_3N_2 during electrocatalysis was 390 mV, significantly lower than that for Mn_2O_3 (470 mV). It can be concluded that the in situ accumulation of high-valence active sites on amorphous structures can lead to increased activity for electrochemical activation.

5.1.2. Coordination Environment in Amorphous Species

The electronic structure of amorphous species could be influenced due to the incorporation of multiple elements, thereby boosting the activity of electrocatalysts. Particularly, the presence of oxyanion-coordinated amorphous species during in situ electrochemical reconstruction is a typical feature in the amorphization process of electrocatalysts containing anions. Zhang et al. reported that an amorphous oxysulfide layer was observed on the $NiCo_2S_4$ surface during OER operating conditions.[107] This enhancement is attributed to the cooperative action facilitated by oxygen and sulfur anions.

The oxyanion-coordinated environment on the amorphous layer might enhance the OER performance by altering the activity of active sites. Wang et al. investigated the amorphization behavior of Ni metalloids (NiT_x, where T represents P, S, and Se) during electrochemical activation, which in situ formed oxyanion-coordinated amorphous NiOOH (**Figure 18A**).[169] The MOR activity of NiOOH-PO_x derived from NiP_x surpassed that of other samples (Figure 18B). NiP_x-R required a potential of 1.4 V to achieve a current density of 400 mA cm^{-2} in the MOR, which was 90 and 117 mV lower than NiS_x-R and $NiSe_x$-R, respectively. The coordination of different oxyanions on amorphous NiOOH affects the adsorption of methanol molecules, as measured by temperature-programmed desorption. Density functional theory (DFT) calculations were conducted to clarify the intrinsic differences caused by the oxyanion-coordinated NiOOH. Figure 18C shows that oxyanions effectively tailored the Ni 3d band center (ϵd), with values of −1.63, −1.68, and −2.01 eV for NiOOH-SO_x, NiOOH-PO_x, and NiOOH-SeO_x, respectively. NiOOH-PO_x presented the most significant Ni 3d-O 2p orbital hybridization and increased Ni-O covalency, improving its adsorption of reactant molecules. In addition, the charge density difference calculation illustrated the fluent electron transfer from the oxygen atoms of

Table 1. The list of self-evolved amorphous phases under electrochemical oxidation reaction.

Precatalyst	Reaction	Electrochemical conditions	Amorphous species	Role of amorphous species	Ref.
$NdNiO_3$	UOR	CV: 0 – 0.7 V vs Hg/HgO at 100 mV s^{-1}, 1 M KOH solution	NiOOH	Stabilized Ni^{3+} ions in amorphous NiOOH steer the UOR reaction	[166]
NiO_x	OER	Chronopotentiometric measurement (CP): a constant current density of 10 mA cm^{-2} for 50 000 s, 1.0 M KOH solution	An amorphous layer containing a high concentration of Ni^{3+}	Ni^{3+}/Ni^{2+} phase exhibits higher electrophilicity to improve catalytic properties	[167]
$Au@NiS_x$	GOR	Chronoamperometric analysis (CA): a constant potential of 1.78 V vs RHE for 1 h, 0.1 M sodium tetraborate solution with 0.1 M glycerol	NiOOH	Ni^{3+} in the NiOOH serves as the active center toward GOR	[80]
NiFe Prussian blue analogue (PBA)	OER	CP: a constant current density of 20 mA cm^{-2} for ≈110 h, 1 M KOH solution	$NiOOH_{2-x}$	Ni^{4+} ions act as an electrophilic center to activate oxidized oxygen ions	[35b]
$LaCo_{0.8}Fe_{0.2}O_{3-\delta}$	OER	LSV: a scan rate of 5 mV s^{-1} from 0 to 0.9 V vs Ag/AgCl, O_2-saturated 0.1 M KOH solution	(Co/Fe)O(OH)	Amorphous (Co/Fe)O(OH) layer induces a modified electronic environment of active sites	[87]
CoMn LDH	OER	CP: a constant current density of 10 mA cm^{-2} for 3 h, 1 M KOH solution	Amorphous regions enriched with Co^{4+}	Co^{4+} species in the amorphous layer enhance the performance of the catalyst	[168]
$CoP\text{-}Cu_3P$	GOR	LSV: a scan rate 2 mV s^{-1} from 0.6 to 1.5 V vs RHE, 1 M KOH solution with 0.1 M glycerol	CoO_x	High-valence Co^{3+} and Co^{4+} species are beneficial for the enhanced GOR activity	[143]
$Li_2Co_2O_4$	OER	CV: −0.1 to 0.7 V vs Hg/HgO at 5 mV s^{-1}, O_2-saturated 1 M KOH solution	Co (oxy)hydroxides	Co^{4+}-O atomic motif serves as an active site during catalysis	[51]
Erythrite $(Co_3(AsO_4)_2{\cdot}8H_2O)$	OER	CV: 0.6 to 2.1 V vs RHE at 100 mV s^{-1}, 0.1 M electrolyte at pH 7	Co (hydr)oxide	Increased cobalt valence promotes the catalytic activity	[63]
Mn_3N_2	OER	CP: a constant current density of 10 mA cm^{-2} for 3 h, 1 M KOH solution	MnO_x	The high valence state of manganese facilitates OER by influencing the strength of chemical bonds	[39]
$NiCo_2S_4$	OER	CP: a constant current density of 10 mA cm^{-2} for 2 h, O_2-saturated 1.0 M KOH solution	Oxysulfide layer	Amorphous oxysulfide serves as an active species and exhibits stable catalytic performance	[107]
NiP_x, NiS_x, and $NiSe_x$	MOR	CV: 0.924 to 1.624 V vs RHE at 100 mV s^{-1} for 300 cycles, 1 M KOH solution	NiOOH-TO_x (T: P, S, Se)	Amorphous NiOOH-PO_x selectively oxidizes methanol into formate due to an optimal coordination environment	[169]
Ni_3S_2	OER	LSV: −0.01 to 0.80 V vs saturated calomel electrode (SCE) at 10.0 mV s^{-1}, 1 M KOH solution	Oxysulfide layer	Oxysulfides with hetero-anionic structures act as the active site for long-term OER	[108]
Boronized NiFe alloy	OER	CP: a constant current density of 10 mA cm^{-2} for 10 h, 1 M KOH solution	Metaborate-containing oxyhydroxide	Metaborate-containing oxyhydroxide enhances both catalytic stability and corrosion resistance	[170]
NiMo-Fe	OER	CP: a constant current density of 100 mA cm^{-2} for 200 h, 1.0 M KOH solution	Ni(Fe)OOH-MoO_4	MoO_4^{2-} ions on the amorphous structure influence the OOH* adsorption on Fe sites	[171]

(*Continued*)

Table 1. (Continued)

Precatalyst	Reaction	Electrochemical conditions	Amorphous species	Role of amorphous species	Ref.
$Ni_{0.42}Co_{0.58}F_2$	OER	CP: a constant current density of 10 mA cm^{-2} for 10 h, 1 M KOH solution	Ni-substituted CoOOH	Amorphous species lower the energy required for the rate-determining step	[172]
CoFe-LDH	Sulfide oxidation	LSV: 0.5 to 2.0 V vs Ag/AgCl with a scan rate of 50 mV s^{-1}, a mixture of 0.5 mM diphenyl sulfide and acetonitrile/H_2O (2.0 mL, 1:1 v/v)	CoFe-oxyhydroxide	CoFe-oxyhydroxide modulates the electronic structure	[173]
Cu/Ni_3S_2	BOR	CV: 100 mV s^{-1} for 10 cycles, 1 M KOH solution	Cu/NiOOH-SO_x	Cu doping and regulation of oxyanions modulate the coordination environment of active Ni sites	[81]
NiS_2	OER	LSV: 1.1 to 1.9 V vs RHE, 1 M KOH solution	NiOOH-SO_4	Chemisorbed sulfate radicals on the amorphous NiOOH enhance OER performance	[105]
NiS_2	UOR	CA: a constant potential of 1.45 V vs RHE for 600 s, 1.0 M KOH solution with 0.33 M urea	Amorphous Ni(oxy)hydroxide co-exist with SO_x	Oxyanions enable the selective adsorption of urea reactants	[174]
CoM-ZIF-L	OER	CV: 0.765 to 1.464 V vs RHE for 40 cycles at 50 mV s^{-1}, 0.1 M KOH solution	$Co(OH)_2$	Amorphous metal oxy(hydroxide) reduces the overpotential at the potential-limiting step	[36]
Uniform FeS_2 microspheres	OER	LSV: 0 to 1 V vs Hg/HgO at 5.0 mV s^{-1}, 1.0 M KOH solution	FeOOH	Amorphous shells with lattice defects optimize intermediate adsorption	[76]
NiCrO	GOR	CV: 0.9–1.6 V vs RHE for 100 cycles, 1 M KOH solution	NiOOH	Vacancies on the amorphous structure enhance intermediate adsorption	[53]
Co and Cl co-doped Ni_3S_2 (Co,Cl-NiS)	EGOR	LSV: 1.0 to 1.7 V vs RHE at 5 mV s^{-1}, 1 M KOH with 0.1 M ethylene glycol	Co-NiOOH	Vacancies on the amorphous layer contribute to the enhanced catalytic performance	[77]
Ni-based perovskite hydroxide $NiSn(OH)_6$	OER	CV:0.5 to 0.8 V vs Hg/HgO for 80 cycles at 10 mV s^{-1}, 1 M KOH solution	NiOOH	Sn vacancies on the amorphous surface optimize the activity of active Ni sites	[175]
F-$Ni(OH)_2$	OER	CV: 1.1 to 1.6 V vs RHE at 50 mV s^{-1}, 1 M KOH solution	F-NiOOH	F-NiOOH/F-$Ni(OH)_2$ p-n junction interface affects the charge-transfer process	[176]
$Ni_2P_4O_{12}$	OER	CA: a constant potential of 0.3 V vs RHE for 24 h, 1 M KOH solution	$Ni(OH)_2$	Heterostructure electrocatalyst accelerates electron transmission and improves electronic conductivity	[177]
$(NiFe)_3Se_4$	OER	CV:0 to 0.8 V vs Hg/HgO for 3000 cycles, 1 M KOH solution	(NiFe)OOH	Heterostructure between amorphous (NiFe)OOH and $(NiFe)_3Se_4$ with high intrinsic activity	[178]
$Ni_3N@Ni_3VN$	OER	LSV: 0.2 – 0.9 V vs Hg/HgO for 20 cycles, 1 M KOH	NiVOOH	Heterostructure interface reduces the energy required at the rate-determining step	[179]
Hybrid $La_{0.33}SrCo_{0.5}Fe_{0.5}O_x$ (H-LSCF)	OER	CP: a fixed current density of 10 mA cm^{-2} for 16 h, 0.1 M KOH solution	RP (A_2BO_4) perovskite phase is collapsed to form an amorphous structure	The combination of amorphous and crystalline phases initiates lattice oxygen oxidation	[180]
Ni_9S_8/Ni_3S_2	OER	CV: 0.425 to 2.425 V vs RHE at 100 mV s^{-1}, 1.0 M KOH solution	NiOOH	Congee-like Ni_3S_2/amorphous NiOOH heterostructure optimizes OER intermediate adsorption	[181]

(*Continued*)

Table 1. (Continued)

Precatalyst	Reaction	Electrochemical conditions	Amorphous species	Role of amorphous species	Ref.
Ni_3N/NF	HOR	CV: 1.20 to 1.60 V vs RHE at 30 mV s^{-1} for five cycles, 1.0 M KOH solution	$Ni(OH)_2$	$Ni(OH)_2/Ni_3N$ heterostructure optimizes the electronic structure of Ni active sites	[182]
Ni_3S_2	BOR	LSV: 1.2 to 1.7 V vs RHE for five scans at 5 mV s^{-1}, 1 M KOH solution with 15 mM HMF	NiO_x	Heterostructure adjusts the reactant adsorption behavior	[23]
Biphasic CoNi/Zn $(Fe,Al,Cr)_2O_4$	OER	CA: a constant potential at 1.74 V vs RHE for 5 h, 1 M KOH solution	Fe-CoNiOOH	Fe-CoNiOOH species terminated the crystal disruption	[183]
$NiFe_{0.5}Sn$	OER	CP: a constant current density of 10 mA cm^{-2} for 2 h, 1 M KOH solution	NiFe(oxy)hydroxide	Amorphous shell of NiFe(oxy)hydroxide protects the metallic core, resisting further oxidation	[184]
RuMn alloy	OER	CV: 1.25 – 1.75 V vs RHE for 10 000 cycles, 0.5 M H_2SO_4 solution	RuO_x	Amorphous RuO_x provides a protective layer for catalyst	[185]
$LiCoO_{1.8}Cl_{0.2}$	OER	CV: 1.2 – 1.6 V vs RHE for 20 cycles, 1 M KOH solution	Co(oxy)hydroxide	Amorphous Co(oxy)hydroxide exhibits outstanding electrochemical activity and remarkable stability	[117]
NiMoN@NiFeN	OER	CV: 1.2 to 1.8 V vs RHE at 2 mV s^{-1} for 100 cycles, 1 M KOH solution	NiFe oxide and NiFe oxy(hydroxide)	Amorphous phase contributes to chlorine corrosion resistance	[42]
NiFeLDH@NiCoS NAs	OER in seawater	LSV: 1.0 to 1.7 V vs RHE, 1 M KOH solution with 0.5 M NaCl	γ-NiOOH and FeOOH (γ-NiFeOOH)	γ-NiFeOOH minimizes Cl^- corrosion through stabilizing OH* intermediate	[34]

OH to Ni species in NiOOH-PO_x (Figure 18D). In contrast, this electron transport was inhibited in NiOOH-SO_x due to the influence of S sites, and the adsorbing ability of OH* in NiOOH-SeO_x was weak, which was unfavorable for the electrooxidation of MOR. The coordination of oxyanions on amorphous species, which adjusts the d band center and facilitates charge transfer, enhances the activity of the electrocatalyst.

A similar oxyanions coordinate structure to accumulate the activity of metal active site are found in other electrocatalysts, such as amorphous oxysulfide layer on the Ni_3S_2,[108] metaborate-containing oxyhydroxide on the boronized NiFe alloy,[170] and Ni(Fe)OOH-MoO_4 on the surface of NiMo-Fe.[171] Furthermore, the electronic structure of active sites within amorphous species can be modulated by the presence of bimetallic elements.[188] This modulation optimizes the adsorption behavior of intermediates.[172,173] Otherwise, in situ formation of amorphous species, characterized by a coordination environment comprising both oxysulfide and copper sites, provides additional active sites and tunes the electronic structures, thus improving the oxidation of HMF.[81]

Chemisorbed sulfate radicals on the amorphous NiOOH structure not only enhance the activity of Ni sites but also participate in the transformation pathway during electrocatalysis. Cheng et al. reported that the NiS_2, $NiSe_2$, and NiTe electrocatalysts converted into amorphous NiOOH, where oxyanions were chemisorbed on the amorphous layer.[105] **Figure 19A,B** illustrate the OER pathway and the free energy diagrams of intermediates on NiOOH-SO_4 via the adsorbate evolution mechanism (AEM) and lattice oxygen-mediated mechanism (LOM). For AEM, the chemisorbed SO_4 modified the d_{yz} orbitals of the Ni atom and strengthened the Ni-O bond, while also directly participating in OER as a proton-transfer station and facilitating the intermediate steps of oxygen evolution. On the other hand, sulfates facilitated LOM by aiding in the desorption of formed oxygen molecules. The amorphous oxyanion species constructed in situ are thermodynamically more favorable than the complexes formed by the adsorption of soluble sulfate ions in the electrolyte, thereby enhancing electrocatalytic performance. Qiao et al. investigated that in situ formed amorphous Ni (oxy)hydroxide coordinated with sulfur species (Ni-SO_x) inhibited the oxygen evolution reaction during urea oxidation.[174] As displayed in Figure 19C, urea molecules primarily adhered to the Ni-SO_x surface. Selective oxidation of urea occurred on the surface of Ni-SO_x through its reaction with OH^- ions from the alkaline electrolyte, resulting in C-N bond cleavage. On the contrary, the OER occurred on the surface of NiO_x owing to the competitive adsorption of OH* on the active sites. In situ attenuated total reflectance infrared (ATR-IR) spectra (Figure 19D) demonstrated that urea molecules covered the surface of amorphous Ni-SO_x because the oxyanion inhibits OH^-, whereas the surface of NiO_x exhibited a high concentration of OH^-. Therefore, the incorporation of oxyanion on the amorphous surface achieved high efficiency in urea electrochemical oxidation.

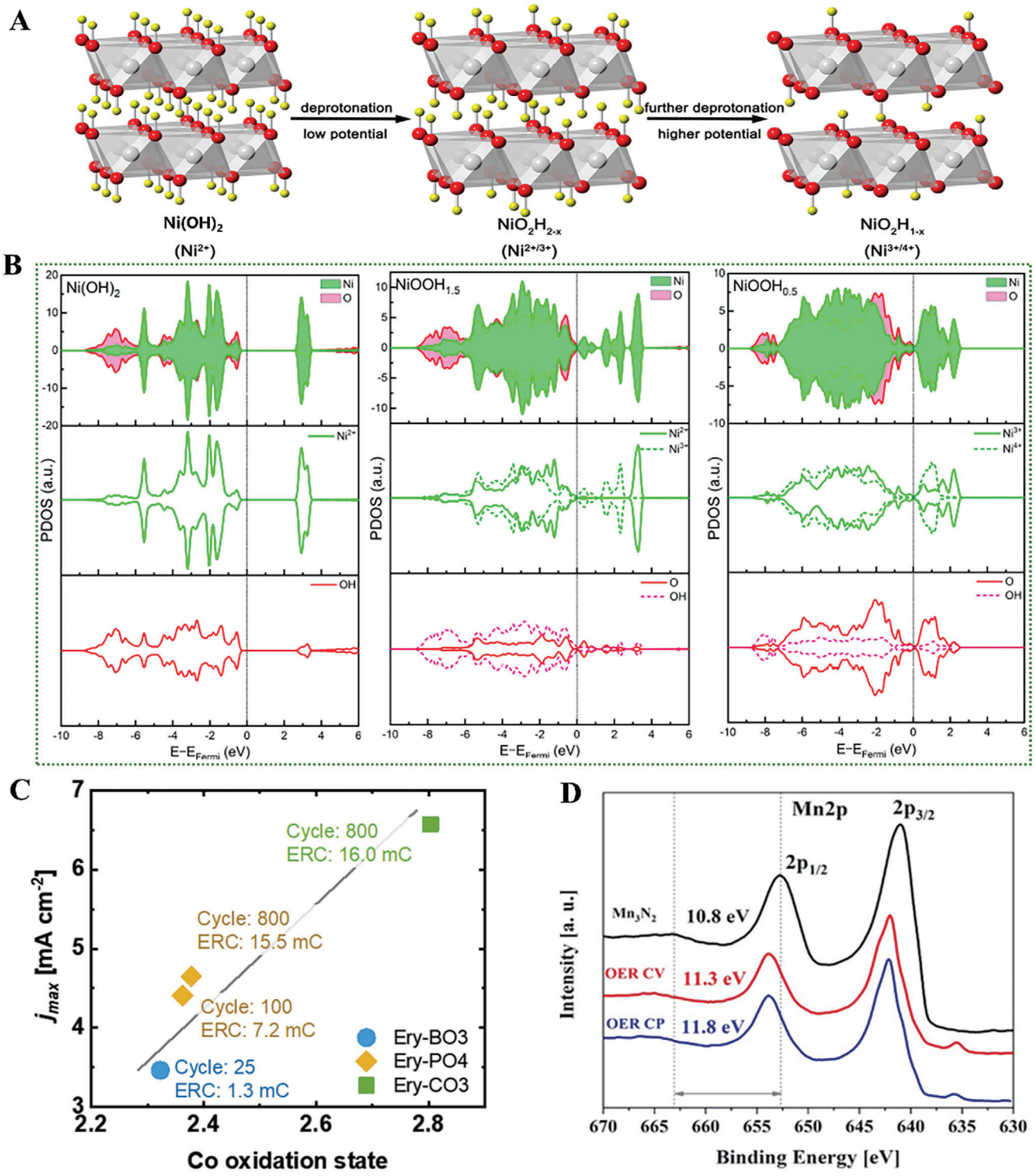

Figure 17. A) Schematic diagram illustrating the structural evolution of amorphized Ni-BPA during OER. B) PDOS for amorphous $Ni(OH)_2$ under varying degrees of deprotonation. The Fermi level was set as the reference point at zero energy.[35b] Copyright 2018, American Chemical Society. C) The relationship between the activity indicator j_{max} (at 2.1 V *vs* RHE) versus the average oxidation state of Co after electrochemical activation in carbonate, phosphate, and borate electrolyte.[63] Copyright 2021, Wiley. D) XPS spectra of Mn 2*p* for Mn_3N_2 before, and after CV and CP tests.[39] Copyright 2019, Wiley.

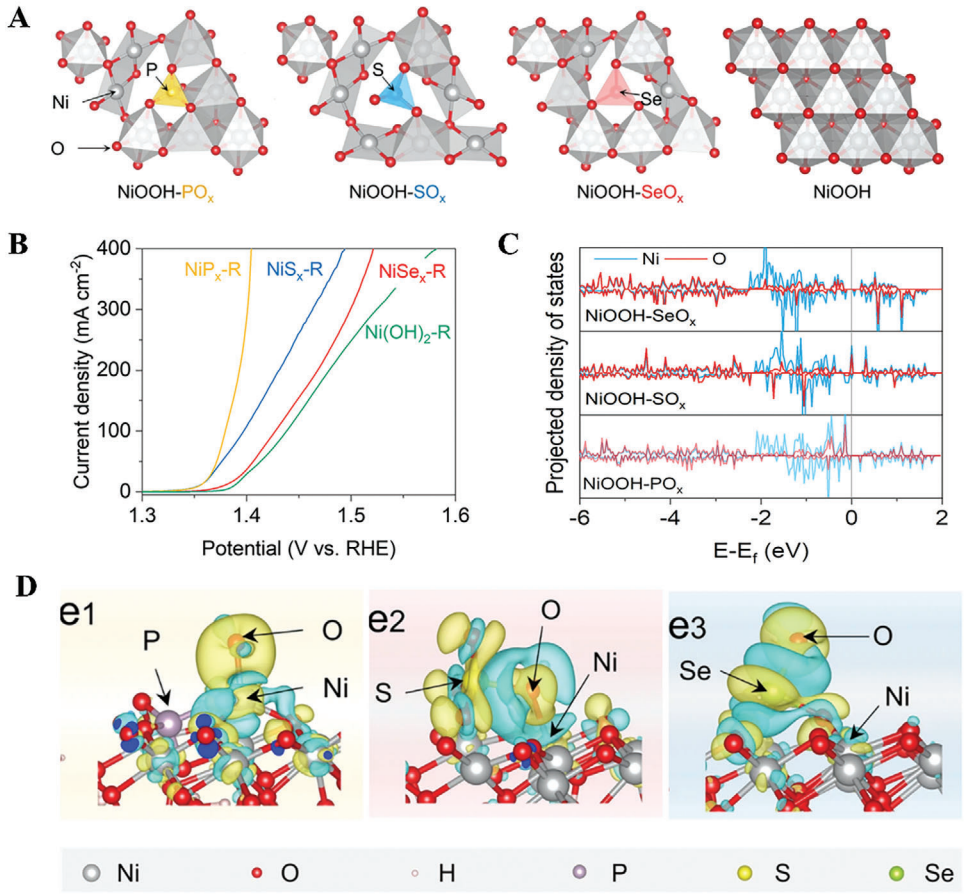

Figure 18. A) Diagram depicting structure model of PO_x-doped NiOOH, SO_x-doped NiOOH, SeO_x-doped NiOOH, and pure NiOOH. B) LSV curves of NiT_x-R and $Ni(OH)_2$-R. C) PDOS plots of O 2p band and Ni 3d for NiOOH-SeO_x, NiOOH-SO_x, and NiOOH-PO_x. D) Charge density difference upon adsorption of OH* intermediates on NiOOH-PO_x e1), NiOOH-SO_x e2), and NiOOH-SeO_x e3), respectively. Cyan represents electron depletion, while yellow signifies electron accumulation.[169] Copyright 2022, Nature Portfolio.

5.1.3. Defective Sites in Amorphous Species

Introducing defects into electrocatalysts has been reported as a promising method for enhancing the activity of catalysts.[189] Composition leaching and lattice oxygen oxidation during the electrochemical reconstruction process usually create defects on in situ formed amorphous species, which facilitates the adsorption and desorption processes of surface intermediates in electrocatalysis.[36,76,190] Zhou's study revealed that the amorphization of the NiCrO electrocatalyst occurred alongside the formation of cation and oxygen vacancies, which were driven by Cr leaching and lattice oxygen oxidation.[53] Abundant vacancies on the amorphous NiOOH layer (NiCrO-$V_{Cr,O}$) can be detected through electron paramagnetic resonance (EPR) signals (**Figure 20**A). NiCrO-$V_{Cr,O}$ exhibited outstanding performance in GOR, with glycerol conversion, formic acid formation selectivity, and faradaic efficiency values exceeding 90% across all cycles (Figure 20B). In situ attenuated total reflection surface-enhanced IR absorption spectroscopy (ATR-SEIRAS) revealed the adsorption characteristics of reactants and their oxidation intermediates on the catalysts (Figure 20C,D). The comparison of in situ ATR-SEIRAS spectra between NiCrO and NiCrO-$V_{Cr,O}$ indicated that glycerol oxidation on the defective amorphous surface was dependent on its ability to adsorb reactants and intermediates (Figure 20E). DFT calculations showed negative co-adsorption energies and individual adsorption energies for glycerol and OH^- on defective amorphous species (Figure 20F), favoring efficient electrocatalysis of glycerol.

Alternatively, more defects could be generated due to the co-leaching of unstable elements during in situ amorphization. Ni's group illustrated that the co-leaching of S and Cl from Co,Cl-NiS induced numerous vacancies on the in situ formed amorphous layer (Co-NiS_V@Co-NiOOH), contributing to the excellent EGOR performance.[77] DFT calculations indicated that the generation of vacancies regulated the catalyst's electronic structure by upshifting the d-band center (Figure 20G), which could improve the adsorption of reaction intermediates. In Figure 20H, in situ formed vacancies resulted in the release of more energy at the potential-determining step (PDS) in Co-NiS_V@Co-NiOOH compared to Co-NiS@Co-NiOOH. Co, Cl-NiS electrode in PET hydrolysate electrolysis contributed to a decreased applied potential, promoting efficient energy conversion (Figure 20I). A similar phenomenon can be observed on the amorphous surface layer of $NiSn(OH)_6$@OOH with Sn vacancies during the OER process.[175] Therefore, defects within the amorphous

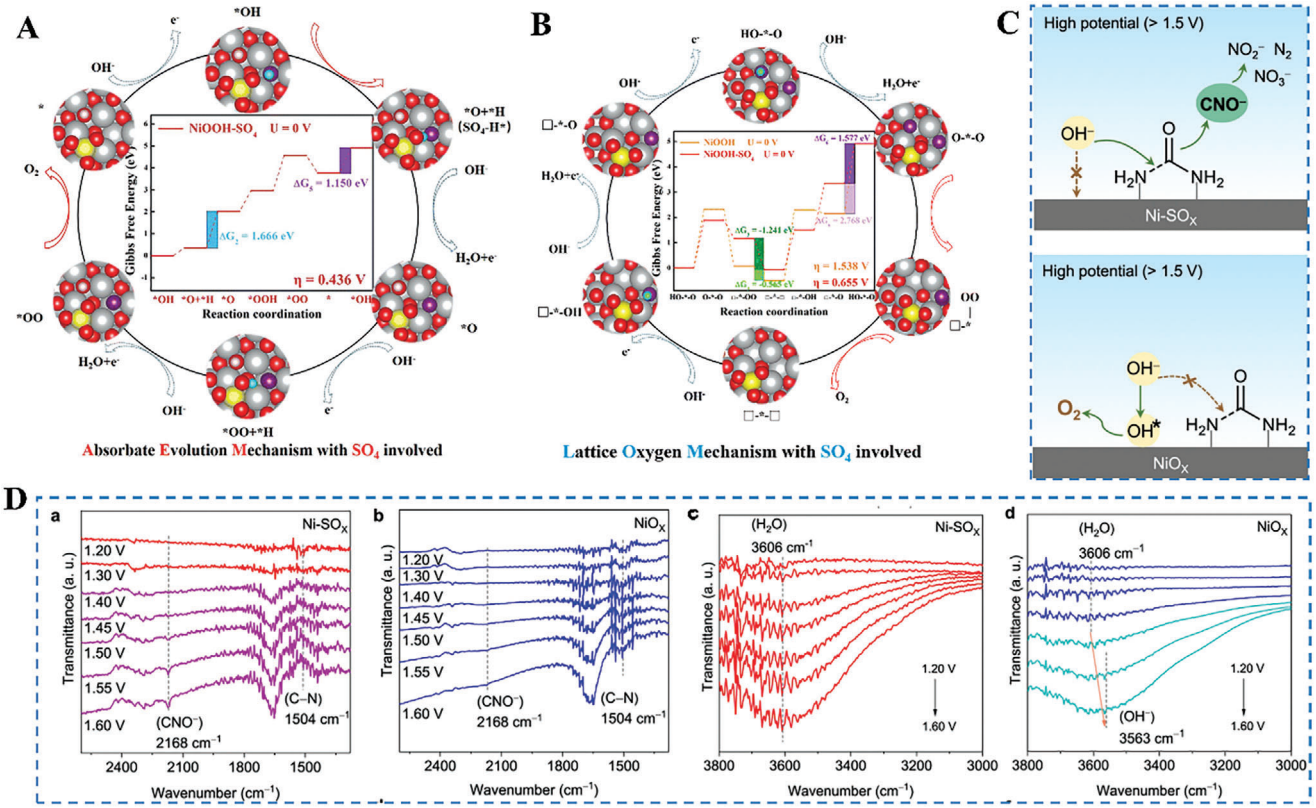

Figure 19. A) The OER pathway and reaction free energy diagram of products for NiOOH-SO_4 involving the AEM, B) and the LOM. The black and red arrows represent the electron-proton coupling step and the thermochemical step, respectively.[105] Copyright 2023, Royal Society of Chemistry. C) Sketch illustrating the selective oxidation of urea due to the competitive adsorption between hydroxyl and urea on Ni-SO_X and NO_X surfaces. D) In situ ATR-IR spectra of Ni-SO_X and NiO_X within the applied potential range of 1.20 – 1.60 V a–d).[174] Copyright 2023, Nature Portfolio.

surface could directly enhance reactant adsorption and may also modulate the electronic structure of electrocatalysts to refine the electrocatalytic process.

5.1.4. Amorphous-Crystalline Heterostructures

For most electrocatalysts undergoing in situ amorphization during electrochemical activation, the surface generally experiences reconstruction, resulting in an amorphous-crystalline heterostructure.[18b] This heterostructure can yield synergistic effects that enhance both the activity and stability of the electrocatalytic performance.[191] Amorphous phases, though rich in catalytic activity, often suffer from low electrical conductivity and insufficient stability in harsh oxidative and corrosive conditions, which restricts their electrochemical performance.[192] Amorphous-crystalline heterostructures feature an optimized electronic structure and electrical conductivity, which promote the electrocatalyst's activity and stability.[91] Zhao's group developed a single/double perovskite nanohybrid catalyst that achieved a tight interfacial interaction between amorphous and crystalline phases during electrocatalysis, resulting in a low overpotential of 268 mV at 10 mA cm^{-2}.[21] However, the continuous extension of the amorphous phase in the single perovskite decreased the electrochemical performance, requiring an overpotential of 330 mV.

The charge transfer and the conductivity of the electrocatalyst can be influenced by the self-formed amorphous-crystalline heterostructure. Hui's group found that in situ amorphization of F-$Ni(OH)_2$ induced the development of a heterogeneous structure, thereby enabling high electrocatalytic performance.[176] The amorphized F-$Ni(OH)_2$ exhibited semiconductor properties of both n-type and p-type. The space-charge effect was observed at the F-NiOOH/F-$Ni(OH)_2$ interface (**Figure 21**A), which could establish an active center on the amorphous F-NiOOH surface to accelerate the electron transfer with reactants during OER. The electronic interaction within the heterostructure was evidenced by the difference in Fermi energies between F-NiOOH and F-$Ni(OH)_2$ (Figure 21B,C). The lower Fermi energy of F-$Ni(OH)_2$, as compared to F-NiOOH based on their work functions, indicated directional electron transport across the interface from F-$Ni(OH)_2$ to F-NiOOH. In addition, the formation of heterostructures on F-$Ni(OH)_2$ altered its band gap and increased the total density of states (TDOS), significantly enhancing the material's electrical conductivity. This heightened conductivity was further evidenced by the proximity of the p-band center to the Fermi level. The improved electrical conductivity optimizes charge transfer during electrochemical reactions and enhances the binding capability with OER intermediates.

Similarly, the heterostructure in other catalysts could also facilitate electron transfer and optimize electronic structural, such as $Ni(OH)_2/Ni_2P_4O_{12}$,[177] $(NiFe)OOH/(NiFe)_3Se_4$,[178] and

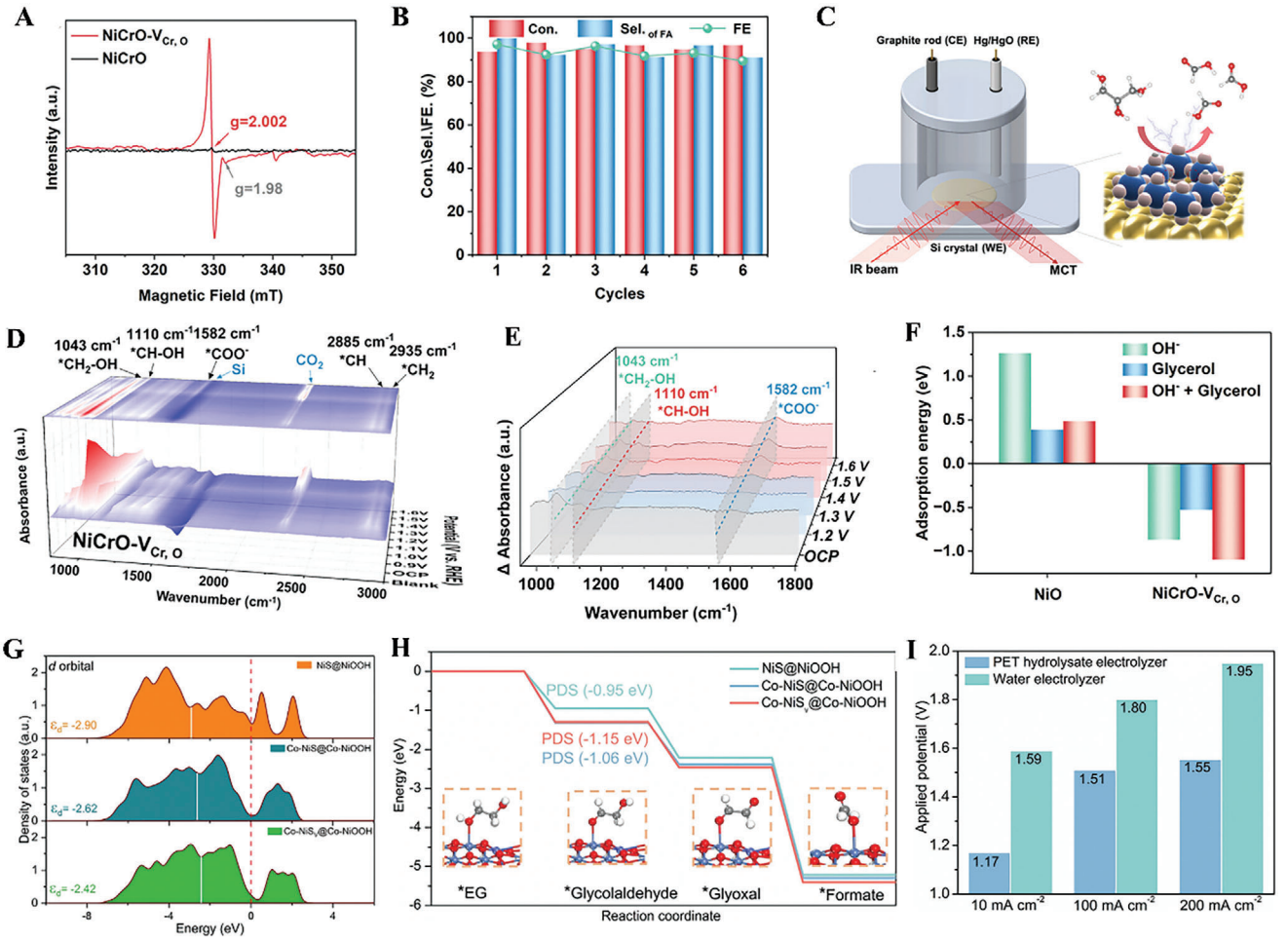

Figure 20. A) EPR spectra for catalyst with and without vacancies. B) Performance in terms of conversion, selectivity, and faradaic efficiency for NiCrO-$V_{Cr,O}$ across six successive electrolysis cycles. C) Diagram of in situ ATR-SEIRAS system. D) In situ ATR-SEIRAS spectra during electrocatalysis of glycerol on NiCrO-$V_{Cr,O}$ at the 0.1 V potential gradient. E) The adsorption characteristics of organic before and after glycerol electrooxidation by analyzing in situ ATR-SEIRAS spectra data for NiCrO-$V_{Cr,O}$ and NiCrO. F) Adsorption energies of reactants on the surface of NiO and NiCrO-$V_{Cr,O}$.[53] Copyright 2024, American Chemical Society. G) Density of states for Co-NiS$_v$@Co-NiOOH, Co-NiS@Co-NiOOH, and NiS@NiOOH. H) Gibbs free energy diagrams when EGOR occurred on the surface of Co-NiS$_v$@Co-NiOOH, Co-NiS@Co-NiOOH, and NiS@NiOOH. The inset presents the molecular arrangement of the different intermediates during EGOR. I) Variations in applied potentials across different current densities for the electrocatalysis of PET hydrolysate and water.[77] Copyright 2023, Springer.

NiVN@OOH.[179] The optimized electron configuration enhances the adsorption and transportation of catalytic intermediates at the active site. Furthermore, in situ formed amorphous-crystalline structure via the OER process may initiate a favorable lattice oxygen oxidation mechanism (LOM) process. It was illustrated by the study in Shao's group.[180] They regulated the composition of cubic (ABO_3) and PR (A_2BO_4) perovskite phases in the hybrid $La_{0.33}SrCo_{0.5}Fe_{0.5}O_x$ (H-LSCF), resulting in the induction of an optimal crystalline-amorphous hybrid structure following in situ electrochemical activation. They investigated that hybrid H-LSCF with crystalline-amorphous phases exhibited a more favorable lattice oxygen oxidation mechanism (LOM) process compared to pure-phase counterparts, potentially attributed to the heightened OH^- absorption on its crystalline-amorphous combination (Figure 21D).

The role of the amorphous/crystalline heterostructure in facilitating electrochemical oxidation is verified, and the spatial distribution of the heterostructure plays a crucial role in achieving effective electrochemical oxidation. Electrocatalysts with dense heterostructure interfacial sites have been reported to demonstrate superior electrochemical oxidation performance compared to those with sparse heterostructure interfaces.[193] Li et al. reported the generation of a distinctive congee-like NiOOH/Ni_3S_2 heterostructure from a precatalyst consisting of Ni_9S_8 and Ni_3S_2 during in situ electrochemical activation (Figure 21E).[181] In contrast to the sparse heterostructure with a NiOOH layer over Ni_3S_2, the dense NiOOH/Ni_3S_2 heterostructure showed an O_2-evolving current density of 10 mA cm^{-2} at a reduced overpotential of only 197 mV and a Tafel slope of 38.8 mV dec^{-1}. The abundant interfacial sites boosted electron transfer between amorphous NiOOH and Ni_3S_2, increasing the activity of the active sites and promoting the adsorption of products. In addition, in situ formed amorphous-crystalline heterostructures exhibited significant activity across various electrochemical oxidation pro-

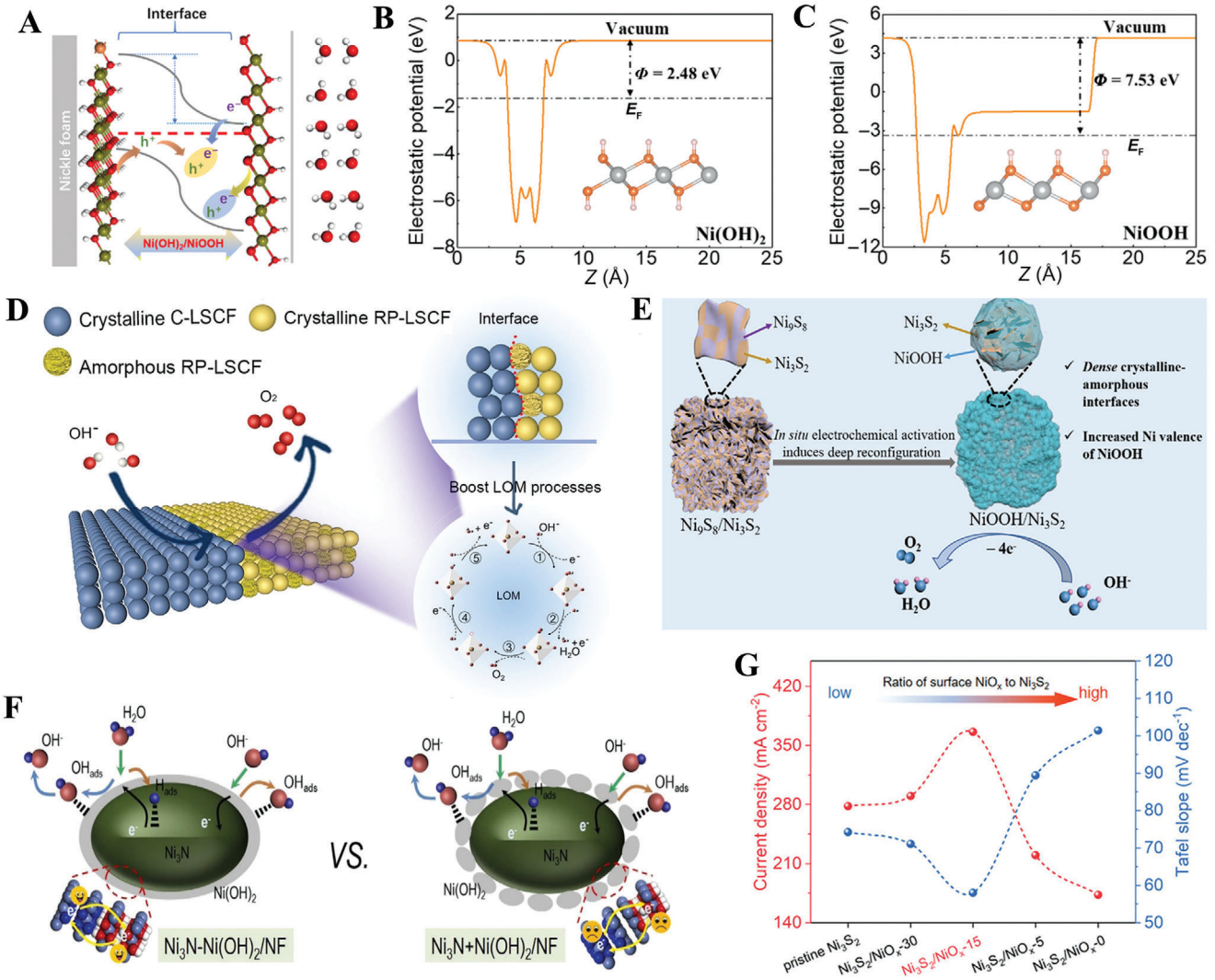

Figure 21. A) Electron transfer mechanism sketch on the F-NiOOH/F-$Ni(OH)_2$ p-n junction during the oxygen evolution process. Work function profiles of B) F-$Ni(OH)_2$ and C) NiOOH.[176] Copyright 2022, Springer. D) A schematic diagram illustrating the heterostructure interface and its facilitation of lattice oxygen reactions.[180] Copyright 2021, Elsevier. E) A schematic illustration depicting the in situ formation of a dense amorphous-crystalline heterostructure designed to enhance OER performance.[181] Copyright 2023, American Chemical Society. F) Schematic illustration of the reaction steps involved in alkaline HOR and HER on both the in situ formed Ni_3N-$Ni(OH)_2$ heterostructure and the electrodeposited Ni_3N+$Ni(OH)_2$ heterostructure.[182] Copyright 2023, Elsevier. G) Tafel slopes and current densities j) at 1.5 V versus RHE for pristine Ni_3S_2 compared to Ni_3S_2 with varying amounts of amorphous NiO_x.[23] Copyright 2023, Wiley.

cesses. As shown in Figure 21F, in situ-formed $Ni(OH)_2$-Ni_3N heterostructure significantly enhanced electron transfer at the heterostructure interface during the hydrogen oxidation reactions (HOR) reaction.[182] Additionally, the proportion of amorphous NiO_x on the crystalline Ni_3S_2 influenced the Tafel slope and current density of the electrocatalyst during the BOR reaction (Figure 21G).[23]

5.1.5. Stability Contribution of the Amorphous Structure

The amorphous structure, with its high strain, toughness, and isotropic properties, can endure the conditions of water splitting.[194] In situ formed amorphous species typically exhibit higher corrosion resistance compared to the precatalysts, enabling the maintenance of electrocatalyst's structure and ensuring stable electrocatalytic activity. Peng's group reported that an amorphous Fe-CoNiOOH layer was in situ generated on the $Zn(Fe, Al, Cr)_2O_4$ spinel phase due to the limited Al leaching under applied potential in alkaline conditions.[183] As shown in **Figure 22A**, continuous Al leaching enabled the creation of an active layer with a thickness of 15 nm, exceeding the typical few nanometers seen in other amorphous layers. Meanwhile, the stable amorphous structure can effectively prevent excessive leaching of Al ions, avoiding disruption of the catalyst's crystal structure. Therefore, an efficient and stable amorphous structure ensures consistent catalytic performance during the electrochemical process. During a 3000-cycle stability test using the

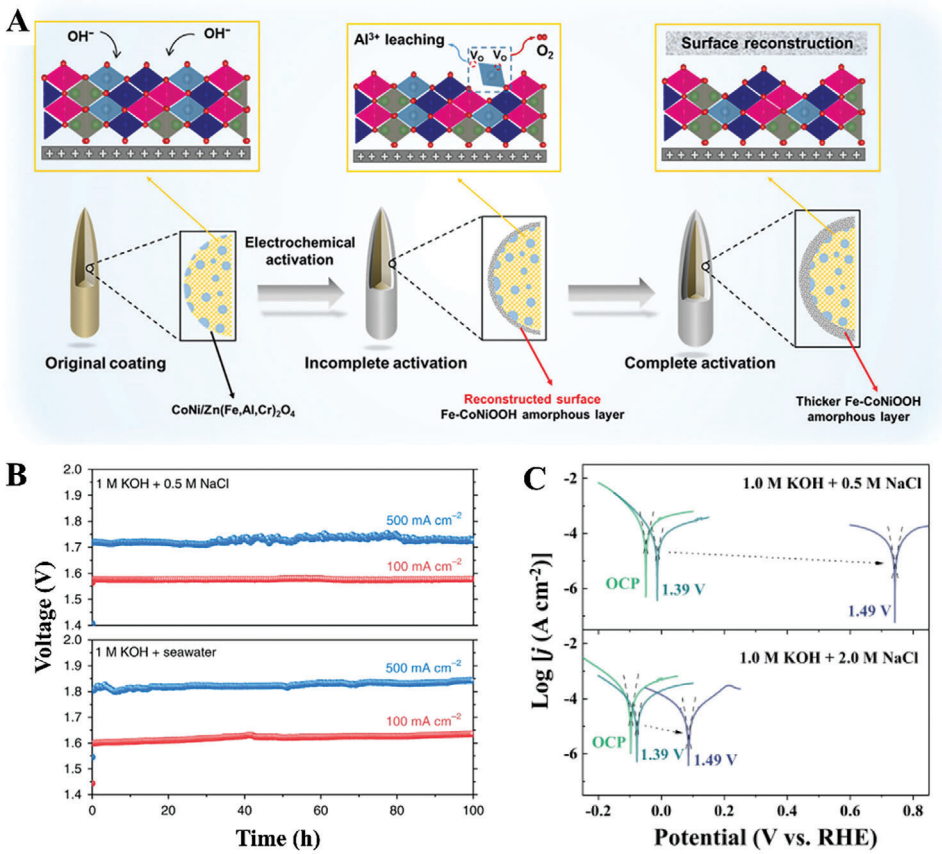

Figure 22. A) Schematic illustrating the generation of stable amorphous structures through Al leaching during electrochemical activation.[183] Copyright 2023, Wiley. B) Stability tests for the NiMoN@NiFeN applied constant current densities at 500 and 100 mA cm^{-2} in different electrolytes at 25 °C.[42] Copyright 2019, Nature Portfolio. C) Measurement of corrosion current densities (j_{corr}) and corrosion potentials (E_{corr}) for (Ni,Fe)O(OH)@NiCoS in potentiodynamic polarization curves in different electrolytes.[34] Copyright 2023, Elsevier.

CV method, the electrode's overpotentials at current densities of 10 and 100 mA cm^{-2} decreased to 255 and 342 mV, respectively. The electronic conductivity and number of active sites grew incrementally as amorphous species formed with more scanning cycles. When this electrocatalyst was used in subsequent sustained electrochemical testing, it achieved long-term stability at the current density of 500 mA cm^{-2} for 100 h. In situ formed amorphous phase serving as a protective shield is commonly observed in the reconstruction of electrocatalysts, such as the amorphous Ni/Fe oxyhydroxide on the $NiFe_{0.5}Sn$ alloy,[184] stability amorphous RuO_x shell on RuMn alloy,[185] and Li-containing Co (oxy)hydroxide on the $LiCoO_{1.8}Cl_{0.2}$.[117] Excessive amorphization causes a decline in electrocatalytic performance. Pang's group found that moderate amorphization of NiO-6, with its crystalline/amorphous structure, maintained a stable current density of 19.44 mA cm^{-2}.[167] In contrast, extensive amorphization of NiO-6S, characterized by its crystal properties, led to structural collapse and a gradual reduction in current density to 5.02 mA cm^{-2} during electrochemical activation.

Furthermore, the self-reconstructed amorphous structure could exclude chloride corrosion during alkaline seawater electrolysis, leading to an active and durable oxygen evolution reaction. Ren et al. reported that in situ evolved amorphous phase on the NiMoN@NiFeN was responsible for both the electrocatalytic activity and the superior chlorine corrosion resistance.[42] As shown in Figure 22B, the NiMoN@NiFeN catalyst in the water electrolyzer delivered consistent performance over 100 h, maintaining current densities of 100 and 500 mA cm^{-2} in both simulated and natural seawater, with minimal voltage increase. Shao et al. investigated the amorphous structure-durability relationships of (Ni,Fe)O(OH)@NiCoS in chloride resistance.[34] When the amorphous γ-NiOOH and FeOOH (denoted as γ-NiFeOOH for simplicity) formed with increasing activation potentials, the corrosion initial potentials (E_{corr}) exhibited a noticeable rise, while corrosion current densities (j_{corr}) decreased across different concentrations of NaCl electrolyte (Figure 22C). They proposed that amorphous γ-NiFeOOH selectively adsorbs and retains OH^- ions, thereby protecting the catalyst from the corrosive effects of Cl^- ions during the four-electron water oxidation reaction. Besides, time-of-flight secondary ion mass spectrometry analysis identified distinct sulfate gradient layers on the amorphous surface of the catalyst. These layers, enriched with $SO_x^{2-/1-}$ species, optimize the coordination environment of Cl^- ions by creating 3D repulsive layers, thereby enhancing the stability of electrocatalytic activity in seawater.

According to the above discussion, the differential evolution of self-evolved amorphous species may enhance the activity and stability of electrocatalysts during the electrochemical oxidation

process. Nevertheless, it is important to note that in some cases, the amorphous species may not function as the catalytically active site. He et al. reported that amorphous NiOOH made a negligible contribution to the active site.[195] The amorphous oxyhydroxide surface layer facilitated the interphase ion transport of $NiWO_4$-TA_{950}. At times, excessive amorphization of partial perovskite-based oxides could result in a decrease in catalytic activity.[21] Therefore, it is urgent to regulate the in situ amorphization process, aiming to establish a suitable amorphous structure through the rational design of precursor electrocatalyst materials and precise control of the reconstruction conditions.

5.2. Electrochemical Reduction Reactions

Electrochemical in situ reconstruction leading to the generation of amorphous phases has been documented in electrochemical reduction processes like the HER,[40,48] oxidation reduction reaction (ORR),[196] carbon dioxide reduction reaction (CO_2RR),[197] and nitrogen reduction reaction (NRR), etc.[198] Researchers have investigated the crucial role played by in situ generated amorphous active sites during the electrochemical reduction process.[94,154] Relevant studies are listed in **Table 2**. The function of in situ formed amorphous species in influencing the electrocatalytic reduction performance is deliberated in this section.

5.2.1. High Activities in Amorphous Structure

Different from the oxidation in the electrochemical oxidation reactions, precatalysts are typically transformed into lower metal states during the in situ reduction amorphization process. The generated amorphous reduction species are identified as the active sites. Qian et al. detected an amorphous Bi shell in real-time during CO_2RR on nanoporous AgBi (np-AgBi), indicating the catalytic involvement of Bi shell in simultaneous CO_2 conversion.[199] **Figure 23A** illustrates the reconstruction diagram. The thickness of the amorphous Bi layer increased with the reaction time of CO_2RR (Figure 23B). The thickest amorphous Bi shell of np-AgBi resulted in the highest faradaic efficiency, reaching 84.8% for $HCOO^-$ production. In situ generated amorphous Bi layer could facilitate the conversion of CO_2 to formate. In situ Raman spectroscopy showed a diminishing CO Raman band intensity, coupled with a persistent rise in *OCHO Raman band intensity as the reaction progresses (Figure 23C,D). DFT calculations indicated that the moderate adsorption-free energy for intermediates on amorphous Bi atoms resulted in excellent CO_2RR performance, leading to the formation of liquid products. Ye et al. also reported that the in situ formed amorphous Sn mass in Sn/SnS_2 samples correlated with their NRR yield (Figure 23E).[198b] Moreover, in situ formation of reductive amorphous species, such as amorphous $CoO_x(OH)$,[50] amorphous CoS_x,[37] and amorphous Co-P alloys,[200] similarly occurred during the hydrogen evolution reaction, significantly improving the production of H_2.

The reconstructed amorphous phases, exhibiting an appropriate coordination environment, serve as effective supports for electrochemical reduction catalysis. Viswanathan et al. investigated the amorphous film with a nominal NiS stoichiometry, which was in situ coated on the Ni_3S_2 under ORR conditions. These films displayed high activity for ORR catalysis.[196a] Through DFT calculations, the author investigated the source of the increased activity for the in situ formed amorphous phase, establishing a correlation between the coordination environment of active sites and their electrochemical activity across various structural phases. Figure 23F illustrates the amorphous structure catalyst composed of Ni:S in a 1:1 ratio. The amorphous species displayed active Ni sites linked to three sulfur atoms. This configuration affects the adsorption free energy of *OH, thereby boosting the activity in the ORR.

At times, the formation of amorphous species in reduction electrochemical reactions could modulate the electronic structure of active sites. Meng et al. prepared amorphous electrocatalysts ($MoO_x/Co(OH)_2$) through electrochemical reduction activation of $MoO_2/Co(OH)_2$ in an alkaline solution.[201] The amorphous $MoO_x/Co(OH)_2$/NF displayed a notably low overpotential of 23 mV at 10 mA cm^{-2}, clearly outperforming the $MoO_2/Co(OH)_2$/NF (46 mV). The alkaline exchange membrane electrolyzer utilizing $MoO_x/Co(OH)_2$/NF and NiFe-LDH/NF for hydrogen production required only 2.25 V at 500 mA cm^{-2}, exhibiting higher efficiency than nickel foam. The formation of amorphous MoO_x (MoO_4^{2-}) was associated with the leaching of Mo during the electrochemical activation, thus causing the transition of Co-O-Mo^{4+} into Co-O-Mo^{6+}. The O p-band was brought closer to the Fermi energy level (E_F) by an increase in Mo valence (Figure 23G). This proximity influenced the d-p band overlap between Mo and O, enhancing electron transfer. It also activated the oxygen p-orbitals, enabling them to accumulate electrons more effectively, which ultimately boosts the activity of the oxygen sites in the HER. Figure 23H shows that as Mo valence increased, electrons moved from Mo to O sites, accumulating at these O sites and creating active sites for hydrogen adsorption during HER. Therefore, the electronic structure of the Mo-O bond is optimized during the amorphization, leading to the regulation of the adsorption energy of H^*/H_2O and the enhancement of the HER performance.

5.2.2. Amorphous-Crystalline Heterostructures

The generation of amorphous-crystalline heterostructure interfaces can originate from either a precatalyst heterojunction or limited amorphization.[196a,202] The distinct heterostructure interface has been proven to enhance the electrochemical reduction reaction by controlling electron transfer between the two phases. Zhang et al. observed the emergence of a heterostructure after the amorphization of crystalline In_2O_3 during CO_2RR.[203] In/In_2O_{3-x} not only demonstrated lower onset potentials of ≈_0.52 V versus RHE and higher current densities compared to In, but also sustained consistent current densities for 10 h during CO_2RR (**Figure 24A**). Ultraviolet photoelectron spectroscopy (UPS) results demonstrated the formation of a Schottky contact at the In/In_2O_{3-x} heterojunction, enabling electron flow from In_2O_{3-x} to In (Figure 24B). DFT calculation demonstrated that less energy was required for In/In_2O_{3-x} to produce formate compared to In and In_2O_3, rather than producing CO (Figure 24C,D). This electrocatalyst, featuring a tailored electronic structure, was utilized in a two-electrode cell setup (Figure 24E), showcasing

Table 2. The list of self-evolved amorphous phases under electrochemical reduction processes.

Precatalyst	Reaction	Electrochemical condition	Amorphous species	Role of amorphous species	Ref.
NiS_2	HER	CA: a constant potential of −0.4 V vs RHE, 1 M KOH solution	Co-Ni sulfides	An amorphous sulfide film structure enriched with nickel temporarily boosts HER activity	[154]
Aligned Co-Fe phosphate (Co-FePO)	HER	CA: a constant potential of −0.17 V vs RHE for 30 min, 1 M phosphate-buffered saline	Co-FePO/OH	Amorphous Co-FePO/OH hybrid electrocatalyst enhances water dissociation in the Volmer step	[94]
Nanoporous AgBi	CO_2RR	CA: a constant potential of −1.05 V vs RHE for 135 min, CO_2 saturated 0.1 M $KHCO_3$ solution	Bi shell	Amorphous Bi shell exhibits efficient performance in CO_2 activation	[199]
SnS_2	NRR	CV: −1.3 to −0.2 V vs RHE at 50 mV s^{-1} for 20 cycles, 0.1 M HCl solution	Sn (Sn^0)	Amorphous Sn enhances electrochemical reduction activity toward N_2 reduction	[198b]
$Co_3(OH)_2(HPO_4)_2$	HER	CA: an overpotential of 130 mV in HER for 10 h, 1 M KOH solution	$CoO_x(OH)$	in situ formed reductive Co^0 markedly decreases the energy required for hydrogen adsorption	[50]
Imidazole based MOFs	HER	CV: −1.76 to 0.15 V vs Ag/AgCl for 1200 cycles, an N_2-saturated 0.5 M thiourea solution with 0.1 M KCl	CoS_x	Amorphous CoS_x with a high content of S_2^{2-} species serves as the catalytically active site	[37]
CoP	Acid HER	CV: −0.266 to −0.406 V vs SCE at 1 mV s^{-1}, 0.5 M H_2SO_4 solution	Co-P alloys	Co in a near-zerovalent state and P in a reduced state contribute to enhanced activity	[200]
Crystalline Ni_3S_2	ORR	CV: 0 to 1.0 V for 10 – 20 cycles at 5 mV s^{-1}, N_2-saturated 1 M sodium phosphate solution	Amorphous surface layer with NiS stoichiometry	Ni sites coordinated with the three nearest sulfur surroundings enhance the ORR activity	[196a]
$MoO_2/Co(OH)_2$/NF	HER	CA: a constant potential of −1.2 V vs SCE for 12 h, 1.0 M KOH solution	MoO_x	High-valence Mo^{6+} optimizes the p-band center of O and enhances intermediate adsorption	[201]
$W_{18}O_{49}/NiWO_4$	HER	CA: a constant potential of −1.3 V vs RHE for 12 h, 1.0 KOH solution	H-AM/$NiWO_4$/NF	Amorphous-crystalline interface benefits the decrease of interfacial energy	[202]
Crystalline In_2O_3	CO_2RR	LSV: −0.7 to −1.9 V vs SCE until the curve kept unchanged, 0.5 M $NaHCO_3$ solution	In_2O_{3-x}	In situ formed In/In_2O_{3-x} heterostructure tailors the electronic structure of electrocatalyst	[203]
Dealloyed composite contains cubic and hexagonal CeO_2, Cu_2O, and Cu	CO_2RR	CA: potentials from −0.5 to −0.8 V vs RHE, 1.0 M KOH solution	CeO_2-Cu	CeO_2-Cu interfacial sites guide the reaction pathway toward the production of C_{2+} alcohols	[204]
Nanoporous Ag-Bi	CO_2RR	CA: a constant potential of −1.0 V vs RHE for 3 h, CO_2-saturated 0.1 M $KHCO_3$ solution	Bi_2O_3 shell	Amorphous Bi_2O_3 shell switches the catalytic products from CO to formate	[205]
Boron-rich covalent organic frameworks (COFs)	NRR	CA: a constant potential of −0.2 V vs RHE for 20 min, N_2-saturated 0.1 M KOH solution	Amorphous COF	An amorphous phase enhanced N_2 physisorption on the catalyst	[198a]
Zr-based MOF coated Cu catalyst (UiO-66/Cu)	CO_2RR	CA: a constant potential at 1.05 V vs RHE for 1 h, 0.1 M $KHCO_3$ solution	ZrO_x	Amorphous ZrO_x attributes to the selective production of C_{2+} chemicals	[197]
Ru-$NiPS_3$ nanosheets	HER	CP: a fixed current density of −100 mA cm^{-2} for 45 h, 1 M KOH solution	Amorphous layer with abundant bridging S_2^{2-} species	The stabilization of active sites leads to improved adsorption capacity for intermediates	[70]

(*Continued*)

Table 2. (Continued)

Precatalyst	Reaction	Electrochemical condition	Amorphous species	Role of amorphous species	Ref.
CuAl-oxide-derived catalyst	CO_2RR	CV: 0 to −1.98 V vs RHE at a rate of 100 mV s^{-1} for 10 cycles, 1 M KOH solution	Al_2O_3	Amorphous Al_2O_3 phase enhanced the stability of active Cu^+ sites	[206]
CoMn-S@NiO	HER	CA: a constant potential of −1.4 V vs Ag/AgCl for 5000 s, 1.0 M KOH solution	Amorphous surface with S leaching	An amorphous layer appears to stabilize the catalysis performance	[207]
$BiFeO_3$	NRR	CA: a constant potential at −0.6 V vs RHE for 20 min, 0.1 M KOH solution with 0.1 M KNO_3	Reduction state of Fe and Bi on the amorphous surface	Preserves the catalyst's high activity during the long-term catalytic process	[208]
V-incorporated Ni_xS_y nanowires (VS/Ni_xS_y)	HER	LSV: −1.0 to −1.5 V at least 20 scans until the HER activity was stable, 1.0 M KOH under a N_2 atmosphere	VOOH and NiOOH	Amorphous VOOH film enhances the HER process, while NiOOH protects sulfide species against dissolution	[209]

elevated performance in CO_2RR and specificity toward formate generation (Figure 24F).

Additionally, the amorphous-crystalline heterostructure influences the adsorption behavior of intermediates, altering the reduction products. Li et al. created a CeO_2-Cu heterostructure during CO_2 reduction, which could steer the production of C_{2+} alcohols (Figure 24G).[204] Theoretical calculations suggested that interfacial sites within the CeO_2-Cu heterostructure enhanced the adsorption of critical intermediates (*CO and *CH_2CHO) and promoted C-C coupling (Figure 24H). Besides, the required free

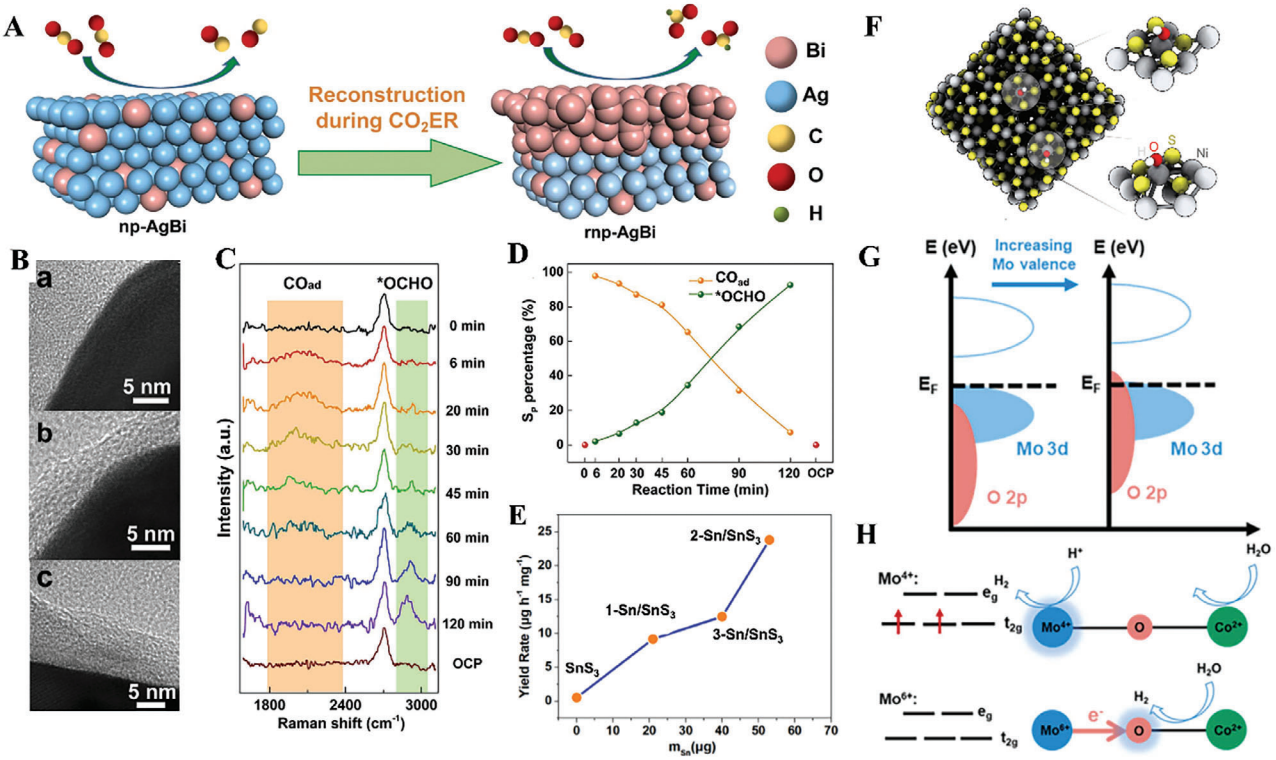

Figure 23. A) Diagram illustrating the reconstruction of np-AgBi to induce selectivity transformation of the product. B)HR-TEM images of np-AgBi under CO_2RR for 0 a), 30 b), and 135 c) minutes at _1.05 V. C) In situ Raman spectra of np-AgBi during various reaction stages of CO_2RR. D) Changes in the intensity of CO_{ad} and *OCHO Raman peaks over Co_2RR reaction time.[199] Copyright 2024, Elsevier. E) The correlation between the mass of amorphous Sn loading and the maximum ammonia yield.[198b] Copyright 2019, Wiley. F) The simulation structure of amorphous NiS catalyst.[196a] Copyright 2017, Cell Press. G) The overlap between the O 2p orbitals and Mo 3d orbitals changes with the valence of Mo. H) Schematic illustrating the changes in Co-O-Mo active sites induced by reconstruction.[201] Copyright 2024, Elsevier.

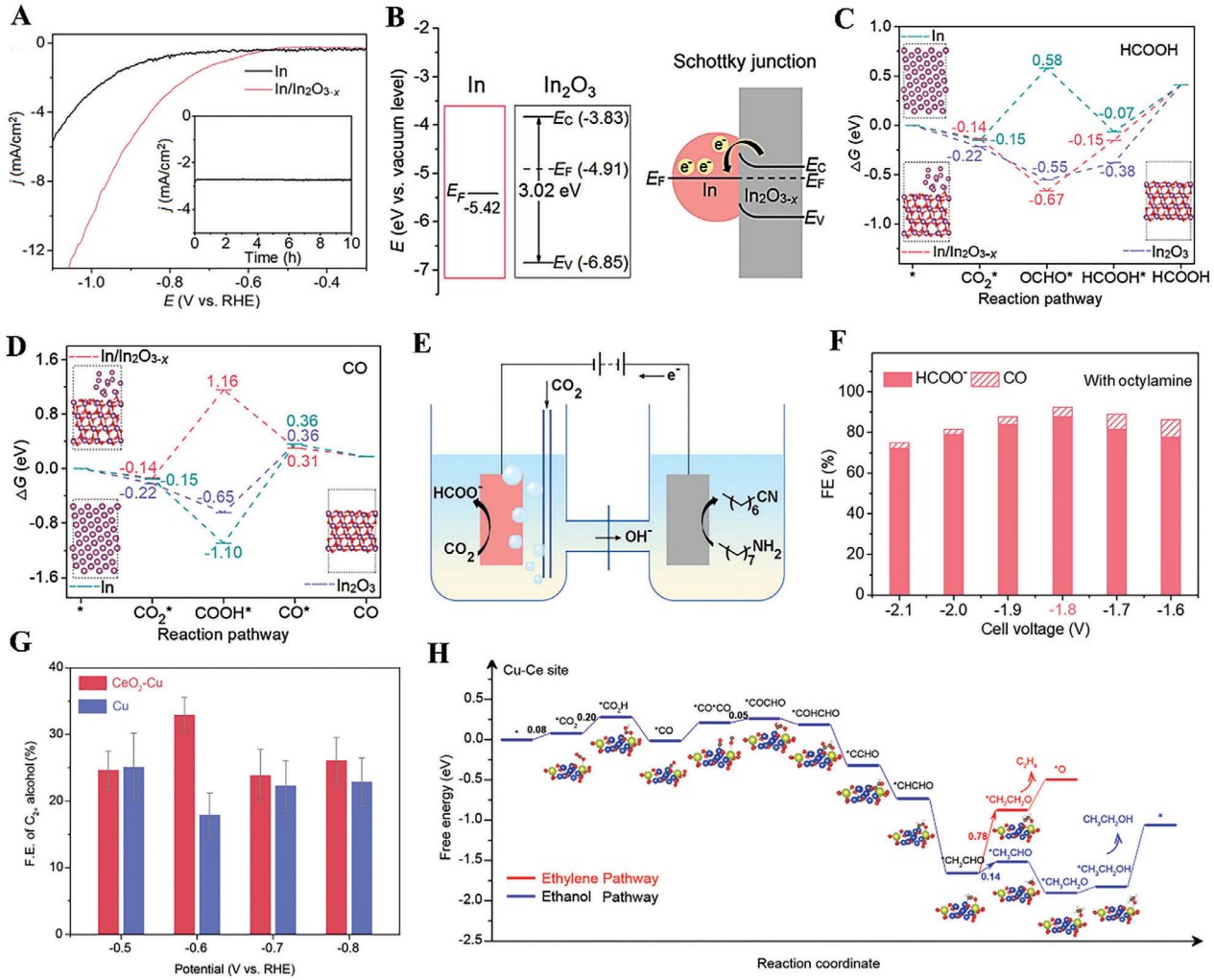

Figure 24. A) Comparative analysis of In/In_2O_{3-x} and In performance in LSV curves. Inset: Dynamic current density plot for In/In_2O_{3-x}. B) From left to right: Band structures of In and In_2O_3, along with a schematic representation of the In/In_2O_{3-x} Schottky junction. (E_F, representing the Fermi level; E_V, corresponding to the valence band; and E_C, indicating the conduction band). Calculated Gibbs free energy diagrams of In, In/In_2O_{3-x} and In_2O_3 to produce C) formate and D) CO. E) Schematic illustration of a two-electrode electrolyzer cell coupling CO_2 reduction with the octylamine oxidation reaction. F) Faradaic efficiencies for CO and formate production in the electrolyzer.[203] Copyright 2020, Elsevier. G) Faradaic efficiencies of Cu and CeO_2-Cu catalysts for C_{2+} alcohol production across various potentials. H) Free energy diagrams of the products during electrocatalysis over Cu-Ce sites on the heterostructure, from CO_2 to ethylene versus ethanol. The configurations of the adsorption intermediates are shown in each state.[204] Copyright 2022, American Chemical Society.

energy for the C-C coupling step (*COCHO) was only 0.05 eV. Notably, the Cu-Ce binary center within the heterostructure played a significant role in stabilizing the $*CH_2CHO$ intermediate, thereby guiding the formation of C_{2+} alcohols. The higher free-energy barrier of ethylene compared to ethanol over the Cu-Ce site facilitated the selectivity of electrocatalysis. In a flow cell with an alkaline electrolyte, the CeO_2-Cu catalyst reached a faradaic efficiency of 32.9% ± 2.6% for C_{2+} alcohols, operating at a reduced potential of −0.6 V versus RHE.

5.2.3. Selectivity Regulated by Amorphous Species

Amorphization of electrocatalysts during electrochemical reduction may alter the transformation pathways of intermediates, achieving selective conversion. Qian et al. investigated that the formation of an amorphous Bi_2O_3 shell promoted formate production during the CO_2RR (**Figure 25**A).[205] The amorphous Ag-Bi bimetals (a-NPSB) exhibited higher performance than Bi nanoparticles, delivering a specific current density of 21.2 mA cm^{-2} and a mass specific current density of 321 mA mg^{-1} at −1.15 V versus RHE, alongside an 88.4% Faradaic efficiency for producing formate. Following the elimination of the amorphous layer on the catalyst by multiple CV cycles, a significant improvement in CO production activity was observed, while this effect diminished over time due to the in situ regeneration of amorphous species again (Figure 25B). In situ development of distinct amorphous species may guide the mode of adsorption of intermediate, facilitating the selective transformation of reactants. Wu et al. employed in situ

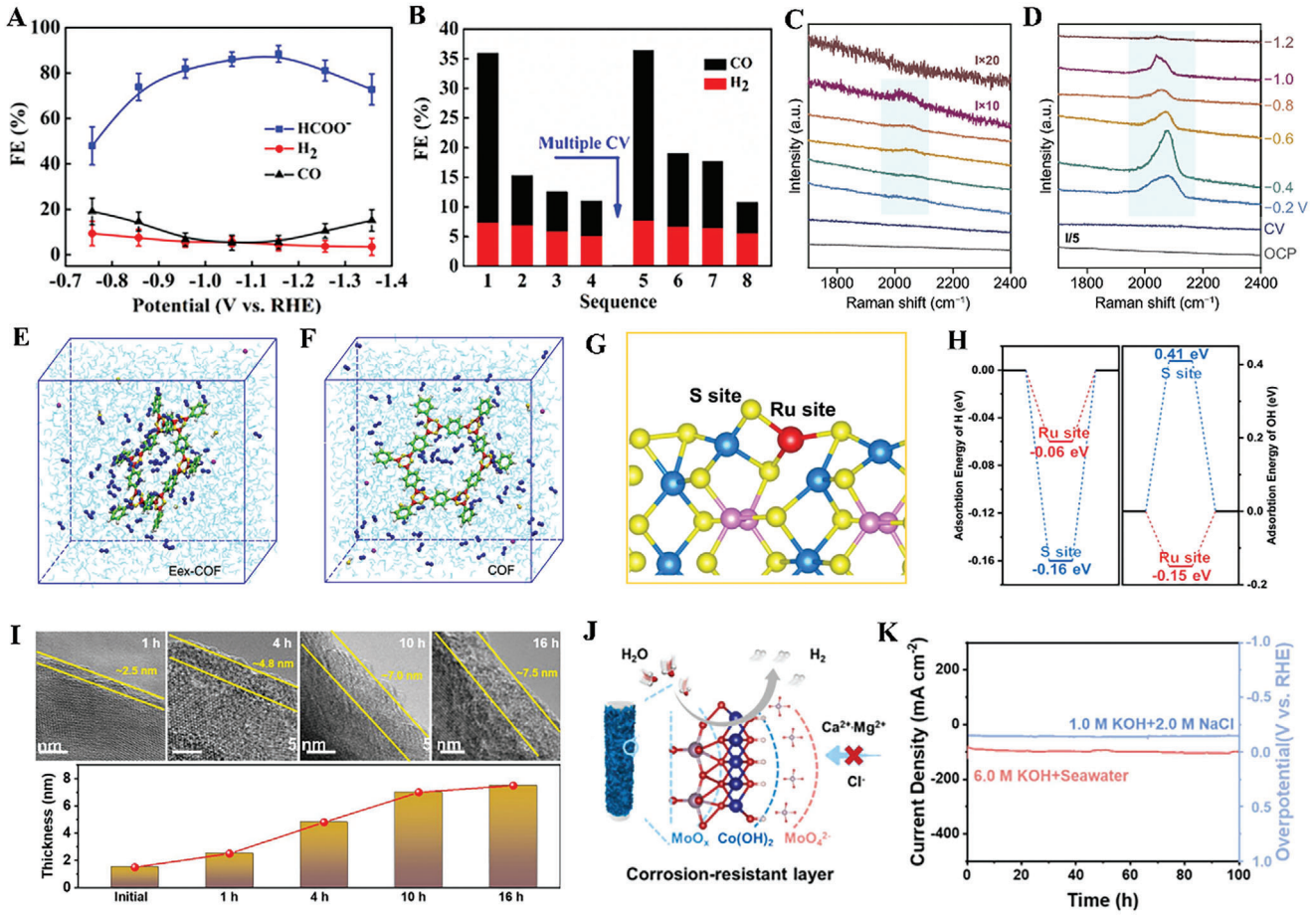

Figure 25. A) Faradaic efficiencies of CO_2RR products catalyzed by amorphous Bi_2O_3 at different potentials. B) Faradaic efficiencies of gas products (CO and H_2) during CO_2RR on the catalyst with iterative amorphization at −1.0 V.[205] Copyright 2020, American Chemical Society. In situ Raman spectra of C) the catalyst after removing the UiO-66 coating layer and D) UiO-66/Cu during the CO_2RR process at the applied potential from −0.2 to −1.2 V versus RHE.[197] Copyright 2022, Springer. Snapshots of molecular dynamics simulations for E) E_{ex}-COF and F) COF. The spheres are color-coded as follows: red for B, green for C, blue for N, yellow for O, and grey for H atoms.[198a] Copyright 2019, Nature Portfolio. G) Diagram of the configuration between the Ru atom and the bridging S_2^{2-} layer on the amorphous surface. H) H* and OH* adsorption energy on the active sites of amorphous structure. I) TEM images of Ru-$NiPS_3$ and the thickness of the amorphous layer after stability tests at different durations.[70] Copyright 2023, Nature Portfolio. J) Schematic diagram of the corrosion resistance on in situ formed amorphous layer. K) Stability measurement of in situ amorphized catalysts in the simulated and natural seawater solution.[201] Copyright 2024, Elsevier.

surface-enhanced Raman spectroscopy to demonstrate the optimized adsorption of intermediates on the in situ generated amorphous ZrO_x of UiO-66/Cu during the CO_2RR process.[197] The intensity of the atop-bound *CO intermediate signal notably increased upon the derivation of amorphous ZrO_x (Figure 25C,D). The stabilization of atop-bound CO* intermediates on the catalyst surface could facilitate the C-C coupling process for the selective production of C_{2+}.

Otherwise, the presence of amorphous species could enhance the adsorption of target reactants, thereby promoting selective electrochemical reduction. Yang et al. discovered that the pronounced amorphization of boron-rich COFs significantly enhanced N_2 adsorption within the COF networks.[198a] Molecular dynamics (MD) simulations explored that the amorphous structure on the electrochemically excited COF (E_{ex}-COF) promoted the aggregation of N_2 molecules around the catalyst (Figure 25E,F). The increased N_2 physisorption by the amorphous phase greatly improved gas diffusion and supply toward the active sites, thus facilitating the NRR reaction. The Faradaic efficiency and NH_3 yield rate of E_{ex}-COF/NC reach their maximum values of 45.43% and 12.53 μg h^{-1} mg^{-1}, respectively, at −0.2 V versus RHE. Therefore, the favorable adsorption of reactants and intermediates on amorphous species could enhance the selectivity transform in electrocatalysis.

5.2.4. Stability Contribution of the Amorphous Structure

In situ amorphization of electrocatalysts can result in the formation of a new stable structure during electrochemical reduction. A restricted amorphous layer could act as a host for robust active sites and demonstrate resilience against catalyst degradation. Zhao et al. proposed that in situ reconstructed amorphous surface, abundant in bridging S_2^{2-} species, could stabilize the

active site Ru, resulting in superior HER activity and remarkable durability of Ru-$NiPS_3$.[70] Ru-doped $NiPS_3$ reached an exchange current density of 1180 μA cm^{-2}. The electrode also demonstrated remarkable durability for 45 h at a constant current density of 100 mA cm^{-2}. Various characterization methods indicated the formation of a stable amorphous shell enriched with Ru^{4+} during the HER process. DFT calculations exposed the strong interaction of Ru with the bridging S_2^{2-} amorphous layer ($NiPS_3$-ac-Ru-1), leading to enhanced structural stability (Figure 25G). Moreover, $NiPS_3$-ac-Ru-1 resulted in H* species being anchored at the S site with an energy of −0.16 eV and OH* species at the adjacent Ru site with −0.15 eV (Figure 25H). These dissociative adsorption sites effectively safeguard the catalyst from active site poisoning, thus improving catalyst durability. Therefore, the formation of the amorphous layer with S_2^{2-} effectively stabilized Ru active sites and prevented its poisoning. In addition, Figure 25I indicates that the amorphous structure remained stable after prolonged electrochemical activation, effectively enhancing stability.

Therefore, in situ reconstruction of amorphous structures not only stabilized the active sites but also reinforced the catalyst's structural stability. The occurrence of a similar phenomenon involving in situ formation of an amorphous layer is widely acknowledged. Likewise, Han et al. engineered an amorphous Al_2O_3 phase via in situ electrochemical methods, enhancing the stability of active Cu^+ sites to facilitate the production of C_{2+} compounds.[206] Stable amorphous structures have also been reported in other studies, such as the amorphous layer on the CoMn-S@NiO[207] and amorphous $BiFeO_3$.[208] In addition, Liu's group inferred that an amorphous NiOOH surface on VS/Ni_xS_y may protect sulfide species from corrosion in alkaline conditions, thereby maintaining high efficiency for alkaline HER.[209] Moreover, Meng et al. reported that in situ formed MoO_4^{2-} on an amorphous layer exhibited resistance to seawater anions (Figure 25J).[201] Over a 1000 h test at a current density of 500 mA cm^{-2}, MoO_x/$Co(OH)_2$/NF exhibited only a limited decline in activity. Even with extended exposure to more harsh conditions during electrochemical stability testing, MoO_x/$Co(OH)_2$ demonstrated consistent electrochemical performance over 100 h (Figure 25K).

In contrast to the electrochemical oxidation process, there has been relatively limited investigation into in situ amorphization during reduction reactions. The role of the amorphous species formed during reduction processes is analogous to that observed during oxidation processes. Besides, the transition to an amorphous structure also can impede the electroreduction activity.[210] It is imperative to conduct more research to explore the amorphization process and the reactivity of in situ formed amorphous species.

6. Conclusion and Outlook

This review showcases recent advancements in comprehending the in situ amorphization process of electrocatalysts. By leveraging both ex situ and in situ characterization techniques, researchers can pinpoint amorphous species and track the amorphous transformation process. Amorphization primarily stems from redox reactions within electrocatalysts under specific electrocatalytic conditions, involving pathways like metal dissolution-reprecipitation, diverse redox reactions, and atomic rearrangement. Various electrocatalysts undergo distinct amorphization during self-reconstruction. Strategies to regulate amorphization, such as ion substitution, doping, and engineering heterogeneous structures, have been applied to tailor the intrinsic properties of catalysts. Moreover, morphological features of electrocatalysts, such as size, density, and porosity, significantly influence the amorphization process. Electrochemical operational parameters like potential and specific anions in electrolytes can also affect the activity of amorphous species and the kinetics of amorphization. These approaches can help to control the degree of amorphization and promote diverse amorphous structures, thereby impacting electrochemical activity.

Understanding the implications of in situ-generated amorphous layers remains a challenge. In electrochemical oxidation/reduction reactions, these amorphous species are believed to provide highly active sites, thereby amplifying the inherent catalytic efficacy of electrocatalysts. Besides, the presence of amorphous species with varying coordination environments and defects, as well as the formation of amorphous-crystalline interfaces, can markedly impact the activity of catalytic sites and alter the adsorption energies of reactants and intermediates. Moreover, the stability and selectivity of electrocatalysts can be enhanced through the formation of amorphous layers. Unfortunately, certain catalysts may experience a decrease in catalytic activity and stability following amorphization or excessive amorphization. There is currently a lack of research uncovering the mechanisms behind the formation of highly active amorphous species. Several challenges and opportunities can be delineated in this regard.

Electrocatalysts undergo dynamic reconstruction to form amorphous structures during electrochemical activation, influenced by factors such as the inherent properties of catalysts, operating conditions, and reaction environments. In situ/*Operando* techniques are suggested to monitor instantaneous alterations in the structure, composition, and electronic properties of catalysts. In addition, in situ technologies can be employed to monitor the dynamic processes at the catalyst-electrolyte interface, such as the adsorption and transformation behaviors of intermediates on the catalyst surface, and the degradation process of the catalyst. Importantly, the local properties of catalysts are critical for the catalytic process. Therefore, advanced characterization technologies with temporal sensitivity and high resolution are urgently needed to uncover the spatial amorphization process, such as atom probe tomography (APT), scanning electrochemical microscopy, and AFM.

The precise reason for the generation of amorphous structures during different electrochemical reactions is not fully mastered. While most efforts have concentrated on exploring the phenomenon of amorphization, it is essential to explore the correlation between precatalysts' electronic structure and the intrinsic factors that induce amorphous evolution. Theoretical calculations can help in assessing the amorphization process by constructing an appropriate model. On the other hand, considering alternative methods such as machine learning could contribute to predicting the evolution of amorphous structures, given the complexity of various electrochemical reaction conditions and intermediates.

During electrocatalysis, the active sites of catalysts change due to in situ amorphization, and catalytic intermediates may

influence the evolution of amorphous structural dynamics. Establishing universal principles to elucidate structure-activity relationships poses a challenge due to the complex nature of catalyst amorphization. Therefore, it is crucial to analyze the real-time distribution of products and the relationship between amorphous structural evolution. By comprehensively analyzing the relationships between catalyst structure, reaction efficiency, and product distribution, researchers can identify key factors regulating catalytic performance. This knowledge not only enhances our fundamental understanding of electrocatalytic processes but also facilitates the design of tailored electrocatalysts with optimized properties for specific applications, ultimately leading to improved efficiency and selectivity in various electrochemical reactions.

The in situ generated amorphous structures exhibit enhanced activity and stability, enabling selective transformations in electrochemical processes and offering significant potential for various applications. The catalytic performance of the in situ amorphized electrocatalyst relies on both the degree of amorphization and the properties of the amorphous species. To achieve high selectivity transformations to specific products, further exploration is needed to develop suitable catalysts. Despite the promising performance of reconstructed amorphous catalysts, their practical application remains limited to laboratory experiments. Advanced theoretical calculation methods can be employed for catalyst design, allowing rapid screening and optimization of catalyst candidates with desired properties. Coupled with experimental validation, wherein catalyst performance is assessed under realistic operating conditions, these computational tools can significantly expedite the development of effective catalytic materials.

In conclusion, this review underscores the significance of understanding in situ amorphization of electrocatalysts. A comprehensive understanding of the mechanisms underlying amorphous formation, regulation of amorphous structure formation, and elucidation of amorphous phase activity are crucial steps in exploring amorphization in electrocatalysis. However, achieving a thorough understanding of amorphization and precise control of amorphous activity remains challenging due to the complexity of in situ amorphization processes. In the future, advanced characterization techniques and theoretical computational methods could be employed to deepen understanding of the mechanisms behind amorphization. Furthermore, the application of advanced computational strategies, such as machine learning that harnesses extensive existing research data and sophisticated algorithms, may uncover complex relationships between amorphization and its influencing factors. This approach would support the rational design of catalysts and the optimization of electrochemical conditions, ultimately enabling controlled amorphization of electrocatalysts.

Acknowledgements

This work was supported by the Australian Research Council (ARC) Discovery Projects (DP220101139 and DP220101142). Dr. Wei Wei acknowledges the support of the ARC through project DE220100530. Dr Sergio Vernuccio acknowledges the support of the Worldwide University Network Research Development Fund.

Open access publishing facilitated by University of New South Wales, as part of the Wiley - University of New South Wales agreement via the Council of Australian University Librarians.

Conflict of Interest

The authors declare no conflict of interest.

Keywords

electrocatalysts, electrochemical oxidation reactions, electrochemical reduction reactions, in situ amorphization, self-reconstruction

Received: March 27, 2024
Revised: June 7, 2024
Published online: June 26, 2024

[1] a) Y. P. Zhu, C. Guo, Y. Zheng, S.-Z. Qiao, *Acc. Chem. Res.* **2017**, *50*, 915; b) B. You, Y. Sun, *Acc. Chem. Res.* **2018**, *51*, 1571.
[2] a) N. C. S. Selvam, L. Du, B. Y. Xia, P. J. Yoo, B. You, *Adv. Funct. Mater.* **2021**, *31*, 2008190; b) C. Wang, Q. Zhang, B. Yan, B. You, J. Zheng, L. Feng, C. Zhang, S. Jiang, W. Chen, S. He, *Nano-Micro Lett.* **2023**, *15*, 52; c) X. Kang, X.-H. Tan, N. Han, J.-F. Hou, C.-M. Yao, Z.-J. Chen, B.-J. Ni, *Tungsten* **2024**, https://doi.org/10.1007/s42864-024-00268-y
[3] a) G. Zhao, K. Rui, S. X. Dou, W. Sun, *Adv. Funct. Mater.* **2018**, *28*, 1803291; b) G. Wang, Z. Chen, W. Wei, B.-J. Ni, *Electron* **2024**, *2*, e54.
[4] P. Saha, S. Amanullah, A. Dey, *Acc. Chem. Res.* **2022**, *55*, 134.
[5] a) X. Zhao, G. Hu, G.-F. Chen, H. Zhang, S. Zhang, H. Wang, *Adv. Mater.* **2021**, *33*, 2007650; b) P. Xiong, J. Tan, H. Lee, N. Ha, S. J. Lee, W. Yang, H. S. Park, *Nano Mater. Sci.* **2022**, https://doi.org/10.1016/j.nanoms.2022.10.001.
[6] V. R. Stamenkovic, D. Strmcnik, P. P. Lopes, N. M. Markovic, *Nat. Mater.* **2017**, *16*, 57.
[7] X. Wang, J.-P. Li, Y. Duan, J. Li, H. Wang, X. Yang, M. Gong, *ChemCatChem* **2022**, *14*, 202101906.
[8] F. W. S. Lucas, R. G. Grim, S. A. Tacey, C. A. Downes, J. Hasse, A. M. Roman, C. A. Farberow, J. A. Schaidle, A. Holewinski, *ACS Energy Lett.* **2021**, *6*, 1205.
[9] a) C. Costentin, M. Robert, J.-M. Savéant, A. Tatin, *Proc. Natl. Acad. Sci. USA* **2015**, *112*, 6882; b) X. Tu, X. Liu, Y. Zhang, J. Zhu, H. Jiang, *Green Carbon* **2024**, https://doi.org/10.1016/j.greenca.2024.03.006.
[10] a) H. Wang, J. Chen, Y. Lin, X. Wang, J. Li, Y. Li, L. Gao, L. Zhang, D. Chao, X. Xiao, J.-M. Lee, *Adv. Mater.* **2021**, *33*, 2008422; b) R.-B. Song, W. Zhu, J. Fu, Y. Chen, L. Liu, J.-R. Zhang, Y. Lin, J.-J. Zhu, *Adv. Mater.* **2020**, *32*, 1903796; c) Z. Chen, G.-F. Han, A. Mahmood, J. Hou, W. Wei, H. Kyong Shon, G. Wang, T. David Waite, J.-B. Baek, B.-J. Ni, *Prog. Mater. Sci.* **2024**, *145*, 101299; d) Z. Chen, T. Ma, W. Wei, W.-Y. Wong, C. Zhao, B.-J. Ni, *Adv. Mater.* **2024**, 2401568.
[11] a) J. Wang, *Curr. Opin. Electrochem.* **2023**, *39*, 101304; b) Y. Li, X. Du, J. Huang, C. Wu, Y. Sun, G. Zou, C. Yang, J. Xiong, *Small* **2019**, *15*, 1901980; c) Z. Wang, Y. Zhou, C. Xia, W. Guo, B. You, B. Y. Xia, *Angew. Chem., Int. Ed.* **2021**, *60*, 19107.
[12] A. Zou, Y. Tang, C. Wu, J. Li, H. Meng, Z. Wang, Y. Ma, H. An, H. Zhong, Q. Zhang, X. Zhang, J. Xue, X. Wang, J. Wu, *ChemSusChem* **2024**, *17*, 202301195.
[13] T. G. Yun, Y. Sim, Y. Lim, D. Kim, J.-S. An, H. Lee, Y. Du, S.-Y. Chung, *Mater. Today* **2022**, *58*, 221.
[14] Z. Chen, N. Han, R. Zheng, Z. Ren, W. Wei, B.-J. Ni, *SusMat* **2023**, *3*, 290.
[15] a) J. Tian, Y. Shen, P. Liu, H. Zhang, B. Xu, Y. Song, J. Liang, J. Guo, *J. Mater. Sci. Technol.* **2022**, *127*, 1; b) Y. Zhou, H. J. Fan, *ACS Mater. Lett.* **2021**, *3*, 136.
[16] B. Jia, B. Zhang, Z. Cai, X. Yang, L. Li, L. Guo, *eScience* **2023**, *3*, 100112.
[17] Y. Song, W. Xie, M. Shao, X. Duan, *Nano Mater. Sci.* **2023**, *5*, 161.

[18] a) X. Han, C. Yu, Y. Niu, Z. Wang, Y. Kang, Y. Ren, H. Wang, H. S. Park, J. Qiu, *Small Methods* **2020**, *4*, 2000546; b) X.-Z. Ren, X.-H. Li, Y.-J. Peng, G.-Z. Wang, J. Yin, X.-C. Zhao, W. Wang, X.-B. Wang, *Rare Met.* **2022**, *41*, 4127.
[19] G. Wan, J. W. Freeland, J. Kloppenburg, G. Petretto, J. N. Nelson, D.-Y. Kuo, C.-J. Sun, J. Wen, J. T. Diulus, G. S. Herman, Y. Dong, R. Kou, J. Sun, S. Chen, K. M. Shen, D. G. Schlom, G.-M. Rignanese, G. Hautier, D. D. Fong, Z. Feng, H. Zhou, J. Suntivich, *Sci. Adv.* *7*, eabc7323.
[20] T. G. Yun, Y. Heo, H. Bin Bae, S.-Y. Chung, *Nat. Commun.* **2021**, *12*, 824.
[21] H. Sun, B. Hu, D. Guan, Z. Hu, L. Fei, M. Li, V. K. Peterson, H.-J. Lin, C.-T. Chen, R. Ran, W. Zhou, Z. Shao, *ChemSusChem* **2020**, *13*, 3045.
[22] D. Guan, C. Shi, H. Xu, Y. Gu, J. Zhong, Y. Sha, Z. Hu, M. Ni, Z. Shao, *J. Energy Chem.* **2023**, *82*, 572.
[23] D. Xiao, X. Bao, D. Dai, Y. Gao, S. Si, Z. Wang, Y. Liu, P. Wang, Z. Zheng, H. Cheng, Y. Dai, B. Huang, *Adv. Mater.* **2023**, *35*, 2304133.
[24] a) S. Chen, L. Ma, Z. Huang, G. Liang, C. Zhi, *Cell Rep. Phys. Sci.* **2022**, *3*, 100729; b) H. Jia, N. Yao, J. Zhu, W. Luo, *Chem. - Eur. J.* **2023**, *29*, 202203073; c) Y. Zeng, M. Zhao, Z. Huang, W. Zhu, J. Zheng, Q. Jiang, Z. Wang, H. Liang, *Adv. Energy Mater.* **2022**, *12*, 2201713.
[25] K. Zhang, R. Zou, *Small* **2021**, *17*, 2100129.
[26] T. Guo, L. Li, Z. Wang, *Adv. Energy Mater.* **2022**, *12*, 2200827.
[27] S. W. Lee, C. Carlton, M. Risch, Y. Surendranath, S. Chen, S. Furutsuki, A. Yamada, D. G. Nocera, Y. Shao-Horn, *J. Am. Chem. Soc.* **2012**, *134*, 16959.
[28] H. Li, Y. Chen, J. Ge, X. Liu, A. C. Fisher, M. P. Sherburne, J. W. Ager, Z. J. Xu, *JACS Au* **2021**, *1*, 2146.
[29] T. Binninger, R. Mohamed, K. Waltar, E. Fabbri, P. Levecque, R. Kötz, T. J. Schmidt, *Sci. Rep.* **2015**, *5*, 12167.
[30] a) S. Samira, J. Hong, J. C. A. Camayang, K. Sun, A. S. Hoffman, S. R. Bare, E. Nikolla, *JACS Au* **2021**, *1*, 2224; b) M. Risch, A. Grimaud, K. J. May, K. A. Stoerzinger, T. J. Chen, A. N. Mansour, Y. Shao-Horn, *J. Phys. Chem. C* **2013**, *117*, 8628.
[31] C. Yang, M. Batuk, Q. Jacquet, G. Rousse, W. Yin, L. Zhang, J. Hadermann, A. M. Abakumov, G. Cibin, A. Chadwick, J.-M. Tarascon, A. Grimaud, *ACS Energy Lett.* **2018**, *3*, 2884.
[32] Y. Duan, J. Y. Lee, S. Xi, Y. Sun, J. Ge, S. J. H. Ong, Y. Chen, S. Dou, F. Meng, C. Diao, A. C. Fisher, X. Wang, G. G. Scherer, A. Grimaud, Z. J. Xu, *Angew. Chem., Int. Ed.* **2021**, *60*, 7418.
[33] Z. Chen, W. Wei, W. Zou, J. Li, R. Zheng, W. Wei, B.-J. Ni, H. Chen, *Green Chem.* **2022**, *24*, 3208.
[34] J. Na, H. Yu, S. Jia, J. Chi, K. Lv, T. Li, Y. Zhao, Y. Zhao, H. Zhang, Z. Shao, *J. Energy Chem.* **2023**, *91*, 370.
[35] a) J.-X. Wu, S.-Z. Hou, X.-D. Zhang, M. Xu, H.-F. Yang, P.-S. Cao, Z.-Y. Gu, *Chem. Sci.* **2019**, *10*, 2199; b) X. Su, Y. Wang, J. Zhou, S. Gu, J. Li, S. Zhang, *J. Am. Chem. Soc.* **2018**, *140*, 11286.
[36] J. Ding, T. Fan, K. Shen, Y. Li, *Appl Catal B* **2021**, *292*, 120174.
[37] W. He, R. Ifraemov, A. Raslin, I. Hod, *Adv. Funct. Mater.* **2018**, *28*, 1707244.
[38] J.-H. Kim, K. Kawashima, B. R. Wygant, O. Mabayoje, Y. Liu, J. H. Wang, C. B. Mullins, *ACS Appl. Energy Mater.* **2018**, *1*, 5145.
[39] C. Walter, P. W. Menezes, S. Orthmann, J. Schuch, P. Connor, B. Kaiser, M. Lerch, M. Driess, *Angew. Chem., Int. Ed.* **2018**, *57*, 698.
[40] X. Zou, Y. Wu, Y. Liu, D. Liu, W. Li, L. Gu, H. Liu, P. Wang, L. Sun, Y. Zhang, *Chem* **2018**, *4*, 1139.
[41] a) S. Jin, *ACS Energy Lett.* **2017**, *2*, 1937; b) M.-L. Guo, Z.-Y. Wu, M.-M. Zhang, Z.-J. Huang, K.-X. Zhang, B.-R. Wang, J.-C. Tu, *Rare Met.* **2023**, *42*, 1847.
[42] L. Yu, Q. Zhu, S. Song, B. McElhenny, D. Wang, C. Wu, Z. Qin, J. Bao, Y. Yu, S. Chen, Z. Ren, *Nat. Commun.* **2019**, *10*, 5106.
[43] S. Ni, H. Qu, Z. Xu, X. Zhu, L. Chen, H. Xing, X. Wu, H. Liu, L. Yang, *ACS Appl. Mater. Interfaces* **2023**, *15*, 36423.
[44] M. Y. Zu, C. Wang, L. Zhang, L. R. Zheng, H. G. Yang, *Mater. Horiz.* **2019**, *6*, 115.
[45] Y. Zhou, B. Chu, Z. Sun, L. Dong, F. Wang, B. Li, M. Fan, Z. Chen, *Appl. Catal. B* **2023**, *323*, 122168.
[46] J. Nie, J. Shi, T. Huang, M.-Y. Xie, Z.-Y. Ouyang, M.-H. Xian, G.-F. Huang, H. Wan, W. Hu, W.-Q. Huang, *Adv. Funct. Mater.* **2024**, 2314172.
[47] T. Hrbek, P. Kúš, T. Košutová, K. Veltruská, T. N. Dinhová, M. Dopita, V. Matolín, I. Matolínová, *Int. J. Hydrogen Energy* **2022**, *47*, 21033.
[48] L. Zhai, C. H. Mak, J. Qian, S. Lin, S. P. Lau, *Electrochim. Acta* **2019**, *305*, 37.
[49] X. Liu, J. Wang, H. Liao, J. Chen, S. Zhang, L. Tan, X. Zheng, D. Chu, P. Tan, J. Pan, *Nano Lett.* **2023**, *23*, 5027.
[50] P. W. Menezes, C. Panda, C. Walter, M. Schwarze, M. Driess, *Adv. Funct. Mater.* **2019**, *29*, 1808632.
[51] S. Zhang, S. Gu, Y. Wang, C. Liang, Y. Yu, L. Han, S. Zheng, N. Zhang, X. Liu, J. Zhou, J. Li, *ACS Catal.* **2019**, *9*, 7389.
[52] G. Zhao, Y. Yao, W. Lu, G. Liu, X. Guo, A. Tricoli, Y. Zhu, *Nano Lett.* **2021**, *21*, 7012.
[53] Z. Xia, C. Ma, Y. Fan, Y. Lu, Y.-C. Huang, Y. Pan, Y. Wu, Q. Luo, Y. He, C.-L. Dong, S. Wang, Y. Zou, *ACS Catal.* **2024**, *14*, 1930.
[54] J. Yu, X. Wu, D. Guan, Z. Hu, S.-C. Weng, H. Sun, Y. Song, R. Ran, W. Zhou, M. Ni, Z. Shao, *Chem. Mater.* **2020**, *32*, 9721.
[55] Y. Chen, H. Li, J. Wang, Y. Du, S. Xi, Y. Sun, M. Sherburne, J. W. Ager, A. C. Fisher, Z. J. Xu, *Nat. Commun.* **2019**, *10*, 572.
[56] N. Ortiz Peña, D. Ihiawakrim, M. Han, B. Lassalle-Kaiser, S. Carenco, C. Sanchez, C. Laberty-Robert, D. Portehault, O. Ersen, *ACS Nano* **2019**, *13*, 11372.
[57] A. Bergmann, E. Martinez-Moreno, D. Teschner, P. Chernev, M. Gliech, J. F. de Araújo, T. Reier, H. Dau, P. Strasser, *Nat. Commun.* **2015**, *6*, 8625.
[58] R. Zhang, N. Dubouis, M. Ben Osman, W. Yin, M. T. Sougrati, D. A. D. Corte, D. Giaume, A. Grimaud, *Angew. Chem., Int. Ed.* **2019**, *58*, 4571.
[59] J. Gao, Y. Liu, B. Liu, K.-W. Huang, *ACS Nano* **2022**, *16*, 17761.
[60] a) X. Liu, J. Meng, K. Ni, R. Guo, F. Xia, J. Xie, X. Li, B. Wen, P. Wu, M. Li, J. Wu, X. Wu, L. Mai, D. Zhao, *Cell Rep Phys Sci* **2020**, *1*, 100241; b) E. S. Davydova, F. D. Speck, M. T. Y. Paul, D. R. Dekel, S. Cherevko, *ACS Catal.* **2019**, *9*, 6837.
[61] a) S. Zhao, Y. Yang, Z. Tang, *Angew. Chem., Int. Ed.* **2022**, *61*, 202110186; b) H.-Q. Zhang, X.-J. Zeng, Q.-Q. Zhang, Z.-L. Zhang, C.-L. Jin, R.-H. Yu, *Tungsten* **2023**, *6*, 585; c) M.-Y. Ma, H.-Z. Yu, L.-M. Deng, L.-Q. Wang, S.-Y. Liu, H. Pan, J.-W. Ren, M. Y. Maximov, F. Hu, S.-J. Peng, *Tungsten* **2023**, *5*, 589.
[62] O. Mabayoje, A. Shoola, B. R. Wygant, C. B. Mullins, *ACS Energy Lett.* **2016**, *1*, 195.
[63] J. Villalobos, D. González-Flores, R. Urcuyo, M. L. Montero, G. Schuck, P. Beyer, M. Risch, *Adv. Energy Mater.* **2021**, *11*, 2101737.
[64] N. Wang, X. Li, M.-K. Hu, W. Wei, S.-H. Zhou, X.-T. Wu, Q.-L. Zhu, *Appl. Catal. B* **2022**, *316*, 121667.
[65] B. Zhang, K. Jiang, H. Wang, S. Hu, *Nano Lett.* **2019**, *19*, 530.
[66] X. Gao, X. Liu, W. Zang, H. Dong, Y. Pang, Z. Kou, P. Wang, Z. Pan, S. Wei, S. Mu, J. Wang, *Nano Energy* **2020**, *78*, 105355.
[67] S. B. Scott, T. V. Hogg, A. T. Landers, T. Maagaard, E. Bertheussen, J. C. Lin, R. C. Davis, J. W. Beeman, D. Higgins, W. S. Drisdell, C. Hahn, A. Mehta, B. Seger, T. F. Jaramillo, I. Chorkendorff, *ACS Energy Lett.* **2019**, *4*, 803.
[68] S. Shen, D. Ma, K. Ouyang, Y. Chen, M. Yang, Y. Wang, S. Sun, H. Mi, L. Sun, C. He, P. Zhang, *Adv. Funct. Mater.* **2023**, *33*, 2304255.
[69] P. W. Menezes, A. Indra, I. Zaharieva, C. Walter, S. Loos, S. Hoffmann, R. Schlögl, H. Dau, M. Driess, *Energy Environ. Sci.* **2019**, *12*, 988.
[70] Q. Fu, L. W. Wong, F. Zheng, X. Zheng, C. S. Tsang, K. H. Lai, W. Shen, T. H. Ly, Q. Deng, J. Zhao, *Nat. Commun.* **2023**, *14*, 6462.

[71] B. Ni, T. He, J.-o. Wang, S. Zhang, C. Ouyang, Y. Long, J. Zhuang, X. Wang, *Chem. Sci.* **2018**, *9*, 2762.
[72] B. Han, A. Grimaud, L. Giordano, W. T. Hong, O. Diaz-Morales, L. Yueh-Lin, J. Hwang, N. Charles, K. A. Stoerzinger, W. Yang, M. T. M. Koper, Y. Shao-Horn, *J. Phys. Chem. C* **2018**, *122*, 8445.
[73] C. W. Song, H. Suh, J. Bak, H. B. Bae, S.-Y. Chung, *Chem* **2019**, *5*, 3243.
[74] K. Fan, H. Zou, Y. Lu, H. Chen, F. Li, J. Liu, L. Sun, L. Tong, M. F. Toney, M. Sui, J. Yu, *ACS Nano* **2018**, *12*, 12369.
[75] Y. Hu, Y. Zheng, J. Jin, Y. Wang, Y. Peng, J. Yin, W. Shen, Y. Hou, L. Zhu, L. An, M. Lu, P. Xi, C.-H. Yan, *Nat. Commun.* **2023**, *14*, 1949.
[76] C. Yue, X. Zhang, J. Yin, H. Zhou, K. Liu, X. Liu, *Appl. Catal. B* **2023**, *339*, 123171.
[77] Z. Chen, R. Zheng, T. Bao, T. Ma, W. Wei, Y. Shen, B.-J. Ni, *Nano-Micro Lett.* **2023**, *15*, 210.
[78] Z. Chen, W. Wei, Y. Shen, B.-J. Ni, *Green Chem.* **2023**, *25*, 5979.
[79] J. Huang, Y. Li, Y. Zhang, G. Rao, C. Wu, Y. Hu, X. Wang, R. Lu, Y. Li, J. Xiong, *Angew. Chem., Int. Ed.* **2019**, *58*, 17458.
[80] T.-G. Vo, G.-S. Tran, C.-L. Chiang, Y.-G. Lin, H.-E. Chang, H.-H. Kuo, C.-Y. Chiang, Y.-J. Hsu, *Adv. Funct. Mater.* **2023**, *33*, 2209386.
[81] P. Xu, Z. Bao, Y. Zhao, L. Zheng, Z. Lv, X. Shi, H.-E. Wang, X. Fang, H. Zheng, *Adv. Energy Mater.* **2024**, *14*, 2303557.
[82] X. Liu, S. Jing, K. Wang, C. Ban, J. Ding, Y. Feng, Y. Duan, J. Ma, D. Yu, X. Han, C. Wang, L. Gan, X. Zhou, *Adv. Funct. Mater.* **2023**, *34*, 2309824.
[83] J. Chen, H. Chen, T. Yu, R. Li, Y. Wang, Z. Shao, S. Song, *Electrochem. Energy Rev.* **2021**, *4*, 566.
[84] H. Chu, R. Li, P. Feng, D. Wang, C. Li, Y. Yu, M. Yang, *ACS Catal.* **2024**, *14*, 1553.
[85] D. González-Flores, I. Sánchez, I. Zaharieva, K. Klingan, J. Heidkamp, P. Chernev, P. W. Menezes, M. Driess, H. Dau, M. L. Montero, *Angew. Chem., Int. Ed.* **2015**, *54*, 2472.
[86] N. J. Firet, T. Burdyny, N. T. Nesbitt, S. Chandrashekar, A. Longo, W. A. Smith, *Catal. Sci. Technol.* **2020**, *10*, 5870.
[87] S. Song, J. Zhou, X. Su, Y. Wang, J. Li, L. Zhang, G. Xiao, C. Guan, R. Liu, S. Chen, H.-J. Lin, S. Zhang, J.-Q. Wang, *Energy Environ. Sci.* **2018**, *11*, 2945.
[88] T. Wu, S. Sun, J. Song, S. Xi, Y. Du, B. Chen, W. A. Sasangka, H. Liao, C. L. Gan, G. G. Scherer, L. Zeng, H. Wang, H. Li, A. Grimaud, Z. J. Xu, *Nat. Catal.* **2019**, *2*, 763.
[89] E. Fabbri, M. Nachtegaal, T. Binninger, X. Cheng, B.-J. Kim, J. Durst, F. Bozza, T. Graule, R. Schäublin, L. Wiles, M. Pertoso, N. Danilovic, K. E. Ayers, T. J. Schmidt, *Nat. Mater.* **2017**, *16*, 925.
[90] T. Liu, D. Liu, F. Qu, D. Wang, L. Zhang, R. Ge, S. Hao, Y. Ma, G. Du, A. M. Asiri, L. Chen, X. Sun, *Adv. Energy Mater.* **2017**, *7*, 1700020.
[91] Z. Gong, R. Liu, H. Gong, G. Ye, J. Liu, J. Dong, J. Liao, M. Yan, J. Liu, K. Huang, L. Xing, J. Liang, Y. He, H. Fei, *ACS Catal.* **2021**, *11*, 12284.
[92] K. Xu, H. Ding, H. Lv, S. Tao, P. Chen, X. Wu, W. Chu, C. Wu, Y. Xie, *ACS Catal.* **2017**, *7*, 310.
[93] C.-L. Ma, Z.-Q. Wang, W. Sun, L.-M. Cao, X.-Q. Gong, J. Yang, *ACS Appl. Mater. Interfaces* **2021**, *13*, 29654.
[94] Q. Zhang, Z. L. Zhe Ru, R. Daiyan, P. Kumar, J. Pan, X. Lu, R. Amal, *ACS Appl. Mater. Interfaces* **2021**, *13*, 53798.
[95] a) Z. Gong, J. Liu, M. Yan, H. Gong, G. Ye, H. Fei, *ACS Nano* **2023**, *17*, 18372; b) Z. Chen, N. Han, W. Wei, D. Chu, B.-J. Ni, *EcoEnergy* **2024**, *2*, 114.
[96] a) A. Sivanantham, P. Ganesan, A. Vinu, S. Shanmugam, *ACS Catal.* **2020**, *10*, 463; b) S. Anantharaj, S. Noda, *Int. J. Hydrogen Energy* **2020**, *45*, 15763.
[97] Z. Chen, R. Zheng, S. Li, R. Wang, W. Wei, W. Wei, B.-J. Ni, H. Chen, *Chem. Eng. J.* **2022**, *431*, 134304.
[98] J.-G. Wang, W. Hua, M. Li, H. Liu, M. Shao, B. Wei, *ACS Appl. Mater. Interfaces* **2018**, *10*, 41237.
[99] W. Zou, C. Sun, K. Zhao, J. Li, X. Pan, D. Ye, Y. Xie, W. Xu, H. Zhao, L. Zhang, J. Zhang, *Electrochim. Acta* **2020**, *345*, 136114.
[100] M. Miao, R. Hou, R. Qi, Y. Yan, L. Q. Gong, K. Qi, H. Liu, B. Y. Xia, *J. Mater. Chem. A* **2019**, *7*, 18925.
[101] a) H. Chen, X. Zou, *Inorg. Chem. Front.* **2020**, *7*, 2248; b) Z. Chen, W. Wei, B.-J. Ni, *Curr. Opin. Electrochem.* **2022**, *31*, 100888.
[102] S. Niu, W.-J. Jiang, Z. Wei, T. Tang, J. Ma, J.-S. Hu, L.-J. Wan, *J. Am. Chem. Soc.* **2019**, *141*, 7005.
[103] Z. Chen, R. Zheng, W. Zou, W. Wei, J. Li, W. Wei, B.-J. Ni, H. Chen, *Appl Catal B* **2021**, *298*, 120583.
[104] J. Li, H. Chen, Y. Liu, R. Gao, X. Zou, *J. Mater. Chem. A* **2019**, *7*, 5288.
[105] H. Xu, K. Li, N. Liu, W. Xia, W. Liu, D. Cao, L. Zhang, D. Cheng, *Catal. Sci. Technol.* **2023**, *13*, 6780.
[106] W. Chen, H. Wang, Y. Li, Y. Liu, J. Sun, S. Lee, J.-S. Lee, Y. Cui, *ACS Cent. Sci.* **2015**, *1*, 244.
[107] Y. Y. Sun, X. Y. Zhang, J. Tang, X. Li, H. Q. Fu, H. G. Xu, F. Mao, P. Liu, H. G. Yang, *Small* **2023**, *19*, 2207965.
[108] C.-X. Zhao, J.-N. Liu, C. Wang, J. Wang, L. Song, B.-Q. Li, Q. Zhang, *Energy Environ. Sci.* **2022**, *15*, 3257.
[109] H. Lei, L. Ma, Q. Wan, S. Tan, B. Yang, Z. Wang, W. Mai, H. J. Fan, *Adv. Energy Mater.* **2022**, *12*, 2202522.
[110] W. Zong, D. Rao, H. Guo, Y. Ouyang, Y.-E. Miao, W. Wang, J. Wang, F. Lai, T. Liu, *Nanoscale* **2020**, *12*, 10977.
[111] C. Zhong, Z. Han, T. Wang, Q. Wang, Z. Shen, Q. Zhou, J. Wang, S. Zhang, X. Jin, S. Li, P. Wang, D. Gao, Y. Zhou, H. Zhang, *J. Mater. Chem. A* **2020**, *8*, 10831.
[112] Q. Xu, H. Jiang, X. Duan, Z. Jiang, Y. Hu, S. W. Boettcher, W. Zhang, S. Guo, C. Li, *Nano Lett.* **2021**, *21*, 492.
[113] a) T. Wang, Y. Wang, Y. Zhao, Y. Bu, *Energy Fuels* **2024**, *38*, 671; b) W. Shen, J. Jin, Y. Hu, Y. Hou, J. Yin, Z. Ma, Y.-Q. Zhao, P. Xi, *Chin. J. Catal.* **2022**, *43*, 1485.
[114] J. N. Hausmann, S. Mebs, K. Laun, I. Zebger, H. Dau, P. W. Menezes, M. Driess, *Energy Environ. Sci.* **2020**, *13*, 3607.
[115] W. Chen, Y. Liu, Y. Li, J. Sun, Y. Qiu, C. Liu, G. Zhou, Y. Cui, *Nano Lett.* **2016**, *16*, 7588.
[116] a) H. Liao, G. Ni, P. Tan, Y. Liu, K. Chen, G. Wang, M. Liu, J. Pan, *Appl. Catal. B* **2022**, *317*, 121713; b) Y. Wu, M. Song, Y.-C. Huang, C.-L. Dong, Y. Li, Y. Lu, B. Zhou, D. Wang, J. Jia, S. Wang, Y. Wang, *J Energy Chem* **2022**, *74*, 140.
[117] J. Wang, S.-J. Kim, J. Liu, Y. Gao, S. Choi, J. Han, H. Shin, S. Jo, J. Kim, F. Ciucci, H. Kim, Q. Li, W. Yang, X. Long, S. Yang, S.-P. Cho, K. H. Chae, M. G. Kim, H. Kim, J. Lim, *Nat. Catal.* **2021**, *4*, 212.
[118] J. Liu, W. Qiao, Z. Zhu, J. Hu, X. Xu, *Small* **2022**, *18*, 2202434.
[119] M. Liu, W. Cui, Z. Sun, C. Zhang, C. He, B. Zou, P. Geng, Z. Zhao, *Electrochim. Acta* **2024**, *477*, 143713.
[120] F. Luo, X. Shu, X. Jiang, Y. Liu, J. Zhang, S. Chen, *J. Power Sources* **2022**, *551*, 232181.
[121] X. Sun, Y. Liu, Y. Wang, F. Liu, S. Zhang, Y. Li, Y. Xue, C. Tang, J. Zhang, *Appl. Surf. Sci.* **2024**, *642*, 158620.
[122] Y. Duan, S. Sun, Y. Sun, S. Xi, X. Chi, Q. Zhang, X. Ren, J. Wang, S. J. H. Ong, Y. Du, L. Gu, A. Grimaud, Z. J. Xu, *Adv. Mater.* **2019**, *31*, 1807898.
[123] T.-H. Shen, L. Spillane, J. Vavra, T. H. M. Pham, J. Peng, Y. Shao-Horn, V. Tileli, *J. Am. Chem. Soc.* **2020**, *142*, 15876.
[124] Y. Zhu, H. A. Tahini, Z. Hu, Z.-G. Chen, W. Zhou, A. C. Komarek, Q. Lin, H.-J. Lin, C.-T. Chen, Y. Zhong, M. T. Fernández-Díaz, S. C. Smith, H. Wang, M. Liu, Z. Shao, *Adv. Mater.* **2020**, *32*, 1905025.
[125] P. W. Menezes, A. Indra, C. Das, C. Walter, C. Göbel, V. Gutkin, D. Schmeißer, M. Driess, *ACS Catal.* **2017**, *7*, 103.
[126] A. Saad, Y. Gao, A. Ramiere, T. Chu, G. Yasin, Y. Wu, S. Ibraheem, M. Wang, H. Guo, P. Tsiakaras, X. Cai, *Small* **2022**, *18*, 2201067.
[127] B. Kirubasankar, Y. S. Won, S. H. Choi, J. W. Kim, L. A. Adofo, S. M. Kim, K. K. Kim, *Chem. Commun.* **2023**, *59*, 9247.

[128] W. Peng, J. Li, K. Shen, L. Zheng, H. Tang, Y. Gong, J. Zhou, N. Chen, S. Zhao, M. Chen, F. Gao, H. Gou, *J. Mater. Chem. A* **2020**, *8*, 23580.
[129] A. Grimaud, C. E. Carlton, M. Risch, W. T. Hong, K. J. May, Y. Shao-Horn, *J. Phys. Chem. C* **2013**, *117*, 25926.
[130] D. Li, W. Wan, Z. Wang, H. Wu, S. Wu, T. Jiang, G. Cai, C. Jiang, F. Ren, *Adv. Energy Mater.* **2022**, *12*, 2201913.
[131] N. Zhang, Y. Hu, L. An, Q. Li, J. Yin, J. Li, R. Yang, M. Lu, S. Zhang, P. Xi, C.-H. Yan, *Angew. Chem., Int. Ed.* **2022**, *61*, 202207217.
[132] D. Yang, Z. Su, Y. Chen, K. Srinivas, X. Zhang, W. Zhang, H. Lin, *Chem. Eng. J.* **2022**, *430*, 133046.
[133] T. Zhao, X. Shen, Y. Wang, R. K. Hocking, Y. Li, C. Rong, K. Dastafkan, Z. Su, C. Zhao, *Adv. Funct. Mater.* **2021**, *31*, 2100614.
[134] K. Fan, H. Zou, Y. Ding, N. V. R. A. Dharanipragada, L. Fan, A. K. Inge, L. Duan, B. Zhang, L. Sun, *Small* **2022**, *18*, 2107249.
[135] G. Zhang, J. Zeng, J. Yin, C. Zuo, P. Wen, H. Chen, Y. Qiu, *Appl Catal B* **2021**, *286*, 119902.
[136] P. W. Menezes, A. Indra, A. Bergmann, P. Chernev, C. Walter, H. Dau, P. Strasser, M. Driess, *J. Mater. Chem. A* **2016**, *4*, 10014.
[137] a) S. Hou, W. Li, S. Watzele, R. M. Kluge, S. Xue, S. Yin, X. Jiang, M. Döblinger, A. Welle, B. Garlyyev, M. Koch, P. Müller-Buschbaum, C. Wöll, A. S. Bandarenka, R. A. Fischer, *Adv. Mater.* **2021**, *33*, 2103218; b) W. Fang, R. Lu, F.-M. Li, D. Wu, K. Yue, C. He, Y. Mao, W. Guo, B. You, F. Song, T. Yao, Z. Wang, B. Y. Xia, *Angew. Chem., Int. Ed.* **2024**, *63*, 202319936; c) W. Wu, X. Ma, Y. Zhu, F. Hu, G. Huang, N. Wang, S. Ning, Y. Zhu, P. K. Shen, J. Zhu, *Chem. Eng. J.* **2023**, *478*, 147425.
[138] H. Man, J. Feng, S. Wang, S. Li, P. Li, H. He, W. Raróg-Pilecka, J. Zhao, J. Zhang, F. Fang, D. Sun, Y. Li, Y. Song, *Cell Rep Phys Sci* **2022**, *3*, 101059.
[139] J. Choi, D. Kim, W. Zheng, B. Yan, Y. Li, L. Y. S. Lee, Y. Piao, *Appl Catal B* **2021**, *286*, 119857.
[140] T. Kang, K. Kim, M. Kim, J. Kim, *J. Catal.* **2021**, *404*, 80.
[141] Y. Yi, Q. Wu, J. Li, W. Yao, C. Cui, *ACS Appl. Mater. Interfaces* **2021**, *13*, 17439.
[142] N. Li, L. Cai, C. Wang, Y. Lin, J. Huang, H. Sheng, H. Pan, W. Zhang, Q. Ji, H. Duan, W. Hu, W. Zhang, F. Hu, H. Tan, Z. Sun, B. Song, S. Jin, W. Yan, *J. Am. Chem. Soc.* **2021**, *143*, 18001.
[143] Z. Xie, K. Wang, Y. Zou, G. Ying, J. Jiang, *Sci. Adv.* **2023**, *2*, 161.
[144] X. Xu, H. Liao, L. Huang, S. Chen, R. Wang, S. Wu, Y. Wu, Z. Sun, H. Huang, *Appl Catal B* **2024**, *341*, 123312.
[145] T. Dai, X. Zhang, M. Sun, B. Huang, N. Zhang, P. Da, R. Yang, Z. He, W. Wang, P. Xi, C.-H. Yan, *Adv. Mater.* **2021**, *33*, 2102593.
[146] X. Cao, T. Wang, H. Qin, G. Lin, L. Zhao, L. Jiao, *Nano Res.* **2023**, *16*, 3665.
[147] Y. Duan, Z.-Y. Yu, S.-J. Hu, X.-S. Zheng, C.-T. Zhang, H.-H. Ding, B.-C. Hu, Q.-Q. Fu, Z.-L. Yu, X. Zheng, J.-F. Zhu, M.-R. Gao, S.-H. Yu, *Angew. Chem., Int. Ed.* **2019**, *58*, 15772.
[148] Z. Chen, R. Zheng, W. Wei, W. Wei, B.-J. Ni, H. Chen, *J. Energy Chem.* **2022**, *68*, 275.
[149] L. Zhang, R. Zhang, R. Ge, X. Ren, S. Hao, F. Xie, F. Qu, Z. Liu, G. Du, A. M. Asiri, B. Zheng, X. Sun, *Chem. - Eur. J.* **2017**, *23*, 11499.
[150] R. Zhang, Z. Wang, S. Hao, R. Ge, X. Ren, F. Qu, G. Du, A. M. Asiri, B. Zheng, X. Sun, *ACS Sustain. Chem. Eng.* **2017**, *5*, 8518.
[151] D. Zhou, L. He, R. Zhang, S. Hao, X. Hou, Z. Liu, G. Du, A. M. Asiri, C. Zheng, X. Sun, *Chem. - Eur. J.* **2017**, *23*, 15601.
[152] Y. Tong, J. Wu, P. Chen, H. Liu, W. Chu, C. Wu, Y. Xie, *J. Am. Chem. Soc.* **2018**, *140*, 11165.
[153] H. Liu, R. Xie, Q. Wang, J. Han, Y. Han, J. Wang, H. Fang, J. Qi, M. Ding, W. Ji, B. He, W. Lü, *Adv. Sci.* **2023**, *10*, 2207128.
[154] C. Karakaya, N. Solati, U. Savacı, E. Keleş, S. Turan, S. Çelebi, S. Kaya, *ACS Catal.* **2020**, *10*, 15114.
[155] a) Z. Wang, X. Guo, J. Montoya, J. K. Nørskov, *NPJ Comput Mater* **2020**, *6*, 160; b) S. Anantharaj, S. Noda, *Nano Energy* **2023**, *114*, 108624.
[156] X. Liu, R. Guo, K. Ni, F. Xia, C. Niu, B. Wen, J. Meng, P. Wu, J. Wu, X. Wu, L. Mai, *Adv. Mater.* **2020**, *32*, 2001136.
[157] K. J. May, C. E. Carlton, K. A. Stoerzinger, M. Risch, J. Suntivich, Y.-L. Lee, A. Grimaud, Y. Shao-Horn, *J. Phys. Chem. Lett.* **2012**, *3*, 3264.
[158] Y. J. Son, S. Kim, V. Leung, K. Kawashima, J. Noh, K. Kim, R. A. Marquez, O. A. Carrasco-Jaim, L. A. Smith, H. Celio, D. J. Milliron, B. A. Korgel, C. B. Mullins, *ACS Catal.* **2022**, *12*, 10384.
[159] M. B. Stevens, M. E. Kreider, A. M. Patel, Z. Wang, Y. Liu, B. M. Gibbons, M. J. Statt, A. V. Ievlev, R. Sinclair, A. Mehta, R. C. Davis, J. K. Nørskov, A. Gallo, L. A. King, T. F. Jaramillo, *ACS Appl. Energy Mater.* **2020**, *3*, 12433.
[160] B.-J. Kim, E. Fabbri, M. Borlaf, D. F. Abbott, I. E. Castelli, M. Nachtegaal, T. Graule, T. J. Schmidt, *Mater. Adv.* **2021**, *2*, 345.
[161] Y. Zhang, L. Gao, E. J. M. Hensen, J. P. Hofmann, *ACS Energy Lett.* **2018**, *3*, 1360.
[162] K. Xu, H. Cheng, L. Liu, H. Lv, X. Wu, C. Wu, Y. Xie, *Nano Lett.* **2017**, *17*, 578.
[163] D. Cao, D. Liu, S. Chen, O. A. Moses, X. Chen, W. Xu, C. Wu, L. Zheng, S. Chu, H. Jiang, C. Wang, B. Ge, X. Wu, J. Zhang, L. Song, *Energy Environ. Sci.* **2021**, *14*, 906.
[164] P. Liu, H. Liu, S. Zhang, J. Wang, C. Wang, *Electrochim. Acta* **2020**, *354*, 136753.
[165] X. Ji, S. Hao, F. Qu, J. Liu, G. Du, A. M. Asiri, L. Chen, X. Sun, *Nanoscale* **2017**, *9*, 7714.
[166] N. N. Rao, C. Alex, M. Mukherjee, S. Roy, A. Tayal, A. Datta, N. S. John, *ACS Catal.* **2024**, *14*, 981.
[167] X. Li, C. Wang, S. Zheng, H. Xue, Q. Xu, P. Braunstein, H. Pang, *J. Colloid Interface Sci.* **2022**, *624*, 443.
[168] F. Song, X. Hu, *J. Am. Chem. Soc.* **2014**, *136*, 16481.
[169] S. Li, R. Ma, J. Hu, Z. Li, L. Liu, X. Wang, Y. Lu, G. E. Sterbinsky, S. Liu, L. Zheng, J. Liu, D. Liu, J. Wang, *Nat. Commun.* **2022**, *13*, 2916.
[170] F. Guo, Y. Wu, H. Chen, Y. Liu, L. Yang, X. Ai, X. Zou, *Energy Environ. Sci.* **2019**, *12*, 684.
[171] H. Liao, X. Zhang, S. Niu, P. Tan, K. Chen, Y. Liu, G. Wang, M. Liu, J. Pan, *Appl Catal B* **2022**, *307*, 121150.
[172] Z. Xu, W. Zuo, Y. Yu, J. Liu, G. Cheng, P. Zhao, *Adv. Sci.* **2024**, *11*, 2306758.
[173] L. Ma, H. Zhou, M. Xu, P. Hao, X. Kong, H. Duan, *Chem. Sci.* **2021**, *12*, 938.
[174] X. Gao, X. Bai, P. Wang, Y. Jiao, K. Davey, Y. Zheng, S.-Z. Qiao, *Nat. Commun.* **2023**, *14*, 5842.
[175] Y. Fang, Y. Fang, R. Zong, Z. Yu, Y. Tao, J. Shao, *J. Mater. Chem. A* **2022**, *10*, 1369.
[176] Y. Kang, S. Wang, K. S. Hui, S. Wu, D. A. Dinh, X. Fan, F. Bin, F. Chen, J. Geng, W.-C. M. Cheong, K. N. Hui, *Nano Res.* **2022**, *15*, 2952.
[177] H. Cao, P. Qiao, Q. Zhong, R. Qi, Y. Dang, L. Wang, Z. Xu, W. Zhang, *Small* **2023**, *19*, 2204864.
[178] J. Zhao, F. Wang, X. Lu, T. Lv, Y. Li, Q. Hao, L. Liang, H. Liu, *J. Colloid Interface Sci.* **2023**, *642*, 532.
[179] X. Gao, X. Li, Y. Yu, Z. Kou, P. Wang, X. Liu, J. Zhang, J. He, S. Mu, J. Wang, *Nano Energy* **2021**, *85*, 105961.
[180] H. Zhang, D. Guan, Z. Hu, Y.-C. Huang, X. Wu, J. Dai, C.-L. Dong, X. Xu, H.-J. Lin, C.-T. Chen, W. Zhou, Z. Shao, *Appl Catal B* **2021**, *297*, 120484.
[181] Y. Deng, W. Lai, L. Ge, H. Yang, J. Bao, B. Ouyang, H. Li, *Inorg. Chem.* **2023**, *62*, 3976.
[182] J.-T. Ren, Y.-S. Wang, Y.-J. Song, L. Chen, Z.-Y. Yuan, *Appl Catal B* **2022**, *309*, 121279.
[183] Y. Chen, J. Xu, M. Jiang, L. Wang, R. Ma, Y. Chen, Z.-H. Xie, P. Munroe, F. Hu, L. Li, S. Peng, *Adv. Energy Mater.* **2023**, *14*, 2303450.
[184] M. Chen, S. Lu, X.-Z. Fu, J.-L. Luo, *Adv. Sci.* **2020**, *7*, 1903777.
[185] L. An, F. Yang, C. Fu, X. Cai, S. Shen, G. Xia, J. Li, Y. Du, L. Luo, J. Zhang, *Adv. Funct. Mater.* **2022**, *32*, 2200131.

[186] X. Xu, T. Wang, L. Su, Y. Zhang, L. Dong, X. Miao, *ACS Sustainable Chem. Eng.* **2021**, *9*, 5693.
[187] M. Lu, S. Kong, S. Yan, P. Zhou, T. Yu, Z. Zou, *J. Mater. Chem. A* **2022**, *10*, 12391.
[188] M. Fang, D. Han, W.-B. Xu, Y. Shen, Y. Lu, P. Cao, S. Han, W. Xu, D. Zhu, W. Liu, J. C. Ho, *Adv. Energy Mater.* **2020**, *10*, 2001059.
[189] a) C.-L. Ma, X.-R. Yang, Z.-Q. Wang, W. Sun, L. Zhu, L.-M. Cao, X.-Q. Gong, J. Yang, *ACS Appl. Mater. Interfaces* **2022**, *14*, 28706; b) H. Qin, Y. Ye, J. Li, W. Jia, S. Zheng, X. Cao, G. Lin, L. Jiao, *Adv. Funct. Mater.* **2023**, *33*, 2209698; c) X.-X. Li, X.-C. Liu, C. Liu, J.-M. Zeng, X.-P. Qi, *Tungsten* **2023**, *5*, 100.
[190] G. Wang, C. Jin, G. Zhang, L. Qian, X. Chen, J. Tan, W. Wang, J. Yin, X. Liu, H. Zhou, *Dalton Trans.* **2021**, *50*, 6333.
[191] a) X. Wang, W. Li, D. Xiong, D. Y. Petrovykh, L. Liu, *Adv. Funct. Mater.* **2016**, *26*, 4067; b) X. Li, G.-Q. Han, Y.-R. Liu, B. Dong, W.-H. Hu, X. Shang, Y.-M. Chai, C.-G. Liu, *ACS Appl. Mater. Interfaces* **2016**, *8*, 20057; c) Z. Chen, W. Zou, R. Zheng, W. Wei, W. Wei, B.-J. Ni, H. Chen, *Green Chem.* **2021**, *23*, 6538.
[192] Y. Jin, M. Zhang, L. Song, M. Zhang, *Small* **2023**, *19*, 2206081.
[193] D. Li, Y. Qin, J. Liu, H. Zhao, Z. Sun, G. Chen, D.-Y. Wu, Y. Su, S. Ding, C. Xiao, *Adv. Funct. Mater.* **2022**, *32*, 2107056.
[194] C. Guo, Y. Shi, S. Lu, Y. Yu, B. Zhang, *Chin. J. Catal.* **2021**, *42*, 1287.
[195] R. Lin, L. Kang, T. Zhao, J. Feng, V. Celorrio, G. Zhang, G. Cibin, A. Kucernak, D. J. L. Brett, F. Corà, I. P. Parkin, G. He, *Energy Environ. Sci.* **2022**, *15*, 2386.
[196] a) B. Yan, D. Krishnamurthy, C. H. Hendon, S. Deshpande, Y. Surendranath, V. Viswanathan, *Joule* **2017**, *1*, 600; b) S. Hu, J. Wang, J. Zhang, J. Lim, Y. Gao, S. Zhang, *Appl Catal B* **2021**, *282*, 119593.
[197] X. Li, J. Wang, X. Lv, Y. Yang, Y. Xu, Q. Liu, H. B. Wu, *Nano-Micro Lett.* **2022**, *14*, 134.
[198] a) S. Liu, M. Wang, T. Qian, H. Ji, J. Liu, C. Yan, *Nat. Commun.* **2019**, *10*, 3898; b) P. Li, W. Fu, P. Zhuang, Y. Cao, C. Tang, A. B. Watson, P. Dong, J. Shen, M. Ye, *Small* **2019**, *15*, 1902535.
[199] X. Zhou, Y. Liu, L. Liu, Y. Yu, J. Xu, M. Ruan, S. Li, L. Qian, *Appl Catal B* **2024**, *343*, 123552.
[200] F. H. Saadi, A. I. Carim, W. S. Drisdell, S. Gul, J. H. Baricuatro, J. Yano, M. P. Soriaga, N. S. Lewis, *J. Am. Chem. Soc.* **2017**, *139*, 12927.
[201] J. Sun, G. Ren, S. Qin, Z. Zhao, Z. Li, Z. Zhang, C. Li, X. Meng, *Nano Energy* **2024**, *121*, 109246.
[202] G. Hai, J. Huang, L. Cao, K. Kajiyoshi, L. Wang, L. Feng, *Appl. Surf. Sci.* **2021**, *562*, 150145.
[203] Y. Liang, W. Zhou, Y. Shi, C. Liu, B. Zhang, *Sci. Bull.* **2020**, *65*, 1547.
[204] T. Kou, S. Wang, S. Yang, Q. Ren, R. Ball, D. Rao, S. Chiovoloni, J. Q. Lu, Z. Zhang, E. B. Duoss, Y. Li, *ACS Mater. Lett.* **2022**, *4*, 1999.
[205] X. Zhou, X. Lu, T. Yu, H. Wang, L. Qian, P. Lei, Y. Yu, L. Liu, S. Xia, J. Fang, *ACS Appl. Mater. Interfaces* **2020**, *12*, 31319.
[206] H. Cheng, S. Jia, J. Jiao, X. Chen, T. Deng, C. Xue, M. Dong, J. Zeng, C. Chen, H. Wu, M. He, B. Han, *Green Chem.* **2024**, *26*, 2599.
[207] Q. Li, Z. Xing, D. Wang, X. Sun, X. Yang, *ACS Catal.* **2016**, *6*, 2797.
[208] J. Wang, D. Wu, M. Li, X. Wei, X. Yang, M. Shao, M. Gu, *Nano Lett.* **2022**, *22*, 5600.
[209] X. Shang, K.-L. Yan, Y. Rao, B. Dong, J.-Q. Chi, Y.-R. Liu, X. Li, Y.-M. Chai, C.-G. Liu, *Nanoscale* **2017**, *9*, 12353.
[210] A. W. H. Whittingham, R. D. L. Smith, *ChemElectroChem* **2019**, *6*, 5116.

Huishan Meng received her master degree in the School of Ecological and Environmental Sciences from East China Normal University in 2020. Currently, she is pursuing her Ph.D. degree at the same university and a visiting scholar at the University of Technology Sydney. Her research interest lies in developing novel electrocatalytic systems for the recovery of resources and the conversion of energy from organic contaminants.

Zhijie Chen received his Ph.D. degree in Environmental Engineering from the University of Technology Sydney (Australia) in 2022. He now works as a Postdoc researcher at the University of New South Wales, Sydney. His research mainly work focuses on developing green techniques and cost-effective functional materials for sustainable energy and environmental applications, such as resourse recovery, (waste)water electrolysis, plastic waste upcycling, and wastewater remediation.

Jinliang Zhu is an associate professor at the School of Resources, Environment and Materials at Guangxi University. He received his Ph.D. degree from Sun Yat-sen University in 2014. Currently, his research areas encompass lithium $^{-1}$sodium-ion batteries, water electrolysis, and the development of graphene materials.

Bo You received his Ph.D. degree in 2014 under the supervision of Prof. Zhaoxiang Deng at the University of Science and Technology of China (USTC). He then joined Prof. Yujie Sun's group at Utah State University from 2014 to 2016, Prof. Hong Li's group at Nanyang Technological University from 2016 to 2017, and Prof. Shi Zhang Qiao's group at The University of Adelaide from 2017 to 2019 as a postdoctoral researcher. Currently, he is a professor at Huazhong University of Science and Technology (HUST). His research focuses on integration-designed electro-activation (IDEA) for advanced renewable energy.

Tianyi Ma received his Ph.D. in physical chemistry in 2013 from Nankai University, China. He is a Fellow of the Royal Society of Chemistry and Clarivate's Global Highly Cited Researcher. He was awarded an Australian Research Council Discovery Early Career Researcher Award (2014) and Future Fellowship (2021). He is currently a full professor at RMIT University, focusing on functional photocatalytic, electrocatalytic, thermocatalytic, and piezocatalytic materials for renewable solar, mechanical, and thermal energy harvesting and utilization, as well as carbon capture, utilization, and storage; these processes are further incorporated into his developed next-generation high-performance battery and supercapacitor-based energy storage devices.

Wei Wei obtained her PhD degree in Environmental Science and Engineering from Harbin Institute of Technology (China) in 2018 and awarded an Outstanding PhD Award from Chinese Education Department. She joined University of Technology Sydney in 2019, and currently is an Australian Research Council (ARC) DECRA Fellow and Lecturer at School of Civil and Environmental Engineering of UTS. Her research focuses on the development and application of innovative and sustainable techniques to achieve sustainable energy recovery from waste.

Sergio Vernuccio received his Ph.D. in Process Engineering from ETH Zurich, Switzerland in 2017. From 2017 and 2019 he worked as a postdoctoral researcher in the group of Prof. Linda J. Broadbelt at Northwestern University, USA where he studied mechanisms of acid-based oligomerization of olefins on zeolites for the upgrading of shale gas resources. His research activity spans from catalysis to reaction engineering and aims to understand the link between macroscopic observation and fundamental phenomena in complex reaction systems.

Juan Xu received her Ph.D. degree from the University of Science and Technology of China. She then completed postdoctoral research at the University of Hong Kong. She is currently a professor in the School of Ecological and Environmental Sciences at East China Normal University. Her research focuses on discovering novel technologies and methods for water pollution control and resource recovery from organic waste.

Bing-Jie Ni received his Ph.D. degree in environmental engineering in June 2009. He currently is a full professor at the University of New South Wales, Sydney. He is a Fellow of the Royal Society of Chemistry and Clarivate Global Highly Cited Researcher. His work focuses on the integration of different disciplines to develop innovative and sustainable technological solutions to achieve environmental and energy sustainability.